

Josephson Tunneling at the Atomic Scale: The Josephson Effect as a Local Probe

THIS IS A TEMPORARY TITLE PAGE
It will be replaced for the final print by a version
provided by the service academique.

Thèse n. 6750 2015
présentée le 22 juillet 2015
à la Faculté des Sciences des Bases
Laboratoire à l'Echelle Nanométrique
Programme Doctoral en Physique
École Polytechnique Fédérale de Lausanne

pour l'obtention du grade de Docteur des Sciences
par

Berthold Jäck

acceptée sur proposition du jury:

Prof. Andreas Pautz, président du jury
Prof. Klaus Kern, directeur de thèse
Prof. Davor Pavuna, rapporteur
Prof. Hermann Suderow, rapporteur
Dr. Fabien Portier, rapporteur

Lausanne, EPFL, 2015



Non est ad astra mollis e terris via
— Lucius Annaeus Seneca

Acknowledgements

It took me about three and a half years, with many ups and downs, to complete this thesis. At this point, I want to say *thank you* to all the people that supported me on my way by any means.

First of all, I am grateful to *Prof. Klaus Kern* for giving me the opportunity to perform my doctoral studies under his supervision at the Max-Planck-Institute for Solid State Research in Stuttgart, Germany. For the entire time of my studies, I enjoyed a significant scientific freedom, such that I had the great possibility to pursue and realize my own ideas. In particular, I want to acknowledge his personal support, which allowed me to attend conferences, workshops and schools, have interesting scientific discussions as well as a wonderful time in the whole of Europe and across the USA. I highly appreciate his support and the trust he put in me.

I am very grateful to *Dr. Christian Ast* and *Dr. Markus Etzkorn* for supervising my studies, their continuous support and many fruitful discussions about physics. I highly benefited and learned from their exceptional experimental, theoretical and computational knowledge as well as experience.

I am thankful to *Prof. Andreas Pautz*, *Prof. Davor Pavuna*, *Prof. Hermann Suderow* and *Dr. Fabien Portier* for being part of my thesis committee.

Special thanks go to my fellow PhD colleague *Matthias Eltschka*. We really worked hard to tame the beast, a.k.a. the milli-Kelvin STM, and spent many day and night shifts together in the MPI. Our shared working ethics certainly helped to accomplish this thesis.

All the results that I presented in this thesis would not exist without the permanent help and support from many people at the MPI. In particular, I am grateful to our technicians *Wolfgang Stiepany*, *Peter Andler* and *Marco Memmler* for their permanent support on taming the beast and their immediate help on repairing parts that I had damaged. Moreover, they were also great football team mates in *Kernspaltung*. I am also very thankful to *Sabine Birtel* who always had a helping hand for me. At this point, I also want to express my thanks to the low temperature service group, the IT service group, the crystal growth service group and the technology service group of our institute.

I am very thankful to *Dr. Christian Urbina* and *Dr. Fabien Portier* from CEA Saclay. I benefited a lot from their comprehensive knowledge on Josephson physics and I highly appreciated

Acknowledgements

the opportunity to visit the Quantronics group at the CEA Saclay. I also want to express my gratitude to *Prof. Joachim Ankerhold*, *Prof. Alex Balatsky*, *Prof. Gerd-Ludwig Ingold*, *Prof. Dimitri Roditchev* and *Prof. Alexey Ustinov* for fruitful discussions about Josephson physics.

I am very grateful to *Dr. Thomas White* for thoroughly proofreading my thesis within the shortest possible time.

Working on a PhD thesis in experimental physics focuses on lab work, data analysis and scientific discussion. However, this job certainly runs better if you are in good company, which I certainly was. I'm grateful to have met *Dr. Laura Rizzi* and *Daniel Weber* in the guesthouse on my first day here in Stuttgart. Their company gave me an easy start and I'm very happy to be still in friendly contact with Dan. Special thanks go to my ol' 6B10 office crew, *Alexander 'Ali' Kölker* and *Jon 'Nathan' Parnell*, for fun times, good music and serious target shooting competitions. I also highly enjoyed my "scientific" roadtrips through Europe and the United States together with *Daniel Rosenblatt* and *Christoph Grosse*. I am glad that I met *Sebastian Koslowski* and that we share more than only our passion for running. Moreover, I want to thank *Carola Straßer*, *Verena Schendel*, *Lukas Schlipf*, *Claudius Morchutt*, *Christian Dette*, *Ivan Pentegov*, *Matthias Muenks*, *Jacob Senkpiel*, *Dr. Tobias Herden*, *Benjamin Wurster*, and *Diana Hoetger* for fun times at the MPI, on the Cannstatter Wasen and anywhere else.

I want to express my deepest thankfulness to my parents, *Dr. Herbert Jäck* and *Dorothea Jäck* who, always and literally, unconditionally supported my path of life. My highest gratitude goes to my partner *Silvia* who cheered me up in hard times and enjoyed the happy times with me. Her permanent support was outstanding, such that it is not wrong to say: She did half of all the work!

Stuttgart, 21st of May, 2015

B. J.

Abstract

The aim of this thesis is to characterize the properties of a Josephson junction in a Scanning Tunneling Microscope (STM) at millikelvin temperatures and to implement Josephson STM (JSTM) as a versatile probe at the atomic scale. To this end we investigate the $I(V_J)$ tunneling characteristics of the Josephson junction in our STM at a base temperature of 15 mK by means of current-biased and voltage-biased experiments. We find that in the tunneling regime, $G_N \ll G_0$, the Josephson junction is operated in the dynamical Coulomb blockade (DCB) regime in which the sequential tunneling of Cooper pairs dominates the tunneling current. Employing $P(E)$ -theory allows us to model experimental $I(V_J)$ characteristics from voltage-biased experiments and determine experimental values of the Josephson critical current in agreement to theory. Moreover, we observe a breakdown of $P(E)$ -theory for experiments at large values of the tunneling conductance $G_N \approx G_0$, which could indicate that the coherent tunneling of Cooper pairs strongly contributes to the tunneling current in this limit. We also observe that the Josephson junction in an STM at temperatures well below 100 mK is highly sensitive to its electromagnetic environment that results from its tiny junction capacitance of a few femtofarads. The combination of the experimental results with numerical simulations reveals that the immediate environment of the Josephson junction in an STM is frequency-dependent and, additionally, that a typical STM geometry shares the electromagnetic properties of a monopole antenna with the STM tip itself acting as the antenna rod. Comparing the $I(V_J)$ curves of voltage-biased and current-biased experiments, we observe that the time evolution of the junction phase is strongly effected by dissipation due to quasiparticle excitations. From investigations on the retrapping current I_R , we show first that the temporal evolution of the junction phase in our STM satisfies a classical equation of motion. Second, we can determine two different channels for energy dissipation of the junction phase. For tunneling resistance values of $R_N \leq 150 \text{ k}\Omega$ the junction dissipates via Andreev reflections, whereas for larger values of $R_N \geq 150 \text{ k}\Omega$ energy dissipation is dominated by the lifetime effects of Cooper pairs. Moreover, from comparing both experiments we also observe that the quantum-mechanical nature of the junction phase manifests in quantum-mechanical phenomena, such as phase tunneling, which strongly alter our experimental $I(V_J)$ characteristics for $G_N \leq G_0$.

To conclude, within this thesis we characterized the properties of a Josephson junction in an STM that is operated at millikelvin temperatures. Hence, this work represents necessary and fundamental steps that allows us to employ the Josephson effect as a versatile probe on the atomic scale.

Acknowledgements

Key words: *Josephson Effect, Scanning Tunneling Microscopy (STM), Josephson Scanning Tunneling Microscopy (JSTM), Dynamical Coulomb Blockade, Quasiparticle Dissipation*

Zusammenfassung

Das Ziel der vorliegenden Dissertation ist zunächst die Eigenschaften eines Josephson Tunnelkontakts in einem Rastertunnelmikroskop (RTM) bei Millikelvin-Temperaturen zu bestimmen und dadurch Josephson RTM (JRTM) als eine vielseitig einsetzbare Sonde auf atomarer Ebene zu etablieren. Hierfür untersuchten wir die Eigenschaften der $I(V_J)$ -Spektren des Josephson Tunnelkontaktes in unserem RTM bei einer Basistemperatur von 15 mK mittels strom- und spannungsgetriebener Experimente. Für den Tunnelbereich, $G_N \ll G_0$, ergaben die Untersuchungen, dass sich der Josephson Tunnelkontakt innerhalb des dynamischen Coulomb-Blockade (DCB) Regimes befindet, in welchem das sequentielle Tunneln von Cooper-Paaren den Tunnelstrom dominiert. Mit Hilfe der sogenannten $P(E)$ -Theorie konnten wir sowohl die experimentellen $I(V_J)$ -Spektren aus spannungsgetriebenen Experimenten fiten als auch experimentelle Werte des kritischen Josephson Stromes bestimmen. Darüberhinaus stellten wir fest, dass diese experimentellen Werte mit theoretisch berechneten Werten übereinstimmen. Des Weiteren ergaben unsere Untersuchungen, dass die bei großen Leitfähigkeitswerten des Tunnelkontakts, $G_N \approx G_0$, gemessenen Cooper-Paar Tunnelspektren nicht mehr mit Hilfe der $P(E)$ -Theorie beschrieben werden können. Dies könnte darauf hinweisen, dass das kohärente Tunneln der Cooper-Paare wesentlich zu dem Tunnelstrom unter dieser Bedingung beiträgt. Wir beobachteten auch, dass der Josephson Effekt in einem STM bei Temperaturen von deutlich weniger als 100 mK höchst empfindsam gegenüber seiner elektromagnetischen Umgebung ist, was von der äußerst geringen Tunnelbarrierenkapazität von wenigen Femtofarad herrührt. Der Vergleich der experimentellen Daten mit einer numerischen Simulation zeigte, dass die unmittelbare Umgebung des Josephson Tunnelkontaktes in einem RTM frequenzabhängig ist, und des Weiteren, dass die typische Geometrie eines RTM die elektromagnetischen Eigenschaften einer Monopolantenne teilt, wobei die RTM Spitze der Antenne entspricht. Der Vergleich der $I(V_J)$ -Spektren von spannungs- mit stromgetriebenen Experimenten ergab, dass die Zeitentwicklung der Phase in hohem Maße durch die Energiedissipation mittels der Anregung von Quasiteilchenzuständen beeinflusst wird. Durch die Untersuchung des „Rückfallstroms“ I_R konnten wir nachweisen, dass (a) sich die Zeitentwicklung der Phase durch eine klassische Bewegungsgleichung beschreiben lässt, und (b) zwei verschiedene Dissipationskanäle existieren. Bei kleineren Tunnelwiderstandswerten von $R_N \leq 150 \text{ k}\Omega$ erfolgt die Energiedissipation über Andreev Reflektionen, wohingegen für größere Werte des Tunnelwiderstands von $R_N \geq 150 \text{ k}\Omega$ die Energiedissipation von Lebenszeiteffekten der Cooper-Paare dominiert wird. Darüberhinaus ergab der Vergleich beider Experimente, dass sich der quantenmechanische Ursprung der Phase in verschiedenen Phänomenen äußert, welche in starkem

Acknowledgements

Maße die experimentellen $I(V)$ -Charakteristika unserer Experimente für $G_N \approx G_0$ verändern. In summa wurden in dieser Dissertation die Eigenschaften des Josephson Tunnelkontaktes in einem STM bei Milli-Kelvin-Temperaturen bestimmt. Daher stellt diese Arbeit notwendige und grundlegende Schritte dar, welche es uns ermöglichen werden, den Josephson Effekt als eine vielseitige Sonde auf atomarer Ebene einzusetzen.

Aus dem Englischen übersetzt von Dr. Herbert Jäck

Stichwörter: *Josephson Effekt, Rastertunnelmikroskop (RTM), Josephson-Rastertunnelmikroskop (JRTM), Dynamische Coulomb Blockade, Quasiteilchen Dissipation*

Résumé

L'objectif de cette thèse est de caractériser les propriétés d'une jonction de Josephson dans un microscope à effet tunnel (STM) à des températures millikelvin et de mettre en application le microscope à effet tunnel Josephson (JSTM) comme sonde polyvalente à l'échelle atomique. Pour y parvenir, nous examinons les caractéristiques de tunnel $I(V_J)$ de la jonction de Josephson dans notre microscope à effet tunnel (STM) à la température de référence de 15 mK au moyen d'expériences à courant polarisé et tension polarisée. Nous observons que dans le régime tunnel $G_N \ll G_0$, la jonction de Josephson fonctionne au régime du blocage dynamique de Coulomb (DCB), pendant lequel l'effet tunnel séquentiel des paires de Cooper domine le courant de tunnel. L'utilisation de la théorie $P(E)$ nous permet de modéliser expérimentalement les caractéristiques $I(V_J)$ des expériences à tension polarisée et de déterminer expérimentalement les valeurs du courant critique de Josephson en accord avec la théorie. De plus, nous observons une rupture de la théorie $P(E)$ pour les expériences à haute valeurs de conductance de tunnel $G_N \approx G_0$, ce qui pourrait indiquer que l'effet de tunnel cohérent des paires de Cooper contribue fortement au courant de tunnel dans cette limite. Nous observons également que la jonction de Josephson dans un microscope à effet tunnel (STM) à températures moins de 100 mK est extrêmement sensible à son environnement électromagnétique ce qui résulte de sa faible capacité de jonction de l'ordre de quelques femtofarads. En combinant l'expérience à des simulations numériques, il apparaît que l'environnement immédiat de la jonction de Josephson dans un microscope à effet tunnel dépend de la fréquence et que de plus, la géométrie typique d'un microscope à effet tunnel partage les propriétés électromagnétiques d'une antenne monopôle, la pointe du microscope agissant comme l'antenne. En comparant les courbes $I(V_J)$ des expériences à courant polarisé et tension polarisée, nous trouvons que l'évolution temporelle de la phase est fortement affectée par la dissipation due à l'excitation des quasi-particules. À partir de l'étude du courant de retrapping I_R , nous pouvons tout d'abord montrer que l'évolution temporelle de la phase de jonction dans notre microscope à effet tunnel satisfait à l'équation classique du mouvement. Ensuite, nous pouvons déterminer deux canaux quant à la dissipation d'énergie de la phase de jonction. Pour des valeurs de résistance de tunnel $R_N \leq 150 \text{ k}\Omega$ la jonction dissipe via des réflexions d'Andreev tandis que pour de plus grandes valeurs de résistance $R_N \geq 150 \text{ k}\Omega$, la dissipation de puissance est déterminée par la longévité des paires de Cooper. De plus, à partir de la comparaison des deux expériences, nous pouvons observer que la nature quantique de la jonction se manifeste au cours de phénomènes mécaniques quantiques, tels que la phase de l'effet tunnel qui change fortement les caractéristiques $I(V_J)$ pour $G_N \leq G_0$.

Acknowledgements

Pour conclure, dans le cadre de cette thèse, nous caractérisons les propriétés de la jonction de Josephson dans un microscope à effet tunnel, fonctionnant à des températures millikelvin. En conséquence, ce travail présente les étapes fondamentales nécessaires qui permettent d'employer l'effet Josephson comme sonde polyvalente à l'échelle atomique.

Traduit de l'anglais par Thierry Gentès

Key words : *Effet Josephson, Microscope à effet tunnel (STM), Microscope à effet tunnel Josephson (JSTM), Blocage dynamique de Coulomb, Dissipation de quasi-particule*

Contents

Acknowledgements	i
Abstract (English/Deutsch/Français)	iii
List of figures	xiii
List of tables	xvii
Abbreviations	xix
1 Introduction	1
2 Fundamental Theory of Tunneling with Superconductors	5
2.1 Microscopic Theory of Superconductivity	5
2.2 The Tunneling of Quasiparticles and Cooper Pairs	9
2.2.1 The Tunneling Effect	9
2.2.2 Tunneling of Quasiparticles	9
2.2.3 Andreev Reflections	12
2.2.4 Finite Lifetime Effects of Cooper Pairs on the Superconducting Density of States	14
2.2.5 Tunneling of Cooper Pairs - The Josephson Effect	14
2.3 Dynamics of the Junction Phase $\phi(t)$	17
2.4 Thermal Fluctuations of the Junction Phase $\phi(t)$	20
2.5 Quantum Mechanics of a Josephson junction	23
3 Experimental	27
3.1 Scanning Tunneling Microscopy	27
3.2 Experimental Requirements for JSTM	29
3.2.1 Mechanical Stability	30
3.2.2 Refrigeration to Millikelvin Temperatures	31
3.2.3 Electronic Temperature and Energy Resolution	32
3.3 Sample and Tip Preparation	35
3.3.1 Preparation of Vanadium (001) Single Crystal	35
3.3.2 Preparation of Vanadium Tips	36
3.4 Measurement Circuit	36

Contents

3.5	Experimental Procedure	38
4	The Critical Josephson Current in the Dynamical Coulomb Blockade Regime	41
4.1	Introduction	41
4.2	$P(E)$ -Theory	43
4.2.1	Numerical Computation of the $P_Z(E)$ Distribution for an Arbitrary Impedance $Z_t(\nu)$	47
4.2.2	Thermal Broadening of the $P(E)$ Distribution due to Thermal Voltage Noise \bar{u} & Calculation of the Total $P(E)$ Distribution	48
4.3	The Environmental Impedance of a Typical STM Geometry	49
4.4	Implementation of $P(E)$ -Theory as Fitting Routine	51
4.5	Testing the Range of Validity for $P(E)$ -Theory	52
4.6	The Josephson Critical Current in the Dynamical Coulomb Blockade Regime	58
4.7	Conclusion	60
5	The AC Josephson Effect as a GHz Source on the Atomic Scale	63
5.1	Introduction	63
5.2	Tuning the Tip Eigenmodes	64
5.3	Numerical Simulations of the Environmental Impedance	68
5.4	Features and Perspectives of the AC Josephson STM	71
5.5	Conclusion	73
6	Phase Dynamics of an Atomic Scale Josephson Junction	75
6.1	Introduction	75
6.2	Defining the Quantum-Mechanical Regime	77
6.3	Theoretical Considerations	79
6.3.1	Retrapping into the Zero Voltage State	80
6.3.2	Stability of the Zero Voltage State	84
6.4	Numerical Simulation of the Phase Dynamics	87
6.5	Comparison of Current-biased and Voltage-biased Experiments	88
6.6	Analysis of the Voltage-biased Experiments	90
6.7	Analysis of the Retrapping Current	95
6.8	Analysis of the Zero Voltage State	99
6.9	Conclusion	102
7	Conclusion & Outlook	103
7.1	Conclusion	103
7.2	Outlook	104
7.2.1	JSTM: Probing the Superconducting Ground State	104
7.2.2	Cooper Pairs and Photons I: The AC Josephson Spectrometer	105
7.2.3	Cooper Pairs and Photons II: Nonlinear Cooper Pair Tunnel Effects	106
7.2.4	Tuning the Energy Scales: Coherent vs. Sequential Cooper pair Tunneling	107
7.2.5	Studying the Quasiparticle Dissipation of Josephson Junctions	108

Bibliography	111
Curriculum Vitae	123
Publications	125

List of Figures

2.1	Illustration of Cooper pair formation	6
2.2	Quasiparticle dispersion relation and density of states	8
2.3	Illustration of the tunneling effect	10
2.4	Example of an experimental quasiparticle density of states	12
2.5	Effect of Andreev reflections on the $dI(V)/dV$ spectrum	13
2.6	Illustration of the Andreev reflection process	14
2.7	Finite lifetime effects on the quasiparticle density of states	15
2.8	Classical phase dynamics of a Josephson junction	18
2.9	Tunneling characteristics of an overdamped and an underdamped Josephson junction	20
2.10	Illustration of the phase diffusion process	21
2.11	Influence of phase diffusion on the tunneling characteristics of a Josephson junction	23
2.12	Uncertainty in the junction phase and the charge as a function of charging energy versus Josephson coupling energy	25
3.1	Illustration of STM operation	29
3.2	Illustration of the laboratory hall and the STM head	30
3.3	Illustration of the dilution refrigerator concept and the cryostat as well as of the filtering concept	33
3.4	Scanning Tunneling Microscopy topography of the vanadium(001) surface in two different magnifications	36
3.5	Experimental dI/dV spectrum of a vanadium-vacuum-vanadium junction	37
3.6	Circuit diagrams for voltage-biased and current-biased experiments	37
4.1	Comparison of Josephson coupling energy, capacitive charging energy and thermal energy	42
4.2	Typical $I(V_J)$ tunneling characteristics of a voltage-biased experiment on the Josephson junction in our STM	43
4.3	Illustration of inelastic Cooper pair tunneling in the dynamical Coulomb blockade regime.	44
4.4	Comparison of $P_Z(E)$, which only contains the interaction with an environmental impedance, and the total probability distribution $P(E)$	49

List of Figures

4.5	Electric properties of a typical STM geometry	51
4.6	Example of a $P(E)$ -fit to an experimental Cooper pair tunneling curve from a voltage-biased experiment	53
4.7	$P(E)$ -fits to experimental tunneling curves for different tunneling conductance values	54
4.8	Fit parameter of the $P(E)$ -fits to experimental tunneling curves for different tunneling conductance values	55
4.9	Experimental tunneling spectra for large values of the tunneling conductance .	56
4.10	Investigating the range of validity for $P(E)$ -theory I	57
4.11	Investigating the range of validity for $P(E)$ -theory II	57
4.12	Determination of the superconducting order parameter from experiment . . .	59
4.13	Comparison of experimental and theoretical values of the Josephson critical current	61
5.1	Conceptual sketch of the STM tip $\lambda/4$ -monopole antenna	63
5.2	Experimental tunneling curves for different STM tip lengths	65
5.3	Experimental tunneling curves for different tip holder geometries	66
5.4	Lowest eigenmode frequency ν_0 of the STM tip as a function of the STM tip length	67
5.5	Cross sections of the STM head geometry used for the numerical simulations .	68
5.6	Scattering parameter and impedance of the STM head, as obtained from the numerical simulations	69
5.7	Electric field pattern for the STM geometry, as obtained from the numerical simulations	71
5.8	Extracting quantities from experimental tunneling curves for the approximation of the photon field in the tunneling junction and the resonator excitation lifetime	72
6.1	Comparison of tunneling characteristics from both voltage-biased and current-biased experiments on the Josephson junction in our STM	75
6.2	Classical and quantum mechanical representation of the junction phase	76
6.3	Calculated eigenfunctions of the junction phase in the quantum-mechanical description	78
6.4	Comparison of a calculated ohmic current and a calculated quasiparticle current	81
6.5	Approximation of the dissipation regime for the Josephson junction in our STM	83
6.6	Illustration of phase tunneling processes in different representations	86
6.7	Time evolution of the junction phase as obtained by numerical simulations . .	88
6.8	Tunneling characteristics for different values of the tunneling resistance as obtained from numerical simulations	88
6.9	Comparison of tunneling characteristics from voltage- and current-biased experiments for different values of the tunneling resistance	89
6.10	Consistency check for the experimental values of the tunneling resistance . . .	90
6.11	$P(E)$ -fit to a tunneling curve from voltage-biased experiments	91
6.12	Comparison of experimental and theoretical Josephson critical current values .	92

6.13 Fit parameter, as obtained from the $P(E)$ -fits, as a function of the tunneling resistance	93
6.14 Analysis of the quasiparticle density of states using the extended Maki model .	94
6.15 Comparison of experimental, simulated and fitted retrapping currents	96
6.16 Comparison of experimental and calculated retrapping currents using experimental values of the differential in-gap quasiparticle resistance	97
6.17 Comparison of the Josephson critical current and experimental as well as calculated values of the switching current	100
6.18 Comparison of experimental and calculated zero voltage resistance values as a function of the tunneling resistance	101
7.1 First JSTM results	105
7.2 Outlook on nonlinear Cooper pair photon interaction	107
7.3 Outlook on the transition from sequential to coherent Cooper pair tunneling .	108



List of Tables

3.1	Circuit resistance of voltage biased measurements for different amplification ranges of the current amplifier	38
-----	-------------------------------------------------------------------------------------------------------------------------	----

Abbreviations

A_1	Large surface tip holder
A_2	Small surface tip holder
AC	Alternating current
α	Damping parameter of the STM tip eigenmodes
BCS	Bardeen, Cooper and Schrieffer-type
c, c^\dagger	Normal electron operators
C_J	Junction capacitance
c_2	Parameter of the $P(E)$ -fit, which models the in-gap quasiparticle current
DC	Direct current
Δ	Amplitude of the superconducting order parameter
ΔE	Energy resolution
DCB	Dynamical Coulomb blockade
DOS	Density of states
e	Elementary charge
E_C	Capacitive charging energy
E_J	Josephson coupling energy
E_T	Thermal energy
m	Electron mass
φ	Complex phase of the superconducting order parameter
ϕ	Josephson junction phase
$\hat{\phi}$	Josephson junction phase operator
f_M	Modulation frequency of the lock-in amplifier
FIM	Finite Integral Method
$\tilde{\gamma}, \tilde{\gamma}^\dagger$	Quasiparticle operators
Γ	Cooper pair lifetime parameter
$\tilde{\Gamma}_{k,l}$	Tunneling rate
$G_0 = 2e^2/h$	Quantum of Conductance
G_N	Tunnel conductivity
h	Planck's constant
$\hbar = h/(2\pi)$	Reduced Planck's constant
$^3\text{He}, ^4\text{He}$	Helium isotopes
HF	High-frequency
i	Imaginary number

List of Tables

I	Current
I_0	Josephson critical current
I_B	Bias current output of the current source
I_R	Retrapping current
I_S	Switching current
$I_{S,Z}$	Switching current in the Zener model
$J(t)$	Phase-phase correlation function
$JSTM$	Josephson Scanning Tunneling Microscopy
κ	Decay constant of $\Psi_{k,l}$ inside a tunnel barrier
$\bar{\kappa}$	Short-pass parameter of $Z_T(\nu)$
k_B	Boltzmann's constant
$K(k)$	Jacobi's full elliptic integral of first kind
l	STM tip length
l_0	Electrical lengthening of the STM tip
Λ	Order parameter of the Ginzburg-Landau equation
$M_{k,l}$	Matrix tunnel element
ν	Frequency
ν_n	STM tip eigenmodes
$\hat{n} = \hat{q}/(2e)$	Number operator of the Cooper pairs, which are stored on the junction
$\Psi_{k,l}(z)$	1D electronic wavefunction
$\bar{\Psi}(\phi)$	Wavefunction of the junction phase in phase space
$P(E)$	Energy-dependent probability of a Cooper pair for an inelastic energy exchange process
$P_C(E)$	$P(E)$ distribution for an energy exchange with thermal voltage fluctuations \bar{u}
P_{\max}	Global maximum of the $P(E)$ distribution
P_T	Probability for the junction phase to tunnel through a washboard potential well
$P_Z(E)$	$P(E)$ distribution for an energy exchange with $Z(\nu)$
Q	Junction quality factor
q	Electric charge that is stored on the tunnel junction
\hat{q}	Junction charge operator
$RCSJ$	Resistively and capacitively shunted junction
ρ_N	Normal metal DOS
ρ_S	Superconducting DOS
R_0	Zero voltage resistance of the DC Josephson current
$R_{DC}=Z(0)$	DC contribution to the environmental impedance $Z(\nu)$
R_{eff}	Effective resistance inside the superconducting gap
R_N	Tunnel resistance
$R_Q = h/(4e^2)$	Klitzing's constant for superconductors
R_{QP}	Quasiparticle resistance
R_{QPP}	Quasiparticle-pair interference resistance
Ref	Reference
RF	Radio-frequency
σ_i	Standard deviation of the quantity i

S_{11}	Scattering parameter as obtained from <i>FIM</i> simulations
<i>STM</i>	Scanning Tunneling Microscopy
T	Temperature
T_C	Critical temperature of a superconductor
T_{eff}	Effective electronic temperature
\tilde{U}	Washboard potential barrier height
\bar{u}	Thermal voltage noise on C_J
<i>UHV</i>	Ultra-high vacuum
V	Voltage
V_B	Bias voltage output of the voltage source
V_J	Voltage across the tunnel junction
V_M	Modulation amplitude of the lock-in amplifier
ω_0	Josephson plasma frequency
$Z(\nu)$	Frequency-dependent environmental impedance
$Z_T(\nu)$	Frequency-dependent environmental impedance that is shunted by C_J

1 Introduction

In the year of 1962, the Cambridge student Brian D. Josephson theoretically investigated possible tunneling phenomena in superconductor-insulator-superconductor tunnel junctions. Remarkably, for his theoretical considerations Josephson threw over with the hypothesis that superconducting particles, the *Cooper pairs*, can not cross a tunnel barrier, a hypothesis that was established from leading theoreticians in the field of superconductivity¹ [2, 3]. In contrast to the concept given by Bardeen [2, 3], Josephson assumed that the wavefunction of this ground state behaves similarly to normal electron wavefunctions and exhibits an exponential decay outside the superconducting material. As a consequence, the wavefunctions of two superconducting ground states separated by an oxide barrier could also overlap inside the barrier and enable the tunneling of Cooper pairs, similar to the tunneling of single electrons that had been experimentally demonstrated just a few years earlier by Ivar Giaever [4, 5]. Based on this idea, Josephson theoretically predicted the “Josephson effect“ which involves the tunneling of Cooper pairs and manifests in two different phenomena. First, the DC Josephson effect describes the dissipationless tunneling of Cooper pairs, which allows one to observe a tunneling current at zero voltage. Second, the AC Josephson effect describes the Cooper pair transfer across the tunnel barrier via absorbing a photon of energy $E = h\nu$ and therefore acts as a perfect voltage V_J to frequency ν converter $2eV_J = h\nu$, where e denotes the elementary charge and h denotes Planck’s constant.

The underlying mechanism of the Josephson effect has strong connection to the superconducting ground state, which represents a macroscopic quantum state [1]. In detail, each ground state can be described by its complex order parameter $\Delta = |\Delta| \exp(i\varphi)$ that is of amplitude Δ – denoting the coupling energy of the electrons in a Cooper pair – and phase φ . For disjoint superconducting reservoirs, e.g. two superconducting electrodes separated by a thin oxide tunneling barrier², the phase values φ of each reservoir are independent so that a phase differ-

¹In 1957, Bardeen, Cooper and Schrieffer (BCS) obtained a theoretical model that successfully describes how superconductivity develops in a microscopic picture [1]. They showed that an attractive interaction between electrons leads to the formation of a macroscopic ground state characterized by its order parameter Δ . Microscopically, the attractive interaction, mediated by small lattice distortions, promotes the formation of Cooper pairs that consist of two electrons of opposite spin and opposite momentum.

²In fact, the Josephson effect can be observed in any sample in which two superconducting reservoirs are

ence $\phi = \varphi_1 - \varphi_2$ between the two reservoirs can exist. Josephson could show that this phase difference ϕ of the coupled wavefunctions is the driving force for a Cooper pair tunneling current I across the barrier [7]

$$I = I_0 \sin(\phi), \quad I_0 = \frac{\pi}{2} \frac{\Delta}{R_N}, \quad (1.1)$$

where the amplitude of this current, I_0 , called the Josephson critical current, is solely determined by the superconducting order parameter Δ and the tunneling resistance R_N of the barrier [8].

Only one year after their prediction in 1962 both the DC and AC Josephson effect were experimentally observed in tunnel experiments on superconductor insulator superconductor junctions [9, 10]. Although Josephson's theoretical work was initially questioned, the experimental proof of the Josephson effect ignited tremendous research on these Cooper pair tunneling phenomena which ultimately resulted in a variety of applications. These are, for instance, the SQUID, which is a highly sensitive magnetometer that has been established as a standard tool in magnetometry [11]. A second application of the Josephson effect is the so-called Josephson phase qubit which serves as a central building block for the currently most sophisticated approach to quantum computing [12]. Moreover, the national institutes of metrology exploit the AC Josephson effect as a voltage standard that precisely defines the electric potential [13].

Apart from these successful applications the Josephson effect has also high potential to be employed as a probe on the local scale. The combination of the Josephson effect with Scanning Tunneling Microscopy (STM), also referred to as Josephson Scanning Tunneling Microscopy (JSTM) [14], can serve as an ideal probe for studying, for instance, superconductivity. In detail, one takes advantage of the Cooper pair current being sensitive to both the amplitude of the superconducting order parameter Δ as well as to the phase φ . These features allow one to address open questions on the symmetry of the superconducting order parameter in non-conventional superconductors, such as Cuprates [14, 15]. JSTM represents also an ideal tool to study how the superconducting state responds to perturbations that can be introduced by a single magnetic atom on top of a superconducting surface, for instance [16]. For such a system, theory predicts a strong response of the superconducting state, which manifests itself in variations of Δ , including even changes of sign [17, 18]. However, in experiments on such systems no change in the amplitude of Δ was observed so far [16, 19, 20]. This is most likely due to the reason that *standard* tunnel experiments probe the energy of so-called quasiparticles that result from breaking up a Cooper pair [4, 5]. Therefore, these experiments are not a direct probe of the order parameter Δ itself. Here, JSTM provides clear advantages and could help to shed more light on the fundamental interaction between superconductivity and magnetism [20], a question that is nowadays also highly discussed in the context of iron-based superconductors [21].

connected via a *weak link*. The term weak link can be realized via a short constriction, a normal metallic film or just an insulating film [6].

The AC Josephson effect also has large potential to be employed in JSTM experiments, since it perfectly converts voltages to frequencies. It was shown in experiments on planar Josephson junctions that the AC Josephson effect can be employed to sense hyperfine transitions in rare earth atoms inside the tunnel barrier or to prove the existence of the Andreev bound state in superconducting atomic point contacts [22, 23]. This spectroscopic feature of the *AC Josephson spectrometer* is certainly also of interest in STM experiments. Here, it could be employed to investigate the spin state of molecular magnets [24], which are a promising candidate for molecular electronics, or even probe the hyperfine transitions of single atoms carrying a nuclear spin [25].

The diversity of the given examples illustrates that the combination of the Josephson effect and STM represents a promising tool in solid state physics and surface science. For this reason, JSTM already attracted some experimental interest [26, 27, 28, 29, 30], yet it never experienced a real breakthrough. The reason for the limited success may be found in the very small coupling strength between the two superconducting wave functions when compared to other relevant energy scales in experiments, such as thermal energy $E_T = k_B T$ (k_B denotes Boltzmann's constant and T the temperature). The condition for Josephson STM to work, as given in Ref. [14], requires that the Josephson coupling energy E_J exceeds thermal energy E_T such that the coupling between the superconductors is not perturbed by thermal fluctuations [31]. For STM experiments with elemental superconductors E_J is typically smaller than $20 \mu\text{eV}$, which requires experimental temperatures of $T \leq 250 \text{ mK}$. All attempts on JSTM so far [26, 27, 28, 29, 30] have been performed at much higher temperatures so that the condition for JSTM to work were clearly violated. Since recently these necessary very low temperatures are also accessible to STM setups [32, 33, 34, 35, 36] so that it would now be appropriate to say: JSTM is in the starting blocks.

In this sense the focus of this work will be to bring JSTM from the starting blocks onto the race track, i.e. to fully characterize the properties of a Josephson junction in an STM. To this end, we perform JSTM experiments on the first ultra-high vacuum STM setup capable of reaching an effective electronic temperature far below 100 mK , which is located in the department of Prof. Klaus Kern at the Max-Planck-Institute for Solid Research in Stuttgart, Germany [35]. Of particular interest in this work is the question of how the small STM junction capacitance effects the properties of the Josephson junction. Whereas for large planar junction geometries the capacitive charging energy E_C is negligible [9], the charging energy for an STM junction capacitance of a few femtofarads is of similar magnitude as the Josephson coupling energy. In this situation, the Josephson junction interacts with its immediate environment such that the inelastic tunneling of Cooper pairs can be observed at finite voltages, which is accompanied by photon emission [37, 38, 39]. Additionally, the phase of this type of Josephson junction exhibits strong quantum properties that drastically change the junction characteristics [31, 40, 41]. In fact, the tunneling characteristics of the Josephson junction in our STM are significantly affected by quantum-mechanical phenomena and require a detailed investigation. In particular, the determination of experimental values of the Josephson critical current as a probe for the local superconducting order parameter demands an appropriate theoretical description of

the experimental data in view of the successful implementation of JSTM.

At this point it should be noted that JSTM also allows one to continuously tune the Josephson coupling energy by changing the tip-sample distance. In this way, JSTM can explore new tunneling regimes and dissipative interactions of the junction with its environment that are inaccessible to experiments on planar junction geometries. In these experiments E_J can not be tuned that easily. The tunability of E_J versus E_C is of particular interest in the context of *Hamiltonian by design* to optimize the properties of phase qubits for quantum computing [12]. Hence, JSTM also represents ideal means to address fundamental questions of superconducting tunneling, which extends and complements the diverse portfolio of this highly interesting technique.

The outline of this thesis is the following: The focus of Chapter 2 is to provide a theoretical background on superconductivity as well as on the tunneling phenomena of single particles and Cooper pairs. In addition, some general aspects of the Josephson effect are presented that help the reader to obtain a fundamental understanding of this effect, whereas detailed theory is given in the corresponding chapters where needed. Chapter 3 is focused on experimental aspects of this study, such as the functionality of an STM, refrigeration using a dilution refrigerator and aspects on the sample preparation and measurement procedures. In Chapter 4, we investigate the tunneling characteristics of voltage-biased Josephson junctions and implement theory that allows us to extract the Josephson critical current from the experimental data. In Chapter 5, we show that the atomic scale Josephson junction in our STM is sensitive to high-frequency signals in the GHz range and, moreover, we demonstrate the realization of the AC Josephson spectrometer in an STM. In Chapter 6, we investigate the dynamics of the phase difference ϕ and its dissipative interaction with quasiparticle excitation processes. Moreover, we compare the experimental results from current-biased and voltage-biased experiments in order to understand how significantly quantum mechanics effects the properties of the Josephson junction. Chapter 7, summarizes all results obtained in this work and provides an outlook on perspective experiments as well as first results of JSTM on the interaction of a single magnetic impurity with a superconducting ground state.

2 Fundamental Theory of Tunneling with Superconductors

The goal of this chapter is to provide the reader with theoretical basics of tunneling between superconducting electrodes. These involve the microscopic description of superconductivity by Bardeen, Cooper and Schrieffer as well as general aspects of the tunnel effect. Second, this chapter includes the derivation of the Josephson equations as well as their generalization and describes fundamental physical aspects of Josephson junctions. The chapter closes with a discussion of the influence of perturbations on the Josephson effect. Further theory that is needed for particular experiments will be considered in the corresponding chapters.

2.1 Microscopic Theory of Superconductivity

The foundation of the modern understanding of superconductivity and related phenomena was set when J. Bardeen, L. N. Cooper and J. R. Schrieffer (BCS) obtained their microscopic description of superconductivity, the BCS theory [1]. This theory succeeded in connecting a quantum-mechanical picture of particle interactions with the critical temperature T_C of the phase transition, at which a normal metal turns superconducting. The fundamental concept behind this theory is an attractive interaction between electrons in a metal mediated by the crystal lattice. A first indication for this interaction potential was experimentally provided by the so-called *isotope effect*. It was found that the critical temperature T_C depended on the isotope of the specific element, thus on the ion mass. This observation pointed to a significant involvement of the crystal lattice for the formation of the superconducting phase. Based on these experimental results, Fröhlich and Bardeen were able to provide a physical picture as well as a theoretical description for an attractive interaction between electrons [42, 43]: In a simplified picture, when the negatively charged electron moves through the crystal, it will attract positively charged ions sitting on the lattice sites when passing by. This lattice distortion creates a local, positive charge density that creates an attractive, albeit small, potential between a pair of electrons, as shown in Fig. 2.1. Bardeen, Cooper and Schrieffer found that *this* pair of electrons is formed by two electrons of opposite momentum $\pm\mathbf{k}$ and opposite spin $S_z = \pm 1/2$. This particle, called a Cooper pair, is of bosonic nature with a total spin $S = 0$ [1].

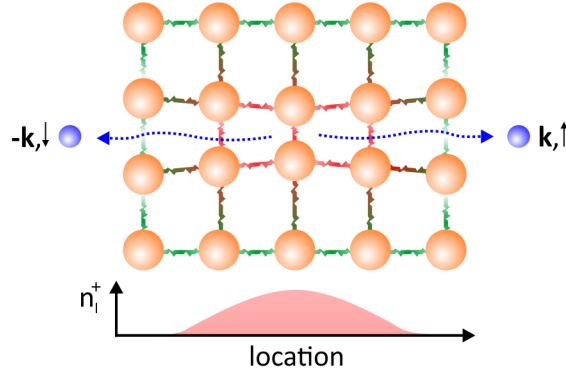


Figure 2.1 – Passing through the crystal lattice of ions (orange circles), the electrons (blue circles) induce a small lattice distortion. This distortion yields a positive, localized space charge n_i^+ , that results in an attractive potential between two electrons of opposite momentum, $\pm\mathbf{k}$, and opposite spin, \uparrow, \downarrow .

To derive an expression for the order parameter of the superconducting phase it is necessary to consider the Hamiltonian of an electronic system that includes this electron-electron interaction potential ζ . For the sake of simplicity, this potential is chosen to be momentum independent. In the framework of BCS theory, this Hamiltonian in second quantization and momentum space reads as:

$$H - \mu N = \sum_{\mathbf{k}, \sigma} \epsilon(\mathbf{k} - \mu) c_{\mathbf{k}, \sigma}^\dagger c_{\mathbf{k}, \sigma} + \zeta \sum_{\mathbf{k}, \mathbf{k}'} c_{\mathbf{k}, \uparrow}^\dagger c_{-\mathbf{k}, \downarrow}^\dagger c_{\mathbf{k}', \downarrow} c_{-\mathbf{k}', \uparrow} + h.c.. \quad (2.1)$$

The first term on the right side of the equation, $\epsilon(\mathbf{k}) = \hbar\mathbf{k}^2/2m$, denotes the kinetic energy of a free electron with respect to the chemical potential μ of a reservoir of N electrons. The particle operators c and c^\dagger annihilate an electron or create an electron of spin state σ , respectively. The second term represents the superconducting ground state, $\sum_{\mathbf{k}'} c_{\mathbf{k}', \downarrow} c_{-\mathbf{k}', \uparrow}$, and its complex conjugate, that result from the attractive interaction ζ . In a more descriptive explanation this last term sums up the entirety of Cooper pairs in the superconducting phase. Since the attractive potential was chosen to be momentum independent, a mean-field approach on the superconducting ground state yields

$$H_{MF} - \mu N = \sum_{\mathbf{k}} \begin{pmatrix} c_{\mathbf{k}, \uparrow}^\dagger & c_{-\mathbf{k}, \downarrow} \end{pmatrix} \begin{pmatrix} \epsilon(\mathbf{k}) - \mu & \Delta \\ \Delta^* & \mu - \epsilon(\mathbf{k}) \end{pmatrix} \begin{pmatrix} c_{\mathbf{k}, \uparrow} \\ c_{-\mathbf{k}, \downarrow}^\dagger \end{pmatrix} - \frac{\Delta^* \Delta}{\zeta}. \quad (2.2)$$

This equation already contains the order parameter of the superconducting phase $\Delta = \zeta \times \sum_{\mathbf{k}} \langle c_{\mathbf{k}, \downarrow} c_{-\mathbf{k}, \uparrow} \rangle$ and its complex conjugate. To calculate the eigenvalue spectrum of the superconducting ground state it is necessary to diagonalize Eqn. 2.2 by rotating the operator basis.

2.1. Microscopic Theory of Superconductivity

This is obtained by the Bogoliubov-transformation, which introduces novel operators

$$\tilde{\gamma}_{1,\mathbf{k}} = uc_{\mathbf{k}\uparrow} + vc_{-\mathbf{k}\downarrow}^\dagger, \quad (2.3)$$

$$\tilde{\gamma}_{2,\mathbf{k}} = -v^*c_{\mathbf{k}\uparrow} + u^*c_{-\mathbf{k}\downarrow}^\dagger, \quad (2.4)$$

where u and v are complex numbers obeying the condition $|u|^2 + |v|^2 = 1$. Within this new basis the mean-field BCS Hamiltonian is diagonalized and reads as

$$H_{MF} - \mu N = \sum_{\mathbf{k}} \begin{pmatrix} \tilde{\gamma}_{1,\mathbf{k}}^\dagger & \tilde{\gamma}_{2,\mathbf{k}}^\dagger \end{pmatrix} \times \begin{pmatrix} E_{\mathbf{k}} & 0 \\ 0 & -E_{\mathbf{k}} \end{pmatrix} \begin{pmatrix} \tilde{\gamma}_{1,\mathbf{k}} \\ \tilde{\gamma}_{2,\mathbf{k}} \end{pmatrix} - \frac{\Delta^* \Delta}{\zeta}. \quad (2.5)$$

$E_{\mathbf{k}} = \pm \sqrt{(\epsilon(\mathbf{k}) - \mu)^2 + |\Delta|^2}$ represents the eigenvalue spectrum of the Hamiltonian, whose momentum dependence, the dispersion relation, is shown in Fig. 2.2(a). It features an energy gap that has twice the width of the order parameter Δ around the Fermi energy $E_F = \mu N$ and a parabolic dispersion to higher and lower energies, respectively. The underlying phenomenon is that the electrons condense at the Fermi energy to form the superconducting ground state $\sum_{\mathbf{k}} c_{\mathbf{k}\downarrow} c_{-\mathbf{k}\uparrow}$. If the energy $E = 2\Delta$ is provided, quasiparticles of this ground state can be excited by the operator $\tilde{\gamma}^\dagger$ having the energy $E_{\mathbf{k}}$. For this reason the $\tilde{\gamma}$ operators are also called *quasiparticle operators*. A more descriptive explanation is obtained in the single particle picture, where electrons form Cooper pairs of zero kinetic and angular momentum energy at the Fermi energy E_F . If the energy $E = 2\Delta$ is provided, a Cooper pair is broken apart and a single electron is generated. This will now behave as a free electron in a metal for which reason it follows its quadratic dispersion relation.

From the dispersion relation $E_{\mathbf{k}}$, it is straightforward to calculate the density of states ρ of the superconductor

$$\rho_S = \frac{dN(E)}{dE} = \frac{dN(\epsilon)}{d\epsilon} \frac{d\epsilon}{dE} = \rho_N \frac{E}{\sqrt{E^2 - \Delta^2}}, \quad (2.6)$$

with ρ_N as the normal metal density of states (DOS). ρ_S is shown in Fig. 2.2(b) and features a singularity at $E = \Delta$ and a gap of width $2\Delta_0$. Its energy dependence is evident when we sum up all states, equally spaced in \mathbf{k} , for all energies $E_{\mathbf{k}}$ of the dispersion relation in Fig. 2.1(a).

To determine the order parameter of the superconducting ground state Δ in BCS theory, it is necessary to perform a self-consistent calculation starting from its definition [1]:

$$\Delta = \zeta \times \sum_{\mathbf{k}} \langle c_{\mathbf{k}\downarrow} c_{-\mathbf{k}\uparrow} \rangle = V \sum_{\mathbf{k}} \left[u^* v \langle \tilde{\gamma}_{1,\mathbf{k}}^\dagger \tilde{\gamma}_{1,\mathbf{k}} \rangle - u^* v \langle \tilde{\gamma}_{2,\mathbf{k}}^\dagger \tilde{\gamma}_{2,\mathbf{k}} \rangle \right]. \quad (2.7)$$

Including a fermionic distribution of quasiparticle states $\langle \tilde{\gamma}^\dagger \tilde{\gamma} \rangle = 1/(\exp(E_{\mathbf{k}}/k_B T) + 1)$, and replacing the sum over all states in momentum space by an energy integral on the normal

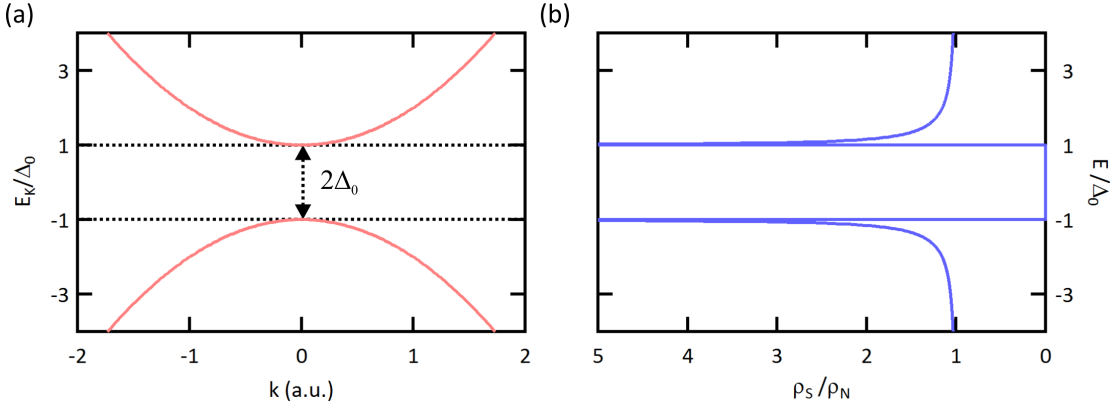


Figure 2.2 – (a) One-dimensional quasiparticle dispersion relation $E_{\mathbf{k}}$ normalized to Δ as a function of momentum k for $E_F = 0$. (b) Quasiparticle density of states ρ_S normalized to the metallic density of states ρ_N as a function of energy E .

density of states ρ_N , some algebra yields:

$$1 = \frac{|\zeta|}{2} \int \rho_N d\epsilon \frac{1}{\sqrt{(\epsilon(\mathbf{k}) - \mu)^2 + |\Delta|^2}} \tanh\left(\frac{\sqrt{(\epsilon(\mathbf{k}) - \mu)^2 + |\Delta|^2}}{2k_B T}\right). \quad (2.8)$$

For temperatures larger than the critical temperature $T > T_C$, the only solution possible is $\Delta = 0$, which is a reasonable result since at this temperature no superconductivity is expected. In the opposite case, $T < T_C$, and assuming that the energy interval $\mu \pm \epsilon_D$ of interaction around the Fermi level μ is determined by the Debye energy ϵ_D – a measure for the excitation energy of phonons – the self-consistent equation for Δ yields a finite value for Δ . Assuming weak electron-phonon coupling an expression for the order parameter in the zero temperature limit Δ_0 can be derived [1]:

$$\Delta_0 = 1.764 k_B T_C. \quad (2.9)$$

This relation between Δ_0 and T_C is of universal validity for all weakly-coupled superconductors and has been experimentally proven for numerous materials.

Although the superconducting order parameter Δ could be derived from a microscopic picture, other important properties were first discovered when Lev Gorkov succeeded in connecting the phenomenological Ginsburg-Landau theory with the microscopic BCS-theory [44]. The Ginsburg-Landau theory is a thermodynamical approach to superconductivity that relates the superconductor's free energy to a complex order parameter of the phase transition Λ [45]. Gorkov found that the microscopically derived order parameter Δ is proportional to Λ . Accordingly, also $\Delta = \Delta e^{i\Phi}$ is complex with a phase Φ , which induces significant consequences as we will see in the next section. Moreover, Gorkov could identify Λ as the wavefunction of Cooper pairs and show that Cooper pairs have an electric charge $q = 2e$.

2.2 The Tunneling of Quasiparticles and Cooper Pairs

To evaluate an expression for the tunneling current that involves superconducting tunneling electrodes, this section will first deal with general aspects of the tunneling effect. This introductory part is followed by theoretical considerations for quasiparticle tunneling, before the Josephson effect itself is introduced. It should be further noted that the following theory is presented in chronological order and mirrors the remarkable progress of theoretical and experimental knowledge on electronic tunneling between the years 1959 and 1961.

2.2.1 The Tunneling Effect

The tunneling effect is a manifestation of the fundamental concept in quantum mechanics where a particle is described by a probability wavefunction $\Psi(\mathbf{x}, \mathbf{k})$. This wavefunction represents the probability to find the particle at location \mathbf{x} having the momentum $\mathbf{k} = \mathbf{p}/\hbar$. If such a quantum-mechanical particle, an electron for instance, is located nearby a barrier of finite width and finite height, its wavefunction will not immediately stop at the barrier, but penetrate through and decay behind it as illustrated in Fig. 2.3(a). To a certain probability the electron can therefore be found behind the barrier; it has *tunneled through* the barrier. Experimentally, this *tunnel effect* was first observed in 1897 by Robert W. Wood investigating the field emission of electrons into vacuum. However, he was not able to describe it, since, at this time, the quantum-mechanical concept was unknown. Twenty years later F. Hund succeeded in explaining the tunnel effect, observed in experiments on molecular isomers, in a quantum-mechanical fashion before, one year later, G. Gamow could derive a mathematical description for this effect starting from the quantum-mechanical Schrödinger equation [46].

The distance behind the barrier at which the tunnel effect can still be observed, relates to the properties of the barrier and the wavefunction. Considering, for instance, the interface of a bulk piece of metal and vacuum as a barrier for the electronic wavefunction Ψ inside the metal, its extension into the vacuum will be on the order of nanometers. Accordingly, when two pieces of metal are separated by such a small distance the wavefunctions of both metals will overlap, as shown in Fig. 2.3(b). This situation is called *tunnel contact* and offers a possibility to measure the quantum-mechanical tunnel effect using electrons: If an external voltage V is applied to such a contact, electrons can tunnel from an occupied electronic state Ψ_k in one electrode into an unoccupied state Ψ_l in the other one and therefore, a tunneling current can be measured.

2.2.2 Tunneling of Quasiparticles

First tunneling experiments were performed on devices having one superconducting and one metallic electrode, which are separated by a thin insulating oxide layer [47, 4, 5]. The experimental results on the measured tunneling current $I(V)$ confirmed that it originates from an overlap of wavefunctions in the tunnel barrier. It was further observed that the

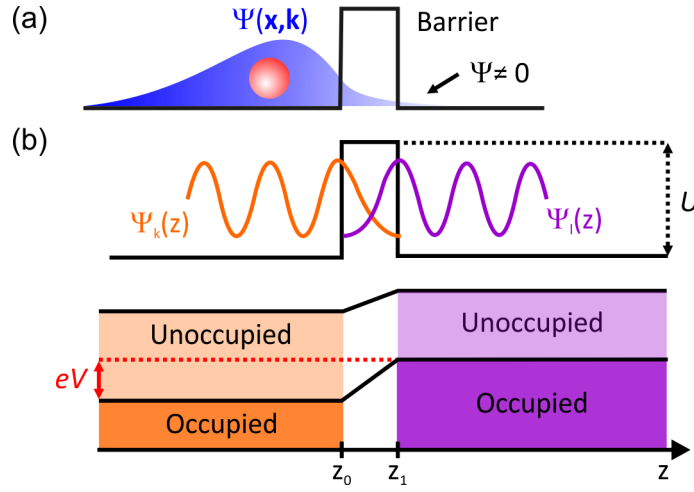


Figure 2.3 – (a) Classical and quantum-mechanical representation of a particle: The red dot is either on the right or the left side of the barrier, showing classical behavior. In contrast, a quantum-mechanical particle represented by a wavefunction has – as a result of the tunneling effect – a probability to be found on both sides. (b) Tunneling of an electron between two electrodes: The wavefunctions $\Psi_k(z)$ and $\Psi_l(z)$, representing single electrons, overlap in the tunnel barrier of height U . If a voltage V is applied, electrons can tunnel from an occupied state in one electrode to an unoccupied state in the other electrode.

measured differential conductance dI/dV directly relates to the density of states (DOS) of the superconductor $\rho_l(E)$, for which reason the tunneling current has to be related to quasiparticle tunneling [47, 4, 5]. Interestingly, these first measurements on electron tunneling were already performed on devices involving superconducting electrodes. This could be possibly explained by the fact that the superconducting DOS has strong features compared to DOS of a normal metal.

Stimulated by these experimental studies, Bardeen could draft a first theoretical picture for the electronic tunneling process: The starting point is the assumption that the electronic wavefunctions of both electrodes, including the superconductor, are free electron plane wavefunctions $\Psi_{k,l}$, which exponentially decay inside the potential barrier ($z_0 < z < z_1$) of height U , as shown in Fig. 2.3(b). These wavefunctions, where \hat{z} corresponds to the direction normal to the interface S in the $\hat{x}\hat{y}$ -plane, read as:

$$\Psi_{1,k,l}(z) \propto \sin(k_z z) \quad (2.10)$$

$$\Psi_{2,k,l}(z) \propto \exp(\kappa z), \quad z_0 < z < z_1. \quad (2.11)$$

Here, $\kappa = \sqrt{2mU/\hbar^2}$ denotes the decay constant of the wavefunction inside the barrier. Including these wavefunctions in time-dependent perturbation theory, Bardeen could derive expressions for both the tunneling matrix element $M_{k,l}$ – containing the overlapping wavefunctions across the entire tunnel contact surface area S – and the energy-dependent tunneling

2.2. The Tunneling of Quasiparticles and Cooper Pairs

rate $\tilde{\Gamma}_{k,l}(E)$ [2]:

$$M_{k,l} = -\frac{i}{2m} \int d\mathbf{S} \Psi_{2,k}^* \frac{\partial \Psi_{2,l}}{\partial z} - \Psi_{2,l} \frac{\partial \Psi_{2,k}^*}{\partial z}, \quad (2.12)$$

$$\tilde{\Gamma}_{k,l}(E) = (2\pi/\hbar) |M_{k,l}|^2 \rho_l(E) f_k(E) (1 - f_l(E)). \quad (2.13)$$

With this result it was, for the first time, possible to qualitatively describe an experimentally determined tunneling spectrum between a normal metallic and a superconducting electrode. However, Bardeen argued, referring to Gorkov's work, that the superconducting order parameter drops to zero rapidly inside the barrier so that a paired wavefunction cannot exist in this region [2]. Accordingly, the sole difference to tunneling experiments with normal metallic electrodes arises from the superconducting DOS [2, 3], a conclusion that clearly was proven incorrect later on.

A more general picture on the tunneling between a metallic and a superconducting electrode was derived one year later by Marvin H. Cohen *et al.*, as an extension to Bardeen's work in a manybody calculation [48]. The starting point of this calculation is the Hamiltonian of that system including a term for interaction,

$$H = H_N + H_S + H_T. \quad (2.14)$$

It contains the normal conducting electrode H_N that corresponds to the normal conducting part of Eq. 2.1, the superconducting electrode H_S , which in a similar fashion contains the number operators $N_S = \langle \tilde{\gamma}^\dagger \tilde{\gamma} \rangle$ of the quasiparticle operators (see Eq. 2.3), and an interaction Hamiltonian H_T :

$$H_T = \sum_{k,l,\sigma} [M_{k,l} c_{k,\sigma}^\dagger c_{l,\sigma} + M_{l,k} c_{l,\sigma}^\dagger c_{k,\sigma}]. \quad (2.15)$$

As in Sec. 2.1 the operators c, c^\dagger denote single electron particle operators and the matrix element $M_{k,l}$ is similar to Eq. 2.12, denoting the overlap of *normal* electronic wavefunctions in the barrier (similar to Bardeen's approach). In this picture the tunneling rate corresponds to the expectation value of the change in quasiparticles in the superconducting electrode $\langle \dot{N}_S \rangle$. Starting from the equation of motion of the quasiparticle number operator $i\hbar \dot{N}_S = [N_S, H_T]$, Cohen *et al.* succeeded in deriving an expression for the tunneling rate $\tilde{\Gamma}$ that depends on the applied voltage V [48]:

$$\tilde{\Gamma}(V) = \langle \dot{N}_S(V) \rangle \propto \int_{-\infty}^{\infty} |M|^2 [f_N(E' - eV) - f_S(E')] \rho_N(E' - eV) \rho_S(E') dE'. \quad (2.16)$$

This equation reveals that the tunneling rate of a superconductor-insulator-metal junction corresponds to the convolution of the superconducting DOS ρ_S (see Eq. 2.6) with the normal conducting DOS ρ_N . In good approximation, ρ_N is constant around the Fermi energy on an interval relevant for superconductivity, $\Delta E \approx 1$ meV (this assumption holds for all elemental

superconductors). For this reason, an experimentally determined differential conductance spectrum $dI(V)/dV$, as shown Fig. 2.4, will be similar to the theoretical superconducting DOS ρ_S (cf. Fig. 2.2(b)). Yet, deviations from an ideal BCS gap, as introduced in Sec. 2.1, can be observed such as a finite width in the quasiparticle excitation peaks, as indicated by the arrows. These deviations can originate from thermally excited quasiparticles, lifetime effects of Cooper pairs and so called Andreev-reflections. For the experiments performed in this work at a temperature of $T = 15$ mK (cf. Ch. 3), thermally excited quasiparticles can be neglected, since thermal energy $k_B T \approx 3.5 \mu\text{eV}$ is negligibly small compared to typical BCS gaps on the order of $\Delta \gg 100 \mu\text{eV}$. The latter two effects will be addressed in the following two subsections.

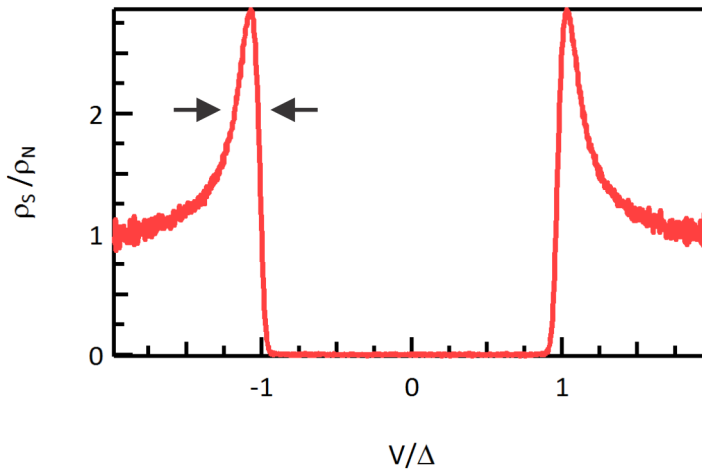


Figure 2.4 – Experimental $dI(V)/dV$ spectrum as a function of the applied voltage bias V measured at a temperature $T = 15$ mK with the voltage axis normalized to the superconducting order parameter Δ . As electrode material we used vanadium, which is a typical BCS superconductor, as the STM tip and a Cu(100) surface as the sample.

2.2.3 Andreev Reflections

In the last section it was shown that the differential tunneling conductance $dI(V)/dV$ of a superconductor-insulator-metal junction is similar to the superconducting DOS as given in Eq. 2.6 and Fig. 2.2. Hence, the $dI(V)/dV$ spectrum should only feature the sharp coherence peaks symmetrically centered around the Fermi energy and an empty gap region. However, a filling of the gap could also be observed experimentally when the tunnel contact resistance R_N was drastically reduced to smaller values. These *in-gap* features originate from pair creation processes via quasiparticle tunneling and were predicted by Andreev just two years after Cohen’s work on superconducting tunneling [49]. For this reason these processes are called Andreev reflections. These reflections involve an electron in the metallic electrode that is reflected by the tunnel barrier as a hole. In order to conserve charge and energy, this process creates a Cooper pair in the superconducting electrode on the other side of the barrier upon

2.2. The Tunneling of Quasiparticles and Cooper Pairs

reflection of the hole ¹. Since this process involves the transfer of two particles across the tunnel barrier the tunneling probability of this process depends on the tunneling resistance as $1/R_N^2$.

Tinkham *et al.* [50] succeeded in deriving a theoretical model that relates the closing of the gap to a so-called barrier parameter Z . Although it is difficult to relate this barrier parameter to the real tunnel contact resistance Fig. 2.5 already gives an impression of this *gap-filling* effect. For a vanishing tunnel barrier, $Z = 0$, the electrodes are in metallic contact and the superconducting gap is filled up, exhibiting a table-like plateau. In the opposite case of a strong barrier, $Z = 10$, the gap remains open. This latter situation corresponds to the experimental situation of a tunnel contact, i.e. $R_N \gg 1/G_0$.

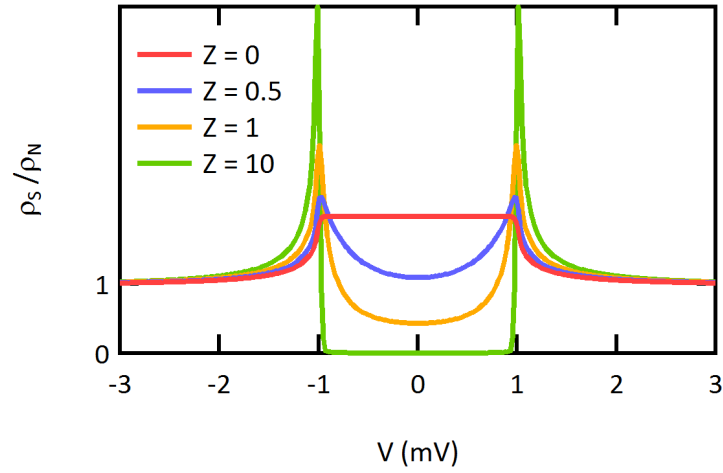


Figure 2.5 – Calculated differential tunneling conductance $dI(V)/dV$ as a function of the barrier parameter Z [50].

Replacing the metallic electrode by a second superconducting electrode with the same gap Δ enables the observation of further Andreev reflections inside the gap [51, 52]. If the voltage drop across the tunnel junction corresponds to the gap value, $eV = \Delta$, an electron can be reflected as a hole and a Cooper pair is created, as illustrated by Fig. 2.6. This process manifests itself as a defined peak inside the superconducting gap at $eV = \Delta$. If the two gaps are of different value it is even possible to observe *multiple Andreev reflections* (MAR), which involves the transfer of more than two quasiparticles. These processes yield in-gap structures at $eV = (\Delta_1 + \Delta_2)/n$. However, their experimental observation is more challenging due to the reduced tunneling probability, which is proportional to $1/R_N^n$. A nice experimental work on these MAR structures, which was also performed using an STM, is given in Ref. [53].

¹Certainly, this process also occurs in the opposite direction via the annihilation of a Cooper pair.

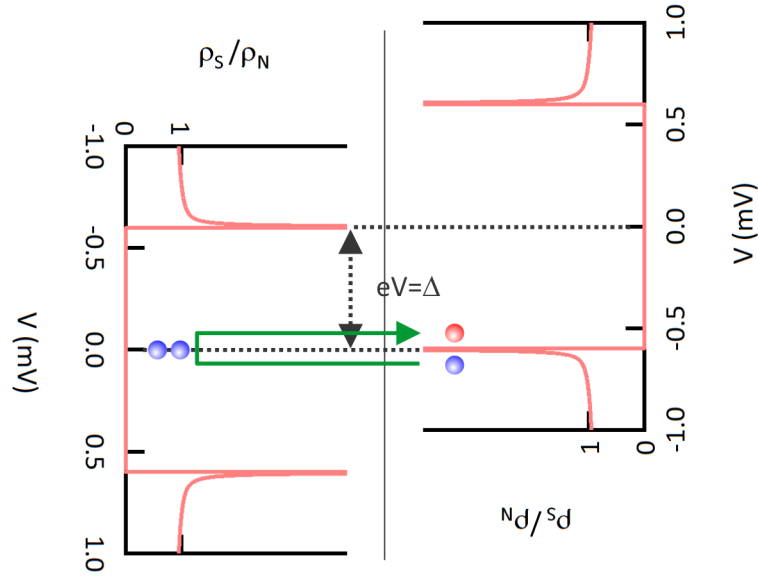


Figure 2.6 – Illustration of the two-particle Andreev reflection that generates a Cooper pair at voltage $V = \Delta$ [51].

2.2.4 Finite Lifetime Effects of Cooper Pairs on the Superconducting Density of States

In many experiments the observed superconducting DOS deviates from the perfect case displayed in Fig. 2.2. The coherence peaks do not appear perfectly sharp but instead are broadened and are of finite width. The origin of this broadening can be manifold, such as a finite lifetime of Cooper pairs due to scattering at surfaces or spin-orbit effects in heavy superconductors. Yet, this experimentally observed broadening can be addressed phenomenologically by introducing a so-called lifetime parameter Γ , as proposed by Dynes *et al.* [54]. This lifetime parameter is simply added to the superconducting DOS in Eq. 2.6, which modifies to

$$\rho'_S(E) = \rho_N \Re \left[\frac{E - i\Gamma}{\sqrt{(E - i\Gamma)^2 - \Delta^2}} \right]. \quad (2.17)$$

Figure 2.7 displays the modified differential tunneling conductance $dI(V)/dV$ for different values of Γ . It can be clearly seen that Γ not only broadens the quasiparticle excitation peaks but also reduces their amplitude.

2.2.5 Tunneling of Cooper Pairs - The Josephson Effect

In the same year that Cohen *et al.* developed their theory on tunneling between a metal and a superconductor, Brian D. Josephson was theoretically investigating a tunnel junction that consists of *two* superconducting electrodes, which the indices k and l separated by a thin oxide layer as tunneling barrier. Josephson's fundamental idea was that despite the fact the

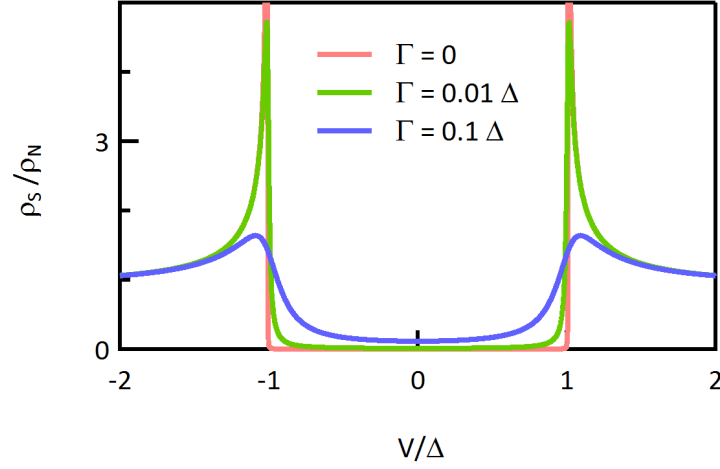


Figure 2.7 – Calculated differential tunneling conductance $dI(V)/dV$ normalized to the superconducting gap as a function of the lifetime parameter Γ using Eq. 2.17.

order parameter Δ rapidly drops to zero inside the tunnel barrier, the pair wavefunctions of both superconductors may still overlap. Moreover, he argued that two superconducting ground states, Δ_k and Δ_l , separated by a tunnel barrier, should also have independent phases $\Phi_k \neq \Phi_l$, corresponding to a different number of Cooper pairs in the electrodes. From these assumptions, Josephson concluded that the coherent superposition of these two ground states of different phases $\phi = \Phi_k - \Phi_l$ should enable the creation of a ground state pair in one electrode $S_k \dagger$ and the annihilation of such a pair in the other one S_l , whereas the total number of single particle states N remains unchanged, $S_k \dagger S_l |N, \phi\rangle = e^{i\phi} |N, \phi\rangle$.

Including these assumptions in the system's Hamiltonian, which is similar to Eq. 2.14, Josephson followed Cohen's perturbative approach in calculating the average rate of change in the quasiparticle density of one electrode $\langle \dot{N}_l \rangle$ and found the following expression for the total current through the junction:

$$I(t) = I_{QP} + \frac{1}{2} I_0 S_l(t) \dagger S_k(t) + \frac{1}{2} I_0^* S_k(t) \dagger S_l(t) \quad (2.18)$$

The first term, I_{QP} , represents the quasiparticle current, which is similar to Cohen's expression in Eq. 2.16. The last two terms represent a pair transfer current of amplitude I_0 , which oscillates at a frequency of $\frac{d\phi}{dt} = 2eV_J/h$, where V_J is the voltage drop across the tunnel contact. Although the theoretical description Josephson found was quite general, he was already able to interpret the physical significance of the pair current terms and predicted two phenomena, the Josephson effects [7]:

1. The AC Josephson effect: A ground state pair transfer at the voltage $2eV_J$ via the absorption or emission of a photon having the frequency $\nu = 2eV_J/h$.
2. The DC Josephson effect: A ground state pair transfer at zero voltage, $V_J = 0$, having the

Chapter 2. Fundamental Theory of Tunneling with Superconductors

maximum amplitude I_0 , which is called the *Josephson critical current*.

The physical interpretation of these two effects is that, first, in a Josephson junction a tunneling current of a maximum amplitude I_0 can be observed at zero voltage. Second, a tunneling current can be measured at voltage V_J if a photon of frequency $\nu = 2eV_J/h$ has been absorbed or emitted by the junction².

Josephson's derivations were quite revolutionary at this time since they were in contradiction to the established hypothesis that paired wavefunctions can not exist inside the tunnel barrier [2]. Even half a year after Josephson published his theory, theoretical studies appeared referring to this hypothesis [3]. Nevertheless, it was Josephson's mentor himself, P. W Anderson, who could – together with J. Rowell – experimentally demonstrate the existence of the DC Josephson effect [9], shortly before S. Shapiro also observed the AC Josephson effect [10]. One year after Josephson's initial work, V. Ambegaokar and A. Baratoff could not only theoretically validate his theory, but also significantly extend it [8, 44]. Following the same perturbative approach for calculating $\langle \dot{N}_I \rangle$, but representing the particle operators by their Green's functions, they derived the famous expression for the dependence of the pair current on the phase-relation between the two superconducting ground states:

$$I(\phi) = I_0 \sin(\phi). \quad (2.19)$$

Second, they also determined the coupling energy $E(\phi)$ of the two superconducting ground states as well as the temperature-dependent critical current $I_0(T)$ of the pair current, yielding:

$$E(\phi) = E_J \cos(\phi) = -\frac{\hbar}{2e} I_0 \cos(\phi), \quad (2.20)$$

$$I_0 = \frac{\Delta_1(T)}{R_N} K\left(\sqrt{1 - \Delta_1^2/\Delta_2^2}\right). \quad (2.21)$$

Here, E_J denotes the Josephson coupling energy of the junction that relates to the critical current as $E_J = (\hbar/2e)I_0$. Δ denotes the modulus of the superconducting order parameter, of which Δ_1 is the smaller one, R_N the resistance of the tunnel contact in the metallic state, and K Jacobi's complete elliptic integral of first kind. The physical interpretation of these two equations is that the overlap of the pair wavefunctions in the tunnel barrier results in a coupling potential E . With respect to the phase, E forms a so-called *washboard-potential*, in whose minima a particle – representing the junction – is in a bound state at constant ϕ , as displayed in Fig. 2.8(a). The height of the potential walls, E_J , is solely determined by Δ and R_N . The tunneling resistance of the Josephson junction $R_N \propto M_{k,l}$ directly reflects the pair wavefunction overlap via the matrix element $M_{k,l}$ (compare Eq. 2.12). Moreover, it should be noted that Eq. 2.21 for the critical current only holds for weakly coupled electrodes since the pair transfer was evaluated as a perturbation to the whole system. In this context, *weakly*

²Observing photon emission from Josephson junctions is not as straightforward as anticipated in early discourses, but this aspect will be addressed later.

coupled refers to a low transmission $G_N = 1/R_N$ of the junction with respect to the quantum of conductance G_0 , such that $G_N \ll G_0$.

The above presented, initial studies on the Josephson effect could already predict and prove its existence. However, they only marked the starting point for the investigation of pair transfer phenomena in tunnel junctions with two superconducting electrodes, called *Josephson junctions*. Other important aspects such as the temporal properties of this pair transfer were addressed afterwards and will be part of the next section.

2.3 Dynamics of the Junction Phase $\phi(t)$

The dynamics of the junction phase are of fundamental importance, since they determine the experimental characteristics of a Josephson junction. For this reason, right after the prediction and observation of the Josephson effect, subsequent theoretical investigations focused on the time-dependence of $\phi(t)$. It was Josephson himself who rewrote his first expression of the tunneling current (Eq. 2.18) such that it connects $\phi(t)$ directly with the current $I(t)$ through the junction [55]:

$$I(t) = I_0 \sin(\phi(t)) + \left[\frac{1}{R_{QP}} + \frac{1}{R_{QPP}} \cos(\phi(t)) \right] \frac{\hbar}{2e} \dot{\phi}(t) \quad (2.22)$$

Here, the first term denotes the current associated with the DC Josephson effect at zero voltage, the second term is the dissipative quasiparticle current at finite voltage and the last term is the so-called quasiparticle interference term. This term involves the creation (annihilation) of ground state pairs via tunneling of quasiparticles and, therefore, represents a different formulation for the phenomenon of Andreev reflections (cf. Sec. 2.2.3). Nevertheless, the temporal dynamics of $\phi(t)$ are dominated by the first two terms, whereas the quasiparticle-interference term is, for most of the tunneling resistance range, small if not zero or similar.

It should be noted that a theoretical treatment of the individual current amplitudes based on a Green's function approach was first given by Werthamer [56]. A very descriptive and general overview on these current contributions is given in Ref. [6], for instance.

The dynamics of $\phi(t)$ can be analyzed when considering the simplest case of a Josephson junction that is biased by a current source I_B . Figure 2.8(b) displays the circuit diagram of such a junction, which also includes the junction capacitance C_J , acting as a shunt. The current through this capacitance reads as $I_C(t) = \dot{Q} = C_J \times dV/dt$. Using the Josephson relation $V = (\hbar/2e)d\phi/dt$, $I_C(t)$ can be inserted into Eq. 2.22 in accordance to Kirchoff's law, which yields a differential equation for $\phi(t)$ [57, 58]:

$$I = I_0 \sin(\phi(t)) + \frac{1}{R_{QP}} \frac{\hbar}{2e} \dot{\phi}(t) + C_J \frac{\hbar}{2e} \ddot{\phi}(t). \quad (2.23)$$

To examine the dynamics of $\phi(t)$, it is a sufficient approximation to replace the dissipative

Chapter 2. Fundamental Theory of Tunneling with Superconductors

quasiparticle conductance $1/R_{QP}$ by an ohmic resistor R . Within this so-called *resistively and capacitively shunted junction model* (RCSJ) the differential equation for $\phi(t)$ can be rewritten to [59, 60]

$$\ddot{\phi}(t) + \frac{1}{\tilde{\tau}}\dot{\phi}(t) + \omega_0^2 \sin(\phi(t)) = \frac{\omega_0^2 I}{I_0}, \quad (2.24)$$

$$\tilde{\tau} = RC_J, \quad (2.25)$$

$$\omega_0 = \sqrt{\frac{2eI_0}{C_J\hbar}}, \quad (2.26)$$

This equation of $\phi(t)$ represents a non-linear, inhomogeneous differential equation of second order that cannot be solved analytically, yet it corresponds to the classical equation of motion for a driven rotating pendulum. In analogy, a pendulum with mass $m = C_J$ has the coordinate ϕ and experiences dissipation expressed in a quality factor $Q = \tilde{\tau}\omega_0$. Therefore, the dynamics of ϕ can be qualitatively well explained in this descriptive analogue.

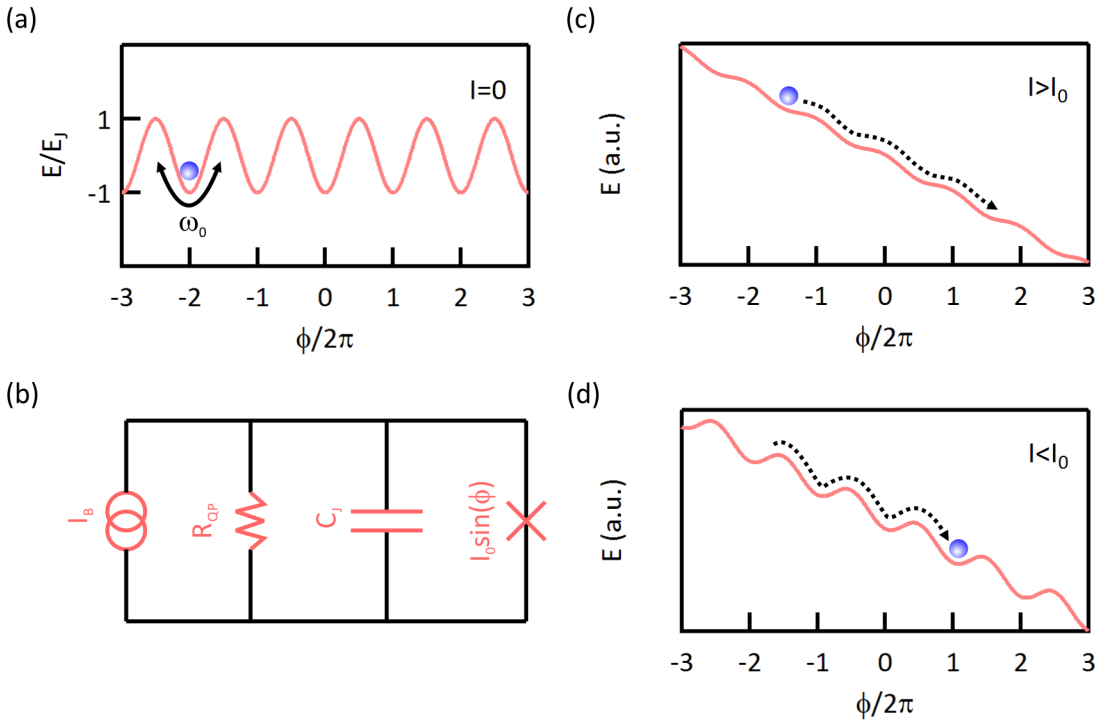


Figure 2.8 – (a) Coupling potential of a Josephson junction for the case of no external drive $I = 0$. The junction is represented by the blue particle. (b) Circuit diagram of a current-biased Josephson junction. I denotes the current source, R_{QP} the dissipative quasiparticle resistance, C_J the junction capacitance and $I_0 \sin(\phi)$ the Josephson junction. (c) Potential of the current biased Josephson junction $I > I_0$. (d) For underdamped junctions the particle continues its movement down the potential landscape when $I < I_0$.

To investigate the dynamics of the junction phase $\phi(t)$ let us first consider a Josephson junction, of which the external current drive is zero. In this case the time average of $\phi(t)$ is constant in time and the particle, representing the junction, oscillates around its zero point of motion inside the washboard potential minimum, as displayed in Fig. 2.8(a). For an increasing external current drive, $0 < I_B < I_0$ this situation remains stable. However, as soon as $I = I_0$ the potential has no minimum anymore and the particle will start rolling down the potential landscape with velocity $\dot{\phi}(t)$, which is displayed in Fig. 2.8(c). This situation corresponds to the case in which the junction switches out of its dissipationless zero voltage state to finite voltage $V = (\hbar/2e)\dot{\phi}$. In the classical analogue, the pendulum will oscillate around its zero point of motion with increasing amplitude, until the external drive is large enough that it swings over the pinnacle and starts rotating. Moreover, in this running state at $I_B > I_0$, the junction experiences dissipation as a result of the ohmic shunt R , which causes friction to the moving particle, thus slowing it down. When again lowering the drive I such that $I_B \leq I_0$, as shown in Fig. 2.8(c), the potential landscape remains tilted but has recovered its minima. Under this condition the dynamic reaction of the moving particle, i.e. the dynamics of the junction phase, crucially depends on the slope of the washboard, as given by the current drive and the amount of friction, i.e. energy dissipation, which is measured by the quality factor $Q = \omega_0\tilde{\tau}$.

For $Q \ll 1$ the energy dissipated per cycle through one potential minimum is much larger than the energy gained from the current drive and the junction is strongly *overdamped*. For this damping, the particle will immediately stop its motion as soon as the current drive equals the critical Josephson current, $I_B = I_0$. At this point the state of Fig. 2.8(a) is restored and the particle only oscillates around its zero point. Since the phase is now constant, $\dot{\phi}(t) = 0$, the Josephson junction is *retrapped* in its zero voltage state. In the pendulum analogue, the dissipation is such strong that as soon as the external drive reaches a critical value, the pendulum cannot reach the pinnacle of its orbit immediately, so falls back and starts oscillating around its zero point of motion. In the opposite case $Q \gg 1$, the energy dissipated per cycle is negligible compared to the gain of kinetic energy from the current drive and the junction is heavily *underdamped*. In this case, the rolling particle will stop its motion only if the washboard potential is not tilted anymore. Hence, the retrapping of the Josephson junction into the zero voltage state occurs at $I_B = 0$, corresponding to a pendulum that stops its rotating motion when the external drive stops.

In experiments, a likely case will be an intermediately damped junction, corresponding to $Q \geq 1$. In this case the energy dissipated per cycle is smaller than (equal to) the energy gain from the current drive. In this case, the particle will continue rolling down the tilted washboard potential, as shown in Fig. 2.8(c), until a minimum tilt is reached. At this particular tilt, the energy gain from the drive and the energy dissipation cancel out and the particle will stop its motion. Accordingly, at the corresponding current drive, $I_R < I_0$, the junction retraps and restores its zero voltage state of Fig. 2.8(a). This so-called *retrapping current* I_R can be found

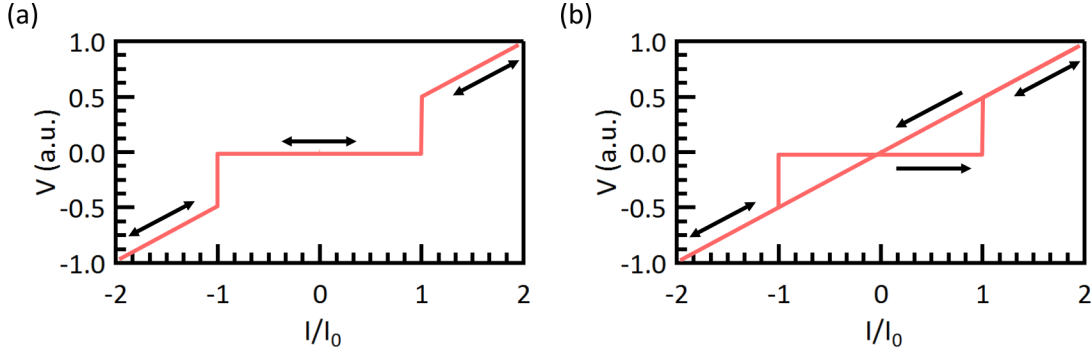


Figure 2.9 – (a) Non-hysteretic $V(I)$ characteristics of a heavily overdamped junction. (b) Hysteretic $V(I)$ characteristics of a strongly underdamped junction.

from the condition [59]:

$$\int_{-\pi}^{\pi} d\phi \frac{I_R}{I_0} = \frac{1}{\omega_0^2 \bar{\tau}} \int_{-\pi}^{\pi} d\phi \dot{\phi}(t). \quad (2.27)$$

The discussed dependence of the phase dynamics on the amount of dissipation Q can be directly observed in the experimental $V(I)$ characteristics of a current biased Josephson junction. In heavily overdamped junctions, the $V(I)$ curves are the same when sweeping the current drive from zero to a current larger than I_0 and back to $I = 0$, since switching and retrapping occurs at $I = I_0$ (see Fig. 2.9(a)). In contrast, heavily underdamped and intermediately damped junctions exhibit a hysteresis between forward and backward sweep of the current drive in the $V(I)$ characteristics. Figure 2.9(b) shows the extreme case of negligible damping, in which retrapping occurs at $I = 0$. For intermediate damping, the retrapping current will be in the range of $0 < I < I_0$, as determined from Eq. 2.27.

2.4 Thermal Fluctuations of the Junction Phase $\phi(t)$

In the previous sections, the Josephson effect was derived for an ideal Josephson junction, isolated from environmental perturbations. However, Josephson junctions in real experiments are embedded into a measurement circuit that, for instance, contains ohmic leads connecting the junction. Moreover, real experiments are thermalized at a finite temperature T , so that these ohmic leads will exhibit thermal resistor noise. This noise induces fluctuations in the junction phase $\phi(t)$ [31], as it will be presented in the following.

The physical consequences of these thermal fluctuations in $\phi(t)$ can be elucidated by considering the most simple case of a current-biased Josephson junction, as displayed in Fig. 2.8(b), with a current bias of $I < I_0$, at a temperature $T = 0$ K. Under these conditions the particle in the tilted washboard potential will oscillate around the metastable potential minima at a frequency ω_0 . If we now switch on the temperature to a finite value and suppose that the

2.4. Thermal Fluctuations of the Junction Phase $\phi(t)$

thermal energy $E = k_B T$ is comparable to the potential barrier height \tilde{U} , the particle has a chance to be thermally excited across the barrier, as displayed in Fig. 2.10. The probability of such an excitation process P_{TA} is proportional to the attempt frequency, which corresponds to the Josephson frequency ω_0 , and a Boltzmann factor, which relates the barrier height $\tilde{U} = E_J(\cos(\phi) - I/I_0)$ to the thermal energy $k_B T$:

$$P_{TA} \propto \omega_0 \exp\left(\frac{\tilde{U}}{k_B T}\right) = \sqrt{\frac{4e^2 E_J}{C_J \hbar^2}} \exp\left(\frac{E_J(\cos(\phi) - I/I_0)}{k_B T}\right). \quad (2.28)$$

It can be seen from this equation that for a junction of given coupling energy E_J and capacitance C_J the excitation probability increases with increasing current bias I and increasing temperature T . The dynamic response of ϕ on such an excitation process depends on the junction quality factor Q , as shown in Fig. 2.10. If the junction is heavily overdamped, $Q \ll 1$, the excited particle will, in the first place, relax to the adjacent potential minima and according to $\dot{\phi} = 0$, the junction remains in its zero voltage state. However, for an increasing tilt, $I \rightarrow I_0$, the friction of the particle will be not large enough to compensate for the tilt. Therefore, a thermal excitation of the particle over the barrier will result in a finite velocity $\dot{\phi}$ and the junction will switch to the finite voltage state. In the opposite case where the particle does not experience significant friction in the washboard, $Q \gg 1$, even one individual thermal excitation across the potential barrier is sufficient for the particle to gain a finite velocity $\dot{\phi} \neq 0$. For a given thermal excitation level the underdamped junction will, therefore, switch to the finite voltage state at much smaller bias currents as compared to overdamped junctions [61]. However, in both cases the premature switching out of the zero voltage state reduces the maximum DC Josephson current to values $I < I_0$ [31, 62].

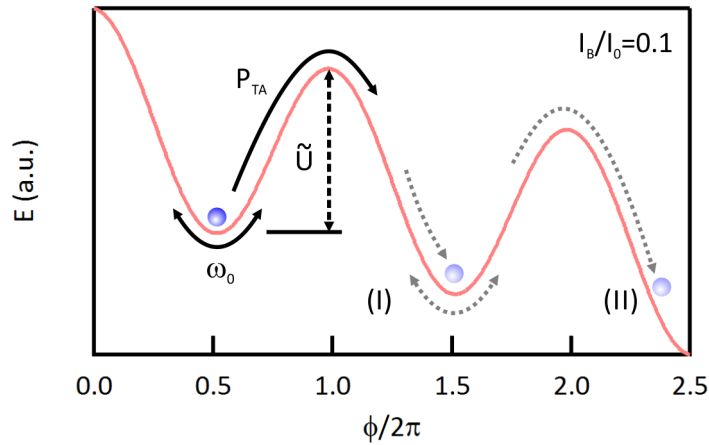


Figure 2.10 – Coupling potential $E(\phi)$ at a current bias of $I_B/I_0 = 0.1$. The particle, representing the junction, oscillates around a potential minimum at a frequency ω_0 and can be thermally excited across the potential barrier \tilde{U} . If the junction is overdamped $Q \ll 1$ the particle will relax into an adjacent minima (I). For an underdamped junction, the particle will start moving down the tilted washboard potential (II).

Chapter 2. Fundamental Theory of Tunneling with Superconductors

The formal context between thermal fluctuation and the Josephson effect was first derived by Ivanchenko and Zil'berman in the year of 1968 [31]. Assuming thermal white noise on an ohmic resistor R_{DC} , we can add a noise term $\delta I(t)$ to the source current, which modifies the differential equation for ϕ in the RCSJ model (see Eq. 2.24) to a stochastic differential equation, yielding

$$\ddot{\phi}(t) + \frac{1}{\tau} \dot{\phi}(t) + \omega_0^2 \sin(\phi(t)) = \frac{\omega_0^2}{I_0} (I + \delta I(t)). \quad (2.29)$$

It is apparent that thermal noise results in a stochastic, additional drive that eventually kicks the particle out of its zero point position in the potential minimum. For an overdamped junction where the junction capacitance C_J can be neglected, Eq. 2.29 transforms into the so-called Fokker-Planck equation, which describes the diffusive, i.e. thermally activated, motion of a particle that experiences a force. Therefore, thermally induced phase fluctuations are also called *phase diffusion* processes. The Fokker-Planck equation can be solved analytically yielding a modified expression for the DC Josephson current [31, 61]:

$$I(V_J) = I_0 \Im \left[\frac{I_{1-iV_J/\tilde{\beta}}(\tilde{\alpha})}{I_{iV_J/\tilde{\beta}}(\tilde{\alpha})} \right], \quad (2.30)$$

$$V_J = \frac{2e}{\hbar} \frac{d}{dt} \langle \phi \rangle = V - I(V) R_W, \quad (2.31)$$

$$\tilde{\alpha} = \frac{E_J}{k_B T}, \quad (2.32)$$

$$\tilde{\beta} = \frac{2e}{\hbar} R_{DC} k_B T. \quad (2.33)$$

Here, $I_\nu(\tilde{\alpha})$ denotes the modified Bessel function and R_W denotes the DC resistance of the measurement circuit. A major effect of thermal phase fluctuations on the characteristics of a Josephson junction is that the DC Josephson effect may be observed at finite voltages V_J across the tunnel contact as opposed to its observation at zero voltage for an unperturbed junction. This phenomenon directly results from thermally excited hopping from one metastable state at ϕ_1 to another state at ϕ_2 corresponding to an average, albeit small, phase velocity $\dot{\phi} \neq 0$. Employing the Josephson relation this finite phase velocity translates into a voltage drop across the tunnel contact³.

Figure 2.11 displays calculated $I(V_J)$ characteristics of such a voltage-biased Josephson junction for different α using Eq. 2.30. The maximum reachable DC Josephson current is smaller than the critical current and decreases with increasing temperature. Moreover, the peak shifts to larger voltages with increasing temperature, which is an intuitive observation, since the thermal hopping between adjacent potential minima should also be favored at higher temperatures.

³In accordance to the quantum fluctuation presented in the next section also the occurrence of thermal phase fluctuation does allow for the observation of the DC Josephson effect in voltage-biased experiments.

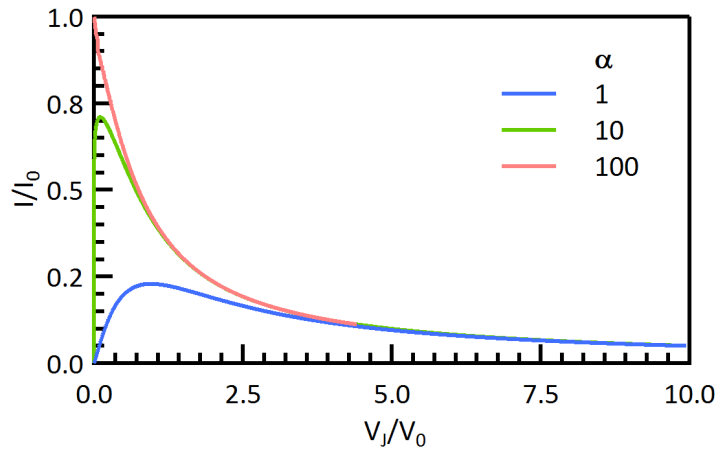


Figure 2.11 – Calculated DC Josephson currents normalized to I_0 for different α values with respect to the normalized voltage ($V_0 = I_0 R$) across the tunnel junction. The ohmic resistor was chosen to be $R = 1 \Omega$.

Although Eq. 2.30 was derived for an overdamped junction, the $I(V)$ characteristics of an underdamped junction are of similar contour. However, in this case the amplitude of the DC Josephson current is strongly reduced.

2.5 Quantum Mechanics of a Josephson junction

Within the past sections, the Josephson effect was derived from a many-body representation of a tunnel contact having two superconducting electrodes. It was also found that the dynamics of the phase can be described by a classical equation of motion that finds its analogue in a rotating pendulum. However, the phase ϕ and the charge q of a Josephson junction are quantum-mechanical quantities, for which reason these classical interpretations only apply to special cases, as will be discussed below. It can be shown, that both correspond to quantum-mechanical operators, $\hat{\phi}$ and \hat{q} , which obey the commutator relation [63]

$$[\hat{\phi}, \hat{q}] = i e. \quad (2.34)$$

The lack of commutativity between these two operators signifies that only the charge q or the phase ϕ of the junction can be well defined quantum numbers at the same time and, thus, can be measured with high precision. Hence, the charge and phase exhibit a standard deviation σ_q and σ_ϕ representing this uncertainty. This purely quantum-mechanical property has fundamental consequences on the measurement process, as will be discussed in the following.

To this end, we start out with a Hamiltonian for a simple Josephson junction of capacitance C_J

employing the operator representation for ϕ and q [31]

$$H = \frac{\hat{q}^2}{2C_J} - E_J \cos(\hat{\phi}). \quad (2.35)$$

Expressing the charge operator by the number operator \hat{n} , $\hat{q} = \hat{n}2e$, and identifying the Coulomb charging energy of the tunnel contact $E_C = 2e^2/C_J$, the Hamiltonian can be rewritten to

$$H = \frac{2e^2}{C_J} \hat{n}^2 - E_J \cos(\hat{\phi}) = E_C \hat{n}^2 - E_J \cos(\hat{\phi}). \quad (2.36)$$

If we assume an experiment for which E_J is much larger than E_C , the Coulomb term can be neglected and the junction phase ϕ is a good quantum number. In this situation the standard deviation of the phase vanishes, $\sigma_\phi = 0$, and the particle in a washboard potential model is an appropriate description (cf. Fig. 2.12). Under this condition, the DC Josephson current at $V=0$ is carried by coherent Cooper pair tunneling between the superconducting ground states. In the opposite case, $E_C \gg E_J$, the Josephson coupling term drops out, q is a good quantum number. We find $\sigma_q = 0$ and $\sigma_\phi = \infty$. In this situation, the phase is entirely delocalized along the washboard potential and the Josephson current is carried by the sequential tunneling of Cooper pairs at finite voltage V_J , which release the excess energy $V_J = h\nu/(2e)$ into the environment, i.e. via the emission of photons. At this point it should be noted that the actual *AC Josephson effect* also describes the tunneling of Cooper pairs at finite voltage $V_J = h\nu/(2e)$, however, for the case of *coherent* Cooper pair transfer.

In the intermediate situation in which the Coulomb energy is comparable to the Josephson energy, $E_C \approx E_J$, neither ϕ nor q are well defined and the standard deviation of both quantities is non-zero, as shown in Fig. 2.12. In this situation it is not appropriate anymore to represent the junction phase as a particle but rather by a quantum-mechanical wavefunction $\bar{\Psi}(\phi)$ that can extend across several minima in the washboard potential. In this situation, tunneling events through the barrier are possible and result in quantum fluctuations of the junction phase. These fluctuations have significant consequences. For instance, if the washboard potential is slightly tilted, these tunneling events yield a tiny but non-zero phase velocity $\langle \dot{\phi} \rangle$ that correspond to a finite voltage $\dot{\phi} = (2e/h)V$, although after tunneling the junction phase still remains in a bound state inside an adjacent potential minimum. As a result, the DC Josephson effect cannot be observed at zero voltage anymore [31]. Moreover, in the regime $E_C \approx E_J$, both the coherent tunneling of Cooper pairs around zero voltage can be observed as well as the sequential tunneling to higher voltages [40].

All of these three cases presented induce different experimental consequences:

- $E_J \gg E_C$: The coherent tunneling of Cooper pairs occurs at $V = 0$ and therefore, the DC Josephson effect can only be observed in a current-biased Josephson junction.
- $E_J \ll E_C$: Coherent tunneling of Cooper pairs does not occur, but only sequential Cooper

2.5. Quantum Mechanics of a Josephson junction

pair tunneling occurs at finite voltages $V_J = \hbar v / (2e)$ and therefore, the Josephson effect can only be observed in voltage-biased measurements.

- $E_J \approx E_C$: Both coherent and incoherent Cooper pair tunneling occurs, and the DC Josephson effect is found at very small voltages $V \neq 0$. Therefore, it is possible to observe the DC Josephson effect in current-biased measurements, as well as the sequential tunneling of Cooper pairs at $V_J = \hbar v / (2e)$ in voltage-biased measurements.

A more detailed theory on the quantum mechanics of a Josephson junctions as well as the possible experimental manifestations can be found in Ch. 6.

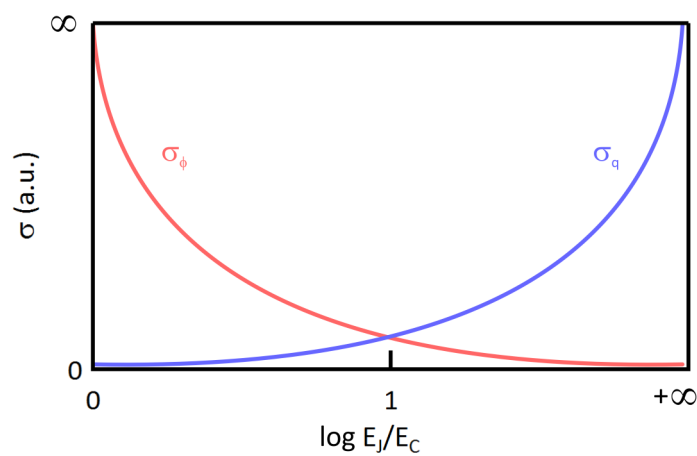


Figure 2.12 – Standard deviations of the phase operator σ_ϕ and the charge operator σ_q as a function of the ratio E_J/E_C .

3 Experimental

The scope of this chapter is to provide the reader with basics of Scanning Tunneling Microscopy (STM) and to discuss the experimental requirements for performing Josephson STM (JSTM) experiments. Moreover, this chapter will provide detailed descriptions on the experiment, preparation of the STM tip and the sample as well as experimental procedures.

3.1 Scanning Tunneling Microscopy

STM is an experimental technique that employs the quantum mechanical tunnel effect (cf. Sec. 2.2.1) to study the topographic and electronic properties of electrically conducting surfaces. Since its first realisation is 1982 by Binnig and Rohrer [64, 65], STM has evolved to be a major tool in physics and chemistry addressing questions, such as atomic scale magnetism and superconductivity, and the electronic properties of individual molecules and their self-assembly into molecular networks [66, 67, 16, 68, 69, 70, 71, 72]. Moreover, in the recent decade the experimental parameter space was further extended by the implementation of time-resolution and as in this work, ultra-low temperatures [32, 33, 34, 35, 36, 73].

The concept of an STM, as displayed in Fig. 3.2(a), involves a sharp electrically conducting tip that scans across an electrically conducting surface with a vertical separation of a few Å. During scanning a bias voltage V is applied between tip and sample and the resulting tunneling current is being recorded¹. In most cases, V corresponds to a generated potential difference between sample and ground and the measured tunneling current corresponds to the current, that flows between tip and ground as shown in Fig. 3.2(b).

The central element for topographically mapping a sample surface is the dependence of the tunneling current on the barrier width (cf. Ch. 2, Sec. 2.2.1). In the year of 1983 Tersoff and Hamann investigated this dependence for an STM geometry in which the tip is assumed to have a single atom at its apex [75]. Assuming only s -type orbital wavefunction for the STM

¹In the simplest case tip and sample are metals, but it is also possible to use ceramics, as the tunneling electrodes in the context of non-conventional superconductors, or semiconducting samples [65, 74].

tip², they found that the tunneling matrix element is modified by an additional dependence on the tip sample distance \vec{r} , $M_{k,l}(\vec{r})$ (cf. Eq. 2.12). The authors could further show, that $M_{k,l}(\vec{r})$ only depends on the amplitude of the sample wavefunction $\Psi_l(z)$ at the position of the tip \vec{r} . In the simplified one dimensional case, the relation between matrix element and vertical tip sample distance, z' , reads as

$$M_{k,l}(z') \propto \Psi_l(z'). \quad (3.1)$$

The resulting dependence of the tunneling current on z' can be subsequently found from the normalization condition for quantum mechanical wavefunctions. The condition

$$1 = \int_{-\infty}^{\infty} dz |\Psi_l(z)|^2 \quad (3.2)$$

implies an exponential decay of $\Psi_l(z)$ for $z \rightarrow \infty$ and, therefore, the tunneling current between tip and sample exponentially depends on their separation z' ,

$$I(z') \propto |M_{k,l}(z')|^2 \propto \exp(-2z'\kappa). \quad (3.3)$$

Here, κ denotes the decay constant of the sample's wavefunction $\Psi_l(z')$ for the decay into vacuum. Accordingly, if a tip is scanning a perfectly flat surface and reaches an obstacle as shown in Fig. 3.2(a), an individual atom on top of a surface for instance, the tunneling current will increase due to the shrinking tip-sample distance.

Scanning the surface topography of *real* samples is challenging when moving the tip across the surface at constant height, because it will exhibit obstacles such as atomic steps. Therefore, it is much more favorable to keep the measured tunneling current constant by adjusting the distance between tip and sample, which can be done by a so-called *feedback loop*. When the tip approaches an obstacle on the surface, the feedback loop detects an increase of the tunneling current due to the decreasing tip-sample distance. It will immediately lift up the tip in order to keep the current constant, as it is shown in Fig. 3.2(a)³. This operation mode, called constant current mode, facilitates the mapping of the surface topography at high precision and high velocity and, therefore, represents the standard mode of operation in STM experiments.

It should be mentioned that, in addition to the dependence of the tip sample separation, the tunneling current also strongly depends on the voltage-dependent *local* density of states (LDOS) of the sample $\rho_l(V)$ (cf. Eq. 2.16), which can vary for different spots on the sample. For this reason, a sample topography mapped with STM always includes information of the local electronic structure and deviates from the *real* sample topography. In return, the STM facilitates the investigation of $\rho_l(V)$ at the position of the tip, for which reason *Scanning Tunneling Spectroscopy* (STS) is the key spectroscopy technique on the atomic scale. ρ_l can be

²To first order, this is a good approximation, since the *s*-type orbital wavefunctions extend much further into space with respect to the center of the atom than *p*-, *d*- and *f*-type wavefunctions [76]

³The control of the tip-sample distance on the atomic scale as well as their lateral motion while scanning the surface requires piezo actuators, which have sub-picometer accuracy.

accessed applying the so-called lock-in technique. This technique adds a small periodic modulation $V(t) = V_m \cos(\omega_m t)$ on top of the applied bias voltage V and measures the resulting signal amplitude $A(\omega)$ at given frequency $f_m = \omega_m / (2\pi)$. This amplitude is proportional to the differential conductance, $A = dI/dV \times V_m$ and provides direct access to ρ_l [77].

This presented introduction on the topographic and local spectroscopic capabilities STM provides the necessary background which is needed in relation to this work, but the interested reader might refer to standard literature for more details on this technique as given in Refs. [78, 79].

In this work, for all STM experiments the Nanonis SPM controller was used providing all required properties for the operation of an STM experiment: A voltage bias source, an analog input for the current signal, high-voltage amplifier for the piezo operation, the feedback-loop for the control of the tip-sample distance and an internal lock-in amplifier.

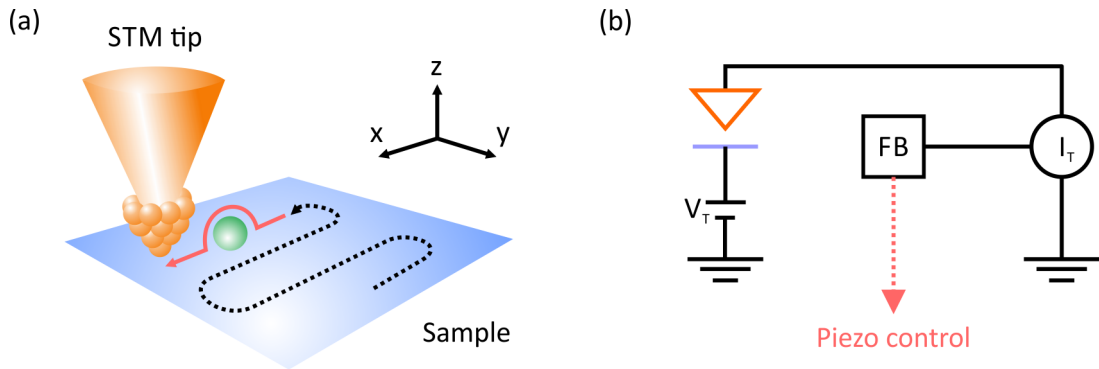


Figure 3.1 – (a) Schematics of an STM that scans a sample surface in the xy -direction in constant current mode. (b) Simplified circuit diagram for standard STM operation using a voltage bias.

3.2 Experimental Requirements for JSTM

Performing JSTM experiments is a challenging task to undertake due to the a variety of high-end experimental requirements that have to be met. These are a low vibration environment to enable the operation of an STM, ultra-low temperatures on the order of a few millikelvin necessary to achieve a sufficient ratio between Josephson coupling energy E_J and thermal energy $k_B T$, $E_J \geq k_B T$, and, last but not least, an overall shielding of the experiment against radio frequency (RF) radiation, necessary to minimize perturbations to the junction phase ϕ . Each of these experimental requirements will be addressed in the following subsections, but a detailed description of the experimental setup used in this work can be found in Refs. [80, 81, 35].

3.2.1 Mechanical Stability

As is was introduced in the previous section, the tunneling current between the STM tip and the sample exponentially depends on their distance, for which reason it is not only sensitive to the atomic scale topography of the sample, but also to mechanical disturbances imposed by the measurement environment. Such disturbances originate from vibrations of the laboratory building structure, from impact noise of scientists walking around or from a pumping environment necessary for operating a cryogenic instrument, for instance. These mechanical motions are transferred along the experimental setup into the tunnel junction of the STM experiment and can result in oscillations of the tip-sample distance, so that STM operation is impossible. Therefore, an STM setup demands both a sturdy construction of the experimental structure as well as an isolation of this structure from external mechanical noise sources.

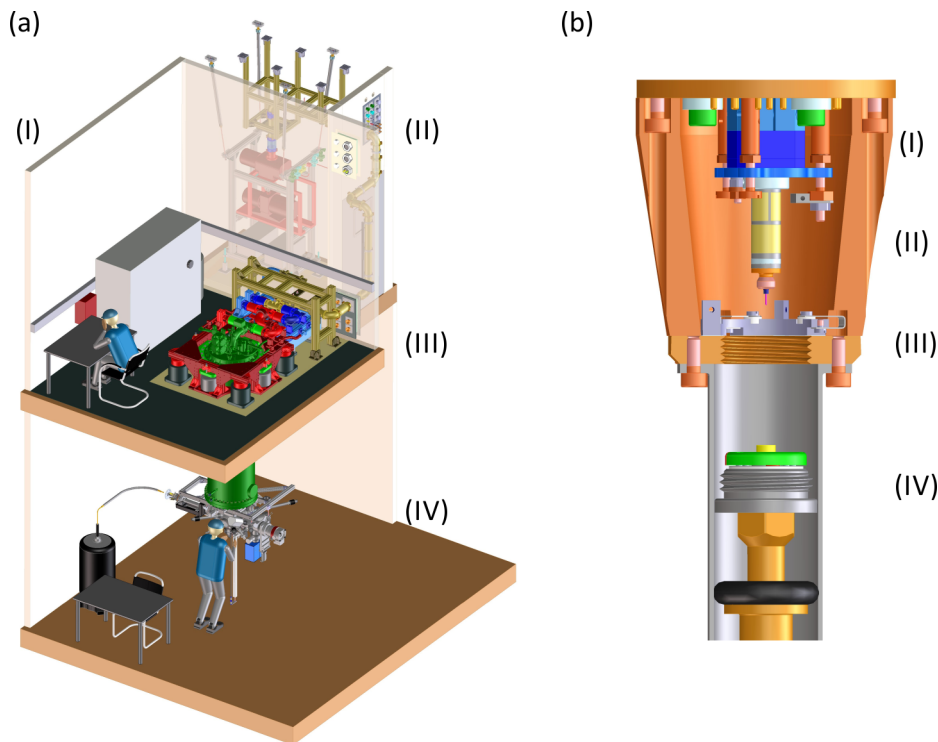


Figure 3.2 – (a) Laboratory hall and damping stages: (I) Two story high noise-canceling room (II) separate noise-canceling pumping room (III) Actively-damped stage (red) and passively-damped stage (green), on which the cryostat (green) is mounted. The pre-damping of the tubing is shown in blue color. (IV) Ultra-high vacuum (UHV) preparation chamber attached to the bottom of the cryostat. (b) Custom designed STM head [80]: (I) Coarse-motion [82] (II) Piezo-stack for xyz -control, containing the tip. (III) Sample-thread with bias voltage contact (IV) Transferable sample. Both figures are adapted from Ref. [35].

The STM used for this work combines both active and passive damping elements in order to minimize disturbances to the tip-sample distance [83, 84, 81]. Fig. 3.2(a) displays the two story

high laboratory hall of the millikelvin STM experiment. The cryostat containing the STM head sits on top of an active piezo-driven damping stage and a passive, air spring damping stage, which isolates the experimental setup from the lab floor. Moreover, operating a continuous flow dilution refrigerator system, as it will be discussed in the next subsection, requires circulator pumps and tubings, which serve as perfect mechanical noise sources and noise conductors. For this reason, these pumps are placed in an additional noise-encapsulating room and the tubings connecting the cryostat to the pumps are pre-damped on an active damping stage and contain flexible elements hindering vibration transfer.

The STM measurement head is custom made in a specialized design so as to minimize the response of the tip sample distance to mechanical vibrations [80]. Its cross section displayed in Fig. 3.2(b) presents all elements that are necessary for the STM operation: A coarse-motion to approach the sample from millimeter distance to less than a micrometer. A piezo-stack that facilitates xyz -motion with sub-picometer accuracy over a range of few hundreds of nanometers. Moreover, the custom design allows for the *in-situ* exchange of STM tip and sample, a property of utmost importance for this work as it will be demonstrated later.

In this configuration the stability of the STM experiment, defined by the standard deviation of the average tip-sample distance, $\sigma_{z'}$, was measured to $\sigma_{z'} = 4.2 \pm 0.5$ pm at a temperature of 15 mK [35].

3.2.2 Refrigeration to Millikelvin Temperatures

Experimentally investigating phenomena whose energy scale is much smaller than the thermal energy at room temperature, $k_B T \approx 26$ meV, requires the application of refrigeration techniques. Superconductivity in mercury, for instance, was first discovered by Kammerlingh-Onnes in 1911 when he succeeded in liquefying helium [85]. Attaching a reservoir of liquid helium to the experiment enables refrigeration down to temperatures of about $T = 4$ K which corresponds to a thermal energy of ≈ 0.1 meV⁴. For this reason liquid helium served as the preferred refrigeration medium over the last century. Studying the Josephson effect in tunnel junctions, however, requires even lower temperatures since the coupling energy of Josephson tunnel junctions in STM experiments is very small, $E_J/k_B \ll 1$ K⁵. Therefore, cooling with liquid Helium is not sufficient anymore and alternative refrigeration techniques have to be employed such as the *dilution refrigerator* [86, 87].

The dilution refrigerator (DR) exploits the latent heat of mixing the two helium isotopes ⁴He and ³He and allows for the refrigeration of experimental setups down to temperatures of a few millikelvin [88]. The operation procedure will be briefly described in the following, but a more comprehensive discourse can be found in standard literature, e.g Ref. [88]. When a mixture of ⁴He and ³He atoms is cooled below a temperature of $T = 0.867$ K, it will separate into two different phases that float on top of each other. The upper concentrated phase only

⁴Even temperatures of about $T = 1$ K can be reached experimentally when exploiting helium's latent heat.

⁵For junctions using elemental superconductors having an order parameter $\Delta \approx 1$ meV

consists of ^3He atoms, whereas the heavier diluted phase on the bottom mostly contains ^4He atoms plus a fraction of ^3He atoms⁶. This finite content of ^3He in the dilute phase displays an energetic minimum of the system at given temperature T and is of fundamental importance for the refrigeration process⁷: Removing ^3He atoms from the diluted phase forces other ^3He atoms in the concentrated phase to cross the phase boundary into the diluted phase. The transfer process increases the entropy of the system, thus requires energy. This energy is taken from the environment in the form of thermal energy and in this way the environment, e.g. an experimental setup, is being refrigerated [88].

The described mixing process can be operated in a continuous mode such, that ^3He atoms are extracted out of the diluted phase and recycled into the concentrated phase by means of circulator pumps, as schematically shown in Fig. 3.3(a)⁸. In this way, it is possible to generate sufficient cooling power for continuous refrigeration down to temperatures below 10 mK.

The cryostat used for this experiments from Janis Research Company has a cooling power of $\dot{Q} \approx 400 \mu\text{W}$ at a temperature of $T \leq 100 \text{ mK}$ [81, 35, 89]. This cooling power is relatively low compared to helium bath cryostats, for which reason the DR cryostat has to match specific requirements in order to reach millikelvin temperatures. Figure 3.2(b) displays a cross-section of the DR cryostat, which is constructed in analogy to onion skins: An outer liquid nitrogen dewar shields the liquid helium dewar on the inside from thermal radiation at room temperature. In the same fashion, this dewar shields the DR stage containing several temperature zones ranging from $\approx 1.5 \text{ K}$ down to the mixing chamber at $T = 15 \text{ mK}$, where the refrigeration process takes place. All temperature stages are used in order to liquefy and pre-cool the ^3He gas. It should be noted, that the pre-cooling process is of essential importance in order to reach temperatures below 50 mK, and this process bundles most of the required knowledge for building a state of the art DR stage. The STM (cf. Fig 3.2(b)), is attached to the mixing chamber via an thermally conductive scaffold manufactured from silver and thus reaches the same base temperature of 15 mK [35]. The employed DR system allows continuous refrigeration of the STM head to temperatures between 15 mK and 800 mK. However, all experiments in this work were performed either at 15 mK or 800 mK, respectively.

3.2.3 Electronic Temperature and Energy Resolution

Reaching very low experimental temperatures on the order of millikelvin is feasible because nowadays DR cryostats that reach temperatures as low as 10 mK are commercially available. However, the physically measured temperature at the mixing chamber in first approximation only represents the temperature of the crystal lattice. The temperature of the electrons moving

⁶Due to the larger mass, ^4He atoms have a smaller zero point motion as compared to ^3He atoms and, thus, the diluted phase is of higher density than the concentrated phase and floats at the bottom.

⁷This minimum displays the point of equivalent attractive and repulsive interaction potentials of ^3He atoms in the diluted phase. The interactions are of both thermodynamic and quantum-mechanical origin, which result from the fermionic nature of the ^3He isotopes.

⁸The still chamber is operated at a temperature of $T \approx 800 \text{ mK}$. At this temperature the gas pressure of ^3He is much larger compared to the gas pressure of ^4He . For this reason, only ^3He is cycled effectively.

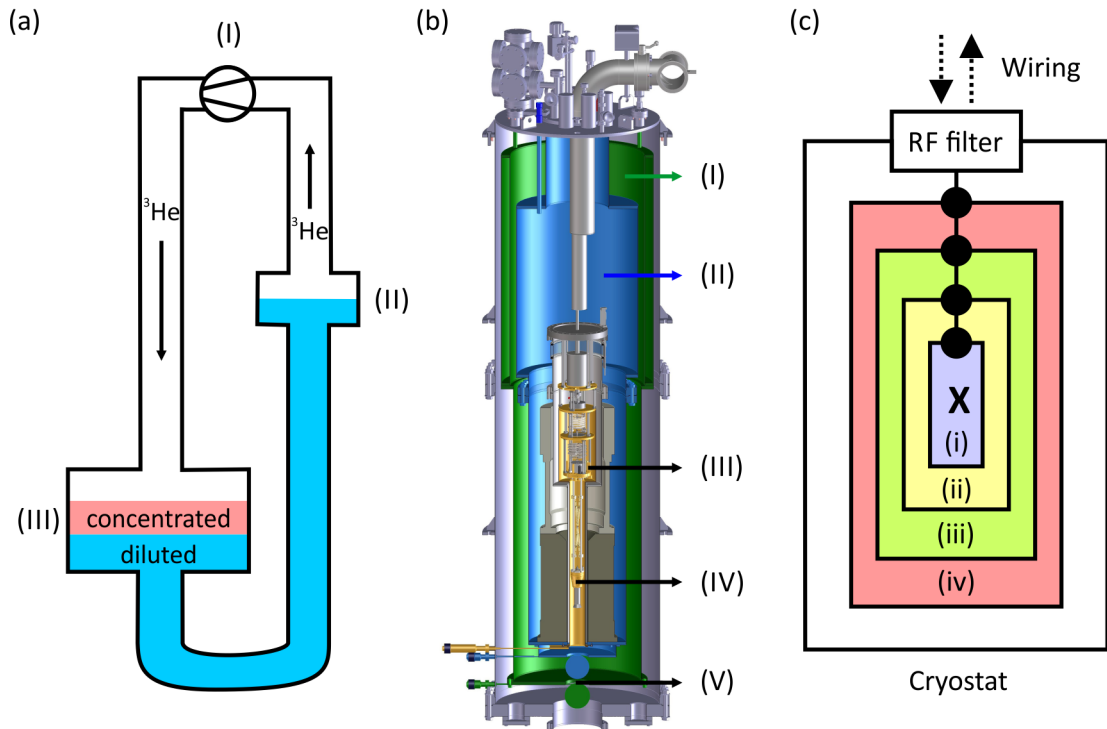


Figure 3.3 – (a) Schematics of the dilution refrigerator: A rotary pump (I) cycles ^3He atoms from the diluted phase in the so-called *still*-chamber (II) to the concentrated phase in the mixing chamber (III). (b) Cross-section of the Janis DR cryostat: (I) liquid nitrogen dewar (II) liquid Helium dewar (III) DR stage (IV) STM head attached to the mixing chamber (V) Shutter feedthroughs to the ultra-high vacuum (UHV) preparation chamber. (c) RF filtering concept: All wires into (out of) the cryostat are RF filtered at the UHV feedthrough. Secondly, the wires are thoroughly thermalized (black knots) at the several temperature stages of the DR, at (iv) 1.5 K, (iii) 800 mK, (ii) 100 mK and (i) 15 mK. The black cross marks the position of the STM head.

through the lattice might deviate since the electron-phonon coupling, which mediates the cooling energy transfer, is very weak in this temperature range. Moreover, at $T = 15\text{ mK}$ thermal energy is so small, $15\text{ mK} \approx 1.3\ \mu\text{eV}/k_B \approx 300\text{ MHz}/(k_B\hbar)$ that any thermal radiation from the environment as well as RF noise from the atmosphere represent a serious energy load that can heat up the electronic bath substantially. Hence, without further experimental means the electron bath in the junction leads remains 'hot' on the order of hundreds of millikelvin such that it will be impossible to observe phenomena whose energy scales are smaller, even when using a DR cryostat. Therefore, it is necessary to achieve a thorough thermalization of the wiring, a proper shielding from thermal radiation and filtering from RF noise to also obtain the lowest electronic temperatures.

In the experiment used for this study, thermalization of all wires is achieved by thermally anchoring every single wire at every temperature stage of the DR, as shown in Fig. 3.3(c). Moreover, at each of these thermalization points the wires are wrapped around bobbins in

order to increase the heat energy transfer effectiveness so that the small electron-phonon coupling can be overcome. Thermal radiation is reduced by shielding the mixing chamber as well as the STM head from temperatures larger than $T = 100$ mK or $T = 800$ mK, respectively. Furthermore, the STM head itself is a closed metal body of large mass thermalized at $T = 15$ mK, which provides additional shielding of sample and tip to heat radiation of 800 mK (cf. Fig. 3.2(b)). All wires leading to the STM head are continuously thermalized as well as protected by radiation shields manufactured out of silver [81]. Shielding from RF radiation is achieved by three different components (cf. Fig. 3.3(c)): First of all, the cryostat itself is a fully closed metal body acting as a perfect Faraday cage that cancels out any electromagnetic radiation. The only openings are the wire feedthroughs, for which reason all of them, signal- and control-lines, are low-pass filtered for RF radiation above 10 kHz [81, 35]. Moreover, the wires in the cryostat themselves, reaching down to the mixing chamber stage, are distributed RF filters having an attenuation of -120 dB/m for frequencies above 100 MHz [90, 81].

Another aspect of relevance for STM experiments at millikelvin temperatures that has not been addressed so far is the limitation of the electronic resolution due to thermal voltage noise \bar{u} on the STM junction capacitance C_J . This voltage noise results from thermal charge fluctuations \bar{Q} , $\bar{Q} = C_J \times \bar{u}$, and depends on the temperature as [91, 92]

$$\bar{u} = \sqrt{\frac{k_B T}{C_J}}. \quad (3.4)$$

The capacitance value of an STM tunnel contact can be easily estimated by electrostatic means when applying a simple 3D cone model for the STM tip in front of a planar surface, which mimics the sample. For the $250 \mu\text{m}$ thick wire used in this study such a calculation yields a capacitance of $C_J \approx 5$ fF. According to Eq. 3.4, we can calculate the thermal voltage noise on the STM junction capacitance at 15 mK to $\bar{u} = 6.4 \mu\text{eV}$. This finding signifies that even in the unlikely case that the electrons in the junction leads reach the exact lattice temperature, the small capacitance of the STM junction limits the energy resolution of STM experiments to $\Delta E \geq 6.4 \mu\text{eV}$ ⁹. For the sake of clarity, the term *energy resolution* denotes the minimum energetic difference ΔE between two energy levels that can still be resolved by means of spectroscopy, e.g. STS (cf. Sec. 3.1). It should be noted, that the calculated value only represents an estimate for standard STM conditions. Constructing STM junctions of larger capacitance will significantly decrease the thermal voltage noise amplitude, which is of interest in the context of the AC Josephson spectrometer at the atomic scale (cf. Ch. 5).

The energy resolution of the STM used for this work was investigated via thermal excitations of quasiparticles in superconducting aluminium tips. It was determined to $\Delta E = 11.4 \pm 0.3 \mu\text{eV}$ [35]. This value contains both the capacitive noise as well as the electronic temperature but, due to a lack of precise knowledge of C_J , the effective electronic temperature itself remains unknown.

⁹The voltage noise on external capacitances, such as capacitances used for filtering, is smaller in our case, $\bar{u}' \leq 1 \mu\text{eV}$

3.3 Sample and Tip Preparation

Investigating sample properties with an STM, such as the surface topography of a metal or individual atoms and molecules, also requires the capability to prepare these atomic scale sample systems. Moreover, both the preparation as well as the STM experiment have to be performed in an environment that avoids any contamination of the surface with other adsorbates, such as molecules from the surrounding atmosphere. Therefore, the preparation chamber of the system as well as the cryostat used for this work, as shown in Fig. 3.2(a), are operated at UHV conditions at a base pressure of $p \leq 5 \times 10^{-10}$ mbar. After the sample has been prepared, our experimental setup enables a sample transfer into the STM head (cf. Fig. 3.2(b)) without breaking the UHV.

Experiments involving the Josephson effect require two electrodes, whose superconducting properties are well described in the framework of BCS theory (cf. Sec. 2.1). All experiments in this work were performed using vanadium as the tip and the sample material. Vanadium is an elemental type-II BCS superconductor with a critical temperature of $T = 5.4$ K [93]. Details of the preparation procedures will be part of the following subsections.

3.3.1 Preparation of Vanadium (001) Single Crystal

For the experimental study of this work we use a vanadium(001) single crystal of purity 6N, which was purchased from SPL [94]. Atomically flat as well as impurity free surfaces can be obtained by means of ion sputtering and thermal annealing. To this end, the sample surface is sputtered with argon ions, which have a kinetic energy of $E = 1$ keV, at an argon pressure of $p = 1.6 \times 10^{-6}$ mbar and for a maximum time of 1 hour. Subsequently, the sample is annealed to a temperature of $T \leq 900$ °C. These two steps, sputtering and annealing, are continuously cycled as soon as the chamber pressure during the annealing step reaches values smaller than 2×10^{-9} mbar. For more details on these standard surface preparation procedures, the author encourages the reader to refer to standard literature, e.g. Ref. [95]. Figure 3.4(a) displays the freshly prepared vanadium surface on a macroscopic scale. It features large atomic layer terraces and moreover, the topography itself features a strip-like structure. The dark spots are surface defects which might originate from an empty vanadium lattice site in the top layer. Figure 3.4(b) displays the close-up on the atomic scale, in which the single vanadium atoms as well as a periodic superstructure of the atoms is apparent. The superstructure corresponds to the oxygen-assisted (5×1) surface reconstruction of the vanadium (001) surfaces, as reported previously [96, 97]. Such a clean sample surface allows us to create a high-quality Josephson junction between the STM tip and sample with a vacuum tunnel barrier whose width can be precisely tuned by the tip-sample distance. In particular, the clean surface and the point like tunnel junction of the STM excludes possible disorders, a non-uniform tunnel barrier thickness or electric shorts through the tunnel barrier for instance, as they can occur in planar junction geometries.

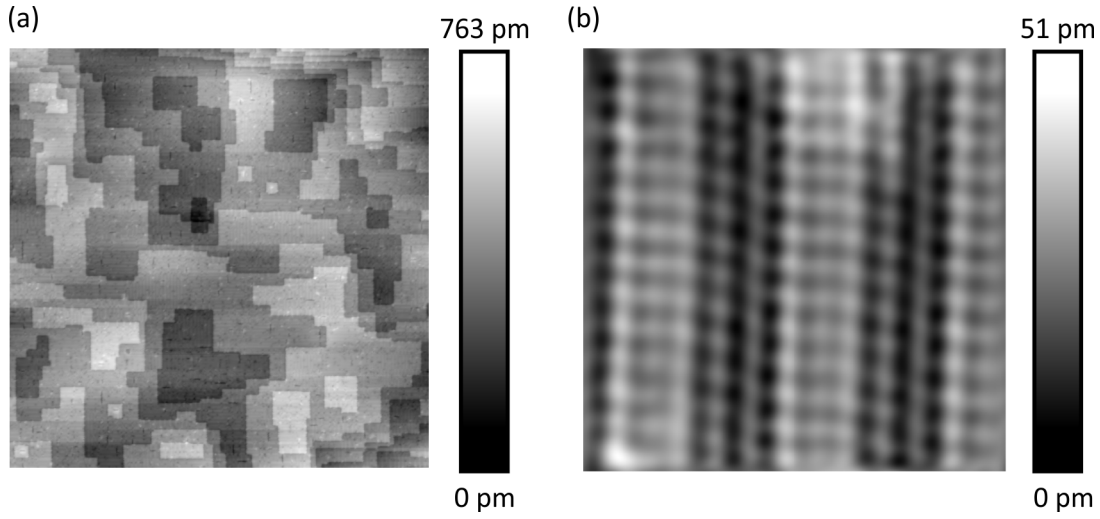


Figure 3.4 – (a) Large scale $100 \times 100 \text{ nm}^2$ topography of the vanadium (001) surface measured at $V = 1 \text{ V}$ and $I = 50 \text{ pA}$. (b) Atomic scale surface reconstruction of the same vanadium sample ($4 \times 4 \text{ nm}^2$) measured at $V = 2 \text{ mV}$ and $I = 5 \text{ nA}$

3.3.2 Preparation of Vanadium Tips

The STM tip is manufactured from a $250 \mu\text{m}$ thick, polycrystalline vanadium wire of 3N purity that was purchased from Alfa-Aesar. The tip is prepared by cutting the vanadium wire under tension. After the tip is mounted into the tip holder it is immediately transferred into the UHV environment and the STM head. To remove the native oxide, we perform field emission between the vanadium tip and the vanadium sample for $t \leq 20 \text{ min}$ at a field emission current of $I_{FE} \approx 20 \mu\text{A}$ when a voltage $V_{FE} \approx 50 \text{ V}$ is applied. Moreover, we apply voltage pulses of amplitude $-8 \leq V \leq 8 \text{ V}$ between the tip and the sample until both of them exhibit a well-developed BCS gap, as displayed in Fig. 3.5.

3.4 Measurement Circuit

Josephson junctions of which the capacitive charging energy E_C is comparable to the Josephson coupling energy E_J , can be investigated by means of both voltage-biased and current-biased experiments, as discussed in Sec. 2.5. In voltage-biased measurements, a voltage bias V_B is applied and the resulting tunneling current $I(V)$ is measured. The circuit diagram of such measurements is shown in Fig. 3.6(a), where the voltage source is the Nanonis SPM controller. The current is measured with a trans-impedance amplifier [98], which converts the current signals into voltage signals. These voltage signals are recorded by the Nanonis SPM controller analog input. The available minimum voltage step of $\Delta V \geq 150 \mu\text{V}$ results from the limited bit resolution of the analog-to-digital converter of the Nanonis voltage source, so that an additional voltage divider 1/1000 is used. In this work, all voltage-biased experiments on Josephson junctions are performed at a bias voltage step width of $\Delta V = 1 \mu\text{V}$ across a range of

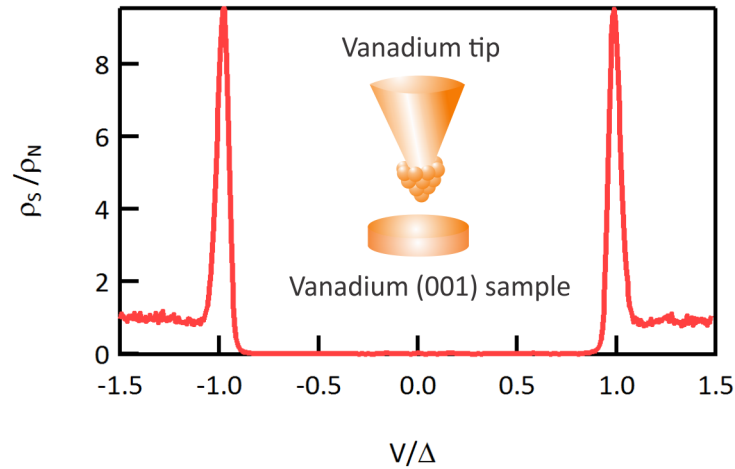


Figure 3.5 – dI/dV spectrum of a vanadium-vacuum-vanadium junction measured at $T = 800$ mK normalized to ρ_N ($V = 2$ mV, $I = 500$ pA, $f_m = 720$ Hz, $V_m = 20$ μ V).

typically -500 μ V $\leq V \leq 500$ μ V, unless stated otherwise.

To gain knowledge on the superconducting order parameter Δ of the tip and the sample, we also investigate the quasiparticle excitation spectrum of the tunnel junction. To this end, we record dI/dV spectra using the internal lock-in amplifier of the Nanonis controller. All of these measurements are performed at a voltage bias step width of $\Delta V = 8$ μ V across a range of -2 mV $\leq V \leq 2$ mV and using the lock-in parameter $f_m = 720$ Hz and $V_m = 20$ μ V.

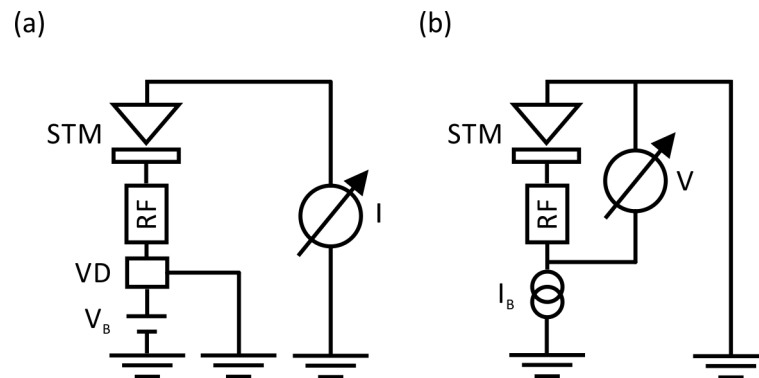


Figure 3.6 – (a) Voltage bias setup: The applied voltage, V_B , corresponds to a generated potential difference between sample and ground. A voltage divider, VD, refines the bias step width and the bias signal is RF filtered (RF). The tunneling current I is measured using a trans-impedance amplifier. (b) Current bias setup: The SMU generates a current bias I_B , which is RF-filtered before it is fed into the cryostat. The voltage drop between current source and ground, V , is also measured using the SMU.

In current-biased experiments a current I_B is forced through the tunnel junction and a voltage drop, $V(I_B)$ is being measured. Since the Nanonis SPM controller does not feature a bias

Chapter 3. Experimental

Table 3.1 – Circuit resistance of voltage biased measurements for different amplification ranges of the current amplifier

Current range	≤ 10 nA	≤ 100 nA	≤ 1 μ A
$R_{DC,1}$ (k Ω)	14	4.8	3.9

current output, an external source measure unit (SMU) is employed for both biasing the current and measuring the voltage drop across the tunnel junction in a two port measurement. To this end, the usual circuit to the Nanonis is replaced by a circuit containing the SMU, as shown in Fig. 3.6(b). Under these conditions, the feedback-loop is no longer applicable, but the tip-sample distance can still be controlled manually with the z -piezo voltage. Hence, the conductance G_N of the tunnel contact can still be adjusted to the desired value by, $G_N(z') = I_B/V \propto \exp(z'/\kappa)/V$. The SMU used for this study [99] features a minimum current step width of $\Delta I = 10$ fA and resolves voltages of $\Delta V \geq 100$ nV. If not stated otherwise, all measurement were performed on a bias current range of logarithmic point density, so that around $I = 0$ A, the minimum current step width corresponds to the source limit of 10 fA.

Whether the voltage is applied as a bias V_B or measured as a signal V , in both cases it does not correspond to the voltage drop across the tunnel junction V_J , but to the voltage drop across the entire measurement circuit. In most cases such a circuit contains several resistive elements R_{DC} , e.g. wires, filters or the voltage divider. The voltage drop across the tunnel junction V_J is obtained by subtracting these voltage drops from the source voltage or the measured voltage, respectively, which reads as

$$V_J = V_{(B)} - I(V_{(B)}) \times R_{DC,i}. \quad (3.5)$$

From measurements we find a circuit resistance of $R_{DC,2} = 3750 \Omega$ for the current-biased measurements. The circuit resistance of the voltage-biased measurements, $R_{DC,1}$, depends on the gain of the current amplifier as summarized in Tab. 3.1.

3.5 Experimental Procedure

The past sections presented the experimental requirements for performing JSTM experiments at ultra low temperatures. The scope of this section is to briefly summarize the experimental procedure from the sample preparation to the actual measurement.

The first step of our experiment is the transfer of the STM tip and the sample into the cryostat after they have been prepared as described in Sec. 3.3. Since the tip and the sample are thermalized at temperatures between 77 and 273 K, their transfer into the cryostat introduces a serious heat load that will warm up the cryostat to temperatures of around 77 K. After the cryostat is refrigerated again to a temperature of about 800 mK – which usually takes approximately one night – we approach the tip to the sample using the coarse motor. As soon as the tip is in contact with the sample, we remove the native vanadium oxide from

the tip apex by performing field emission (cf. Sec. 3.3). The field emission process leaves a lot of debris on the entire accessible surface of $1 \times 1 \mu\text{m}^2$ area¹⁰, for which reason after field emission we retract the tip and rotate the sample, so that the tip will approach a different and clean sample spot. After refrigeration to 800 mK we again approach the sample. As soon as the contact is reached, we apply voltage pulses until both the tip and the sample exhibit the well developed superconducting BCS gap, as shown in Fig.3.4. At this point, we start with the refrigeration process by increasing the amount of ^3He - ^4He -mixture in the DR cryostat. It takes typically about one night until the mixing chamber and the STM head are thermalized at the base temperature of 15 mK. As soon as we have found an atomically clean surface, e.g. shown in Fig. 3.4, we start with the current- and voltage-biased experiment as explained in Sec. 3.4. From these experiments we obtain the experimental data, which we will discuss in the next three chapters.

¹⁰The edge length of this square is limited by the maximum piezo displacement.

4 The Critical Josephson Current in the Dynamical Coulomb Blockade Regime

The content of this chapter is partly taken from the manuscript entitled “*Critical Josephson Current in the Dynamical Coulomb Blockade Regime*” by the authors Jäck, B., Eltschka, M., Assig, M., Etzkorn, M., Ast, C.R. and Klaus Kern, which we recently submitted for publication.

4.1 Introduction

The critical Josephson current I_0 is a universal parameter that characterizes the coupling configuration between two superconducting ground states in the tunnel junction electrodes. In the tunnel regime, i.e. the normal state conductance G_N of the tunnel contact is much smaller than the quantum of conductance G_0 , the critical Josephson current directly depends on G_N and the superconducting order parameters Δ_1 and Δ_2 , as it was derived by Ambegaokar and Baratoff (cf. Eq. 2.21)[8]. Thus, the Josephson critical current provides direct access to the superconductor ground state and for this reason, it serves as an ideal probe for superconductor physics, such as the pairing symmetry of unconventional superconductors [100]. The desirable combination of the Josephson effect with Scanning Tunneling Microscopy (STM), also referred to as JSTM, transfers this capability to the atomic scale [14]. Additionally, this combination enables the investigations of local variations of the superconducting order parameter as a probe for a variety of phenomena. These are, for instance, the response of the superconducting ground state to the local dopant structure in unconventional superconductors [101] or the interaction of the superconducting ground state with a single magnetic impurity [16]. In particular the competition between superconductivity, which favors pairing of electrons with opposite spin directions, and magnetism, which favors pairing of electrons with same spin direction, on the local scale has attracted theoretical [102, 18, 17] as well as experimental [16, 20] efforts for decades, also in the context of unconventional superconductors [103].

So far, experiments exploiting the JSTM concept [26, 27, 28, 29, 30] have measured at comparably high temperatures, where the thermal energy exceeds the Josephson coupling energy, so that the critical current cannot be accessed unambiguously [31, 104]. Directly accessing the critical current in an experiment requires special design and tuning of the properties of

Chapter 4. The Critical Josephson Current in the Dynamical Coulomb Blockade Regime

the Josephson junction beforehand or it demands detailed knowledge about the junction parameters as well as tuning of the involved energy scales for precise modeling. While the former approach has been successfully applied in planar tunnel junctions [39, 61, 62], other experiments, such as STM, have much less design flexibility. In these cases, the latter approach is more appropriate, but not every regime in which a Josephson junction is operated can be modeled equally well for extracting the critical current. For instance, the Ivanchenko-Zil'berman model, discussed in Sec. 2.4, is only valid for systems of large capacitance and a frequency-independent circuit impedance $Z(\nu) = Z(0)$. This clearly does not apply to STM experiments that involve a small tunnel junction capacity and a junction environment that contains transmission lines with strong frequency dependence $Z(\nu)$ [31].

Choosing the appropriate theoretical model in fact requires a careful consideration of all involved phenomena that effect the properties of the Josephson junction. These are the Josephson coupling energy $E_J = \hbar I_0 / (2e)$, the Coulomb charging energy of the tunnel contact $E_C = 2e^2 / C_J$, where C_J is the junction capacitance, as well as the thermal energy $E_T = k_B T$, where T is the temperature. Fig. 4.1 compares these energy scales as a function of the normalized tunneling conductance G_N / G_0 for our STM experiment. We find that in the tunneling regime, $G_N \ll G_0$, the energy scales order in the following way: $E_T \leq E_J \ll E_C$. This reduces thermal fluctuations of the junction phase as introduced in Sec. 2.4 and, in particular, this means that the condition $E_T \leq E_J$ for JSTM to work best is fulfilled for most of the tunneling conductance range [31, 14].

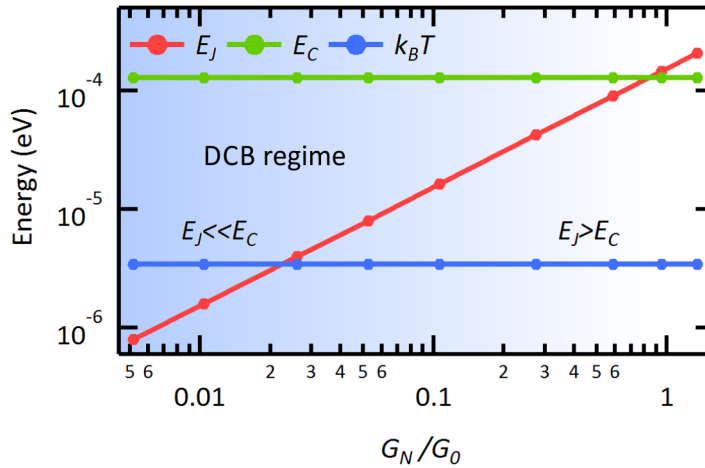


Figure 4.1 – Comparison of all relevant energy scales as a function of the normalized tunneling conductance for a Josephson junction in an STM: E_J denotes the Josephson coupling energy, E_C the capacitive charging energy and $k_B T$ the thermal energy.

In addition, we find $E_J \ll E_C$ and can conclude that the tunneling current in our STM experiment is carried by the sequential tunneling of Cooper pairs. In this regime, $E_J \ll E_C$, also referred to as the dynamical Coulomb blockade (DCB) regime, the DC Josephson effect can not be observed at $V = 0$ anymore (cf. Sec. 2.5) [31, 37, 38]. Instead, Cooper pairs tunnel at finite

voltages $\Delta V \neq 0$, which results in a so-called *supercurrent peak*, as shown in Fig.4.2 [62]. Since Cooper pairs consist of two electrons of opposite momentum and opposite spin orientation, they carry no kinetic energy as well as no net spin. Accordingly, the Cooper pair tunneling at finite voltages represents an inelastic process, in which the energy quanta $h\nu$, proportional to the junction bias voltage $V_J = h\nu/(2e)$, are released into the environment via the emission of a photon of energy $E = h\nu$ (compare Fig. 4.3). The emitted photon spectrum has recently been studied in more detail [105], also in the context of non-linear quantum electrodynamics [106]. Moreover, a junction environment that exhibits spectral resonances, e.g. standing electromagnetic modes of energy $E = h\nu$, can interact with the Josephson junction and induce inelastic Cooper pair tunneling at an applied voltage bias $2eV_J = h\nu$ ¹ [107, 39]. Such a process manifests itself as additional spectral resonances in the measured $I(V_J)$ characteristics and these resonances are also present in our experiment, as displayed in Fig. 4.2.

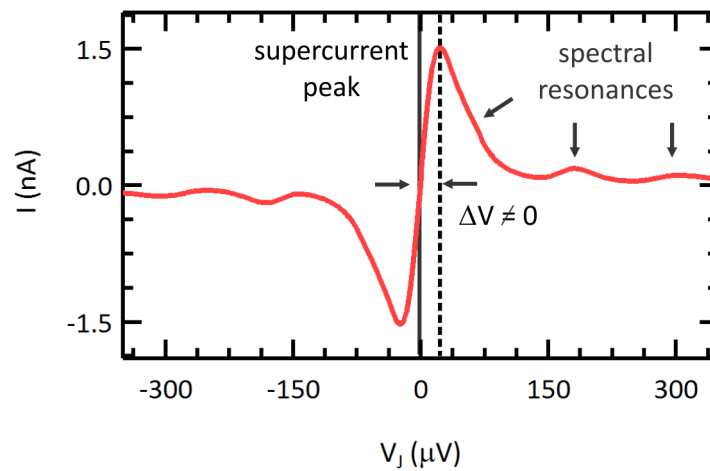


Figure 4.2 – Typical $I(V_J)$ tunneling characteristics measured at $G_N/G_0 = 0.27$ and $T = 15$ mK.

The inelastic Cooper pair tunneling characteristics of voltage-biased Josephson junctions can be analyzed in the framework of $P(E)$ -theory [37, 38]. This theory models the spectral energy exchange probability $P(E)$ between a tunneling Cooper pair and an – quite general – environment, from which the inelastic tunneling current $I(V_J)$ can directly be calculated. The following section will present the derivation of $P(E)$ -theory that is necessary to model the Cooper pair tunneling characteristics of a voltage-biased Josephson junction in an STM at millikelvin temperatures.

4.2 $P(E)$ -Theory

The theoretical basis for calculating the tunneling characteristics of microscopic tunnel junctions was developed along with the technological advances in manufacturing such microscopic devices on the sub-micrometer length scale in the 1980s. In analogy to the theory

¹The factor of two here considers the double electron charge of the Cooper pair.

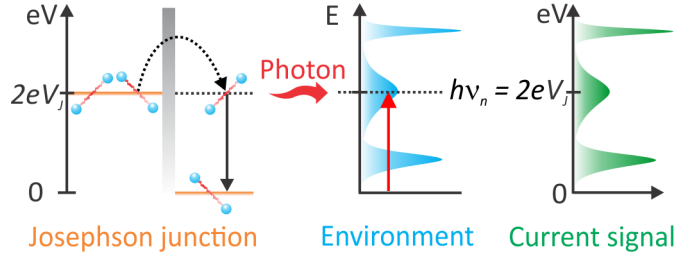


Figure 4.3 – Illustration of inelastic Cooper pair tunneling in the dynamical Coulomb blockade regime.

of the tunneling effect in macroscopic junctions (cf. Sec. 2.2), also the tunneling theory for microscopic junctions was derived without limitations to superconducting tunneling. In fact, the central element of this theory is the quantum nature of the junction phase ϕ and the charge q (cf. Sec. 2.5), which are of great relevance for microscopic devices in which quantum effects come to light. The second element is a formalism that describes the dissipative interaction of a quantum system with an arbitrary environment, which was first formulated by Caldeira and Leggett in 1983 [108]. They could show that a dissipative environment corresponds to a set of N harmonic oscillators represented by a set of N LC -circuits of capacitance C_n and inductance L_n . The Hamiltonian of this type of environment then reads as

$$H = \sum_{n=1}^N \left[\frac{q_n^2}{2C_n} + \left(\frac{\hbar}{e} \right)^2 \frac{1}{2L_n} \left(\frac{\phi}{2} - \frac{e}{\hbar} Vt - \phi_n \right)^2 \right], \quad (4.1)$$

whereas in the limit $N \rightarrow \infty$ the environment can be rewritten in terms of a frequency-dependent impedance

$$Z(2\pi\nu) = \left[\int_0^\infty dt \exp(-i\nu t) \sum_{n=1}^N \frac{\cos(\nu_n t)}{L_n} \right]^{-1}. \quad (4.2)$$

As we will see later, the formulation of the environment as a complex-valued impedance $Z(\nu)$ will be of great advantage in order to model experimental data. It should be noted, that the achievement of Caldeira and Leggett reaches far beyond the research area of Josephson physics discussed in this work, since energy dissipation from quantized energy levels into a continuous environment is found in any quantum mechanical system and, moreover, is still part of ongoing research.

In order to calculate the tunneling current of a microscopic Josephson junction, the junction Hamiltonian (cf. Sec. 2.5) has first to be extended by the environment [107, 109]

$$H = \frac{q^2}{2C_J} - E_J \cos(\phi(t)) + \sum_{n=1}^N \left[\frac{q_n^2}{2C_n} + \left(\frac{\hbar}{e} \right)^2 \frac{1}{2L_n} \left(\frac{\phi}{2} - \frac{e}{\hbar} Vt - \phi_n \right)^2 \right]. \quad (4.3)$$

As has been already introduced before, in the dynamical Coulomb blockade regime the

Coulomb charging energy of the junction E_C exceeds the Josephson coupling energy, E_J , which represents the Cooper pair transfer across the tunnel junction. Therefore, the tunneling rate of Cooper pairs can be evaluated by means of time-dependent perturbation theory, treating E_J as a perturbation to E_C ².

Applying Fermi's golden rule the voltage-dependent tunneling rate $\tilde{\Gamma}(V_J)$ can be evaluated to

$$\tilde{\Gamma}(V_J) = \frac{E_J^2}{4\hbar^2} \int_{-\infty}^{\infty} dt \exp(i\nu t) \langle \exp(i\phi(t)) \exp(i\phi(0)) \rangle. \quad (4.4)$$

The entire interaction between junction and environment, facilitating the inelastic tunneling process, is contained in the so-called phase-phase correlation function $J(t) = \langle \exp(i\phi(t)) \exp(i\phi(0)) \rangle$. This function represents the average change of the phase coherence via the interaction with the environment and accordingly the transfer of Cooper pairs (cf. Sec. 2.2.5). The correlation function can be analytically evaluated for an arbitrary environment and reads as [107, 109]

$$J(t) = 2 \int_{-\infty}^{\infty} \frac{d\nu}{\nu} \frac{\Re[Z_t(\nu)]}{R_Q} \frac{\exp(-i\nu t) - 1}{1 - \exp(-h\nu/(k_B T))}. \quad (4.5)$$

$J(t)$ is dominated by the frequency-dependent environmental impedance $Z_t(\nu)$ normalized to the resistance quantum of Cooper pairs $R_Q = h/(2e)^2$. Here, $Z_t(\nu)$ represents the *total* environmental impedance that contains both the environment and the junction capacitance C_J , which acts as a capacitive shunt:

$$Z_t(\nu) = \frac{1}{i2\pi\nu C_J + Z^{-1}(\nu)}. \quad (4.6)$$

Moreover, $J(t)$ explicitly contains the temperature of the environment, which causes fluctuations to the junction phase $\phi(t)$ (cf. Sec. 2.4). By separating the interaction with the environment and the Josephson coupling of the junction, it is now possible to rewrite the expression for the tunneling rate, Eq. 4.4, yielding

$$\tilde{\Gamma}(V_J) = \frac{\pi E_J^2}{2\hbar} P(2eV_J), \quad (4.7)$$

$$P(E) = \frac{1}{2\pi\hbar} \int_{-\infty}^{\infty} dt \exp\left[J(t) + \frac{i}{\hbar} Et\right]. \quad (4.8)$$

This $P(E)$ -function, serving as the theory's name giver, represents the spectral probability of a Cooper pair to exchange an energy portion $E = 2eV_J$ with the environment $Z_T(\nu)$ when a voltage bias $2eV_J$ is applied. Since the probability distribution for the energy exchange $P(E)$ is directly proportional to the tunneling rate, it follows that such an inelastic energy exchange between Cooper pair and environment directly results in a tunneling current signal. In other words, only in the case where the environment provides a possibility for the Cooper pair to release its excess energy $h\nu = 2eV_J$ (or the opposite case the environment provides the energy

²For a detailed description of the theoretical procedure the reader might refer to Refs. [107, 109]

Chapter 4. The Critical Josephson Current in the Dynamical Coulomb Blockade Regime

portion $2eV_J = h\nu$), Cooper pairs can tunnel and, correspondingly, a tunneling current can be measured at the applied voltage $2eV_J$.

It should be noted that the total energy exchange probability over the entire spectral range is unity, for which reason it requires normalization of the calculated $P(E)$ -function, reading

$$1 = \int_{-\infty}^{\infty} P(E) dE. \quad (4.9)$$

Finally, the total tunneling current through a microscopic Josephson junction can be calculated as the difference between the probabilities of releasing energy into the environment, $P(2eV_J)$, and of absorbing energy from the environment, $P(-2eV_J)$, respectively [37, 110, 111]:

$$I(V_J) = \frac{\pi e E_J^2}{\hbar} [P(2eV) - P(-2eV)]. \quad (4.10)$$

The above presented derivation of the $P(E)$ -theory reveals several essential properties of this approach from which an analysis of experimental data will greatly benefit:

- In order to calculate the energy exchange probability distribution $P(E)$ of a specific junction environment, it only requires a complex expression of the environmental impedance $Z(\nu)$ as the sole input parameter.
- All interaction of the junction with the environment is contained in the $P(E)$ distribution, which is independent of the tunneling conductance G_N . Hence, for all values of G_N the $P(E)$ distributions will be the same.
- The Josephson effect itself enters the theory only as a scaling factor E_J^2 of the previously calculated $P(E)$ distribution. Hence, the Josephson coupling energy $E_J = (\hbar/2e)I_0$ can be determined independently with high accuracy.

For the purpose of JSTM the Josephson critical current I_0 has to be determined from experimentally determined Cooper pair tunneling spectra $I(V_J)$. On the one hand, $E_J = (\hbar/2e)I_0$ is an independent scaling parameter favoring this goal. On the other hand, it still requires fitting of a calculated $P(E)$ distribution to the experimental data which is quite a difficult task to undertake. Only for very few cases of simple environmental impedance functions and in the zero temperature limit, can the $P(E)$ distribution be calculated analytically [37, 109]. However, this does not represent the most common case found in experiment, in which at least temperature will be non zero. For this reason the $P(E)$ -function for the interaction with the environmental impedance $Z_t(\nu)$ has to be calculated by means of numerical computation.

In addition, other phenomena, such as thermal voltage noise \bar{u} on the junction capacity, can serve as an energy source or drain for the inelastic tunneling of Cooper pair. In order to correctly model experimental Cooper pair tunneling characteristics it is necessary to include all

possible inelastic interactions with the environment. Therefore, the presented description of the $P(E)$ -theory requires further extensions, which will be part of the following subsections.

4.2.1 Numerical Computation of the $P_Z(E)$ Distribution for an Arbitrary Impedance $Z_t(\nu)$

The numerical calculation of the $P_Z(E)$ distribution that models the interaction of a Josephson junction with an arbitrary environmental impedance $Z_t(\nu)$ could, in principle, be achieved by first computing Eq. 4.5 and 4.8³. Still, the numerical calculation of these functions is difficult, for which reason Ingold and Grabert derived an integral equation [112]

$$P_Z(E) = I(E) + \int_{-E_0}^{E_0} d\nu K(E, \nu) P(E - h\nu), \quad (4.11)$$

which can be solved iteratively and enables the numerical calculation of the $P_Z(E)$ distribution [112].

$$I(E) = \frac{1}{\pi h} \frac{D}{D^2 + E^2/h^2}, \quad (4.12)$$

$$D = \frac{\pi k_B T \Re[Z_t(0)]}{h R_Q}. \quad (4.13)$$

The inhomogeneity of Lorentzian shape, $I(E)$, represents a probability distribution that determines the minimum width of $P_Z(E)$, as a result of thermal noise on an ohmic resistor $R_{DC} = \Re[Z_T(0)]$ in the junction environment. The integral kernel $K(E, 2\pi\nu)$ contains all the interactions with the frequency-dependent environment:

$$K(E, \nu) = \frac{E/h}{D^2 + (E/h)^2} k(\nu) + \frac{D}{D^2 + (E/h)^2} \tilde{\kappa}(\nu), \quad (4.14)$$

$$k(\nu) = \frac{1}{1 - \exp[h\nu/(k_B T)]} \frac{\Re[Z_t(\nu)]}{R_Q} - \frac{k_B T \Re[Z_t(0)]}{h\nu R_Q}, \quad (4.15)$$

$$\tilde{\kappa}(\nu) = \frac{1}{1 - \exp[h\nu/(k_B T)]} \frac{\Im[Z_t(\nu)]}{R_Q} - \frac{2k_B T}{h} \sum_{n=1}^{\infty} \frac{\omega_n}{\omega_n^2 + \nu_n^2} \frac{Z_t(-i\omega_n)}{R_Q}. \quad (4.16)$$

Here $\omega_n = 2\pi n k_B T$ denotes the Matsubara frequencies. This set of equation enables the self-consistent calculation of a $P_Z(E)$ distribution, where the inhomogeneity $I(E)$ serves as an initial test function $P_{m=0}(E)$. Employing the environmental impedance, as it will be introduced in Sec. 4.3, the integral equation, Eq. 4.11, can be solved iteratively until self-consistency is reached with a relative deviation of 1×10^{-6} . Typically this takes less than $m = 10$ steps using

³For the sake of clarity, the index z in $P_Z(E)$ marks the probability distribution for the interaction with the frequency-dependent environment, $Z_t(\nu)$.

50000 node points on an interval $\pm 5 \text{ mV}$ ⁴. With this extension of the $P(E)$ -theory it is possible to numerically calculate the spectral inelastic energy exchange probability $P_Z(E)$ between a Josephson junction and an arbitrary frequency-dependent environment $Z_t(\nu)$.

4.2.2 Thermal Broadening of the $P(E)$ Distribution due to Thermal Voltage Noise \bar{u} & Calculation of the Total $P(E)$ Distribution

Finite temperature in the junction leads impose fluctuations \bar{u} on the voltage drop across a tunnel junction capacitance C_J , as introduced in Sec. 3.2.3. These fluctuations act as another source or drain of energy $E = 2e(V_J + \bar{u})$, opening up another path for inelastic Cooper pair tunneling. The corresponding $P_C(E)$ distribution is of Gaussian shape and reads as [109, 107].

$$P_C(E) = \sqrt{\frac{1}{4\pi E_C k_B T}} \exp\left[\frac{-E^2}{4E_C k_B T}\right]. \quad (4.17)$$

In comparison to the expression derived in reference [107] we neglected a spectral shift of the $P_C(E)$ distribution due to Coulomb blockade, since the low DC impedance of the junction leads in our experiment, $R_{DC} \ll R_Q$, does suppress Coulomb blockade effects in the $I(V_J)$ curves.

For the experiments performed in this work these thermal fluctuations represent the only inelastic energy exchange path in addition to the interaction with the environmental impedance $Z_t(\nu)$. Hence, from these two distributions, $P_Z(E)$ and $P_C(E)$ respectively, the total probability distribution can be calculated. Since both interactions are independent of each other, the total Cooper pair tunneling probability can be obtained by convoluting $P_Z(E)$ with $P_C(E)$ [107, 109]:

$$P(E) = \int_{E_0}^{-E_0} dE' P_Z(E') P_C(E - E'). \quad (4.18)$$

Figure 4.4 compares the pure probability distributions $P_Z(E)$ with the convoluted probability distribution $P(E)$. For the calculation of both $P(E)$ distributions we employed the environmental impedance function $Z(\nu)$ introduced in Sec. 4.3. As is expected from theory, the global maximum of both distributions is located at $E = 0 \text{ eV}$ [109]. However, the amplitude of $P_Z(E)$ exceeds the amplitude of $P(E)$ by more than a factor of 30. Additionally, the $P_Z(E)$ distributions peaks much sharper with a full width half maximum (FWHM) of $\sigma_{E_Z} \leq 2 \mu\text{eV}$ compared to $\sigma_{E_Z} \leq 80 \mu\text{eV}$. We conclude that the finite temperature, as the source of voltage fluctuation, redistributes the spectral width of the $P(E)$ distribution away from the zero voltage peak to the area of finite voltage. This property is of great importance for the analysis of the measured Cooper pair tunneling curves $I(V_J)$, as will be demonstrated in Sec. 4.5.

⁴The large energy interval guarantees that the strongly oscillating functions $k(\nu)$ and $\bar{\kappa}(\nu)$ sufficiently decay to zero, otherwise the iterative calculation of $P_Z(E)$ would not converge.

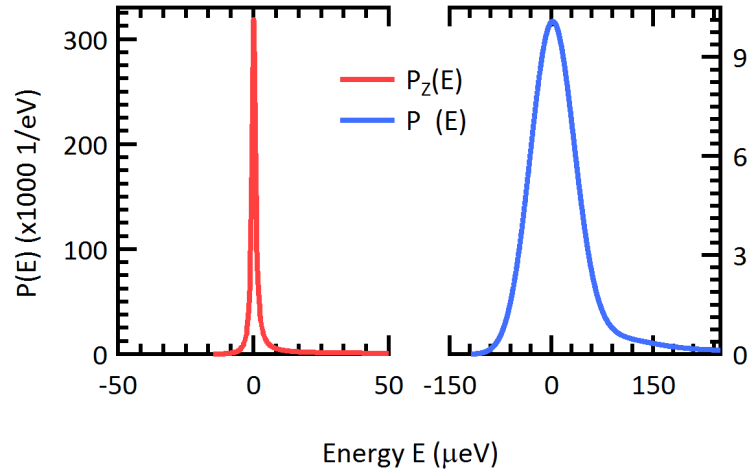


Figure 4.4 – Comparison of $P_Z(E)$, which only contains the interaction with an environmental impedance, and the total probability distribution $P(E)$.

4.3 The Environmental Impedance of a Typical STM Geometry

After deriving the necessary theoretical framework, the last piece in the puzzle, which is required to model the experimental data, is a complex-valued analytic expression for the environmental impedance $Z(\nu)$. Unfortunately, the technical constraints for operating an STM do not allow for precise tailoring of the electric environment by means of nano- and micro-lithography as is done by default in experiments on planar Josephson junctions, see e.g. Refs. [39, 62]. Therefore, the frequency-dependent impedance of the environment has to be estimated from considerations on the immediate junction environment.

First of all, the wires connecting the tunnel junction, i.e. STM tip and sample, to the measurement circuit are long transmission lines, which, from the point of view of the junction, can be considered infinitely long. Such transmission lines have a typical input impedance of $R_{DC} = 377 \Omega$, which determines the ohmic resistance $Z(0) = R_{DC}$ of the junction environment [61, 113]. The frequency-dependent part of $Z(\nu)$ can be approximated by investigating the impedance distribution on the STM tip and sample assembly schematically shown in Fig. 4.5(a). The bottom of the tip, which is $250 \mu\text{m}$ thick and typically about 1 mm long, is in electric contact with the tip holder, that forms a large plane. In contrast, the impedance of the tunnel contact at the STM tip apex is high-ohmic, $R_N = 10^4 \dots 10^6 \Omega$, for which reason we approximate the tip assembly as open-ended. Remarkably, the STM tip holder assembly shares both the electric as well as the geometric properties of a monopole antenna connected to a ground plane [113], as schematically displayed in Fig. 4.5(b). In this sense, the tip holder forms the “antenna ground plane” (see Fig. 4.5(a))⁵. Therefore, the STM tip shares a similar

⁵To clarify the terminology, the tip holder acts effectively as the antenna ground plane although in the STM the tip holder is actually not connected to ground.

Chapter 4. The Critical Josephson Current in the Dynamical Coulomb Blockade Regime

eigenfrequency spectrum with resonances at about

$$\nu_n = (2n + 1) \times c / (4(l + l_0)), \quad (4.19)$$

where the integer $n = 0, 1, 2, \dots$ denotes the n th eigenmode and l denotes the tip length with an extension l_0 corresponding to an electrical lengthening of the tip [114, 115]. A typical eigenfrequency of a millimeter long STM tip is on the order of tens of GHz. For the measurement of which the result is displayed in Fig. 4.2, for instance, a 1.7 mm long STM tip was used, whose lowest eigenmode has the frequency $\nu_0 = 30$ GHz. Converting the eigenfrequencies of this tip into voltages, $V_J = h\nu / (2e)$, we find the three lowest eigenmodes at approximately 60, 180 and 300 μeV . These values are in good correspondence to the voltage positions of the resonant current features we observed in Fig. 4.2, corroborating the validity of our geometric impedance analysis⁶.

The schematic electric field pattern derived from this impedance analysis are also shown for the three lowest eigenmodes $\nu_{0,1,2}$ in Fig. 4.5(c). The ground mode of the tip assembly corresponds to a quarter wavelength, for which reason such an antenna geometry is also called $\lambda/4$ -monopole antenna or $\lambda/4$ resonator, respectively.

Since there is no analytic expression for a monopole antenna, we approximate the STM tip's impedance spectrum by an open-ended transmission line [113]. This is a valid approximation since the open-ended transmission line and a monopole antenna share similar impedance properties – a large impedance mismatch at one end and an impedance match at the other end – which results in a similar excitation spectrum. However, this approximation neglects any influence of the ground plane on the electromagnetic properties of the antenna. The input impedance of the open-ended transmission line seen by the junction $Z_T(\nu)$ reads as follows⁷ [107, 113]:

$$Z_T(2\pi\nu) = Z(0) \frac{1 + \frac{i}{\alpha} \tan\left(\frac{\pi\nu}{2\nu_0}\right)}{\left[1 - \bar{\kappa} \frac{\nu}{\nu_0} \tan\left(\frac{\pi\nu}{2\nu_0}\right)\right] + i\alpha \left[\kappa \frac{\nu}{\nu_0} + \tan\left(\frac{\pi\nu}{2\nu_0}\right)\right]}. \quad (4.20)$$

Here, $Z(0)$ denotes the input impedance of the tip, which for monopole antennas is typically $Z(0) = 36\Omega$ [113]. This value is much smaller than the input impedance of the transmission line $R_{DC} = 377\Omega$ connecting the sample. Since the thermal resistor noise amplitude, causing phase fluctuations, is dominated by the largest value of the ohmic resistance, we reduce the number of parameters and set the input impedance of the tip $Z(0)$ equal to the input impedance of the transmission line R_{DC} . The dimensionless parameter α is a measure for the quality of the eigenmodes — smaller values correspond to eigenmodes of better quality — and ν_0 denotes the $n = 0$ eigenfrequency of the tip. The parameter $\bar{\kappa} = \nu_0 Z_0 C_J$ results from the capacitive shunt of the junction by itself and, thereby, acts as an effective short-pass

⁶For this particular tip length the lowest eigenmode ν_0 is hidden in the falling flank of the supercurrent peak.

⁷In comparison to the pure environmental impedance $Z(\nu)$, the impedance $Z_T(\nu)$ also contains the junction capacitance C_J , which shunts the junction itself (e.g. Ref. [109]).

4.4. Implementation of $P(E)$ -Theory as Fitting Routine

filter, where $Z_0 \approx 377\Omega$ is the vacuum impedance. Figure 4.5(c) displays an example of the calculated environmental impedance $Z_T(\nu)$ of the STM tip assembly.

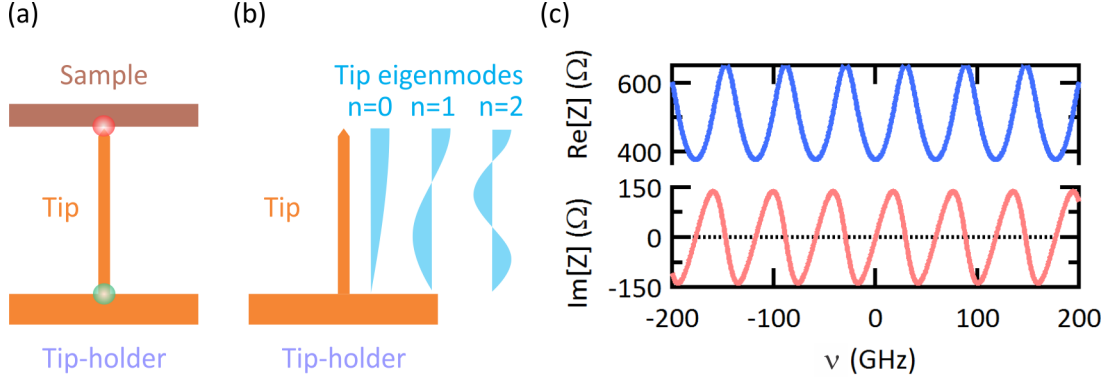


Figure 4.5 – (a) Sketch of the STM tip sample assembly. The red dot indicates a point of large resistance R_1 and the green dot indicates a point of small resistance R_2 . (b) Monopole antenna analogue of the STM tip. The lowest eigenmodes of the tip holder assembly ν_n are displayed and indicated. (c) Complex impedance of a transmission line as a function of the frequency for a resonance frequency $\nu_0 = 30\text{GHz}$, a damping $\alpha = 0.75$ and a short-pass constant $\bar{\kappa} = 0.005$.

4.4 Implementation of $P(E)$ -Theory as Fitting Routine

With a theoretical model and the environmental impedance in hand, we can fit the experimentally measured $I(V_J)$ characteristics. However, the challenge in fitting such a curve using $P(E)$ -theory lies in the rather involved interplay of the different fitting parameters, as well as in the large range of varying tunneling current amplitudes. Therefore, the experimental parameters require more detailed consideration.

- We use the effective temperature of $T_{\text{eff}} = 40\text{mK}$ for the calculation of P_C . The effective temperature of the Josephson junction itself may also be higher, because we can not perfectly shield it from stray photons. Although the STM head forms a closed metal body, isolation ceramics for the wire feedthroughs are transparent for photons in the MHz to GHz range. For the calculation of $P_Z(E)$ we therefore estimated the effective temperature of the Josephson junction to $T = 100\text{mK}$, which results in a slightly better fit, as compared to effective temperatures of either 50 or 150 mK, respectively.
- As discussed before, we can keep the ohmic resistance fixed at the input impedance of a transmission line $R_{DC} = 377\Omega$.
- For typical experimental values of $C_J \approx 1\text{fF}$ and $\nu_0 \approx 30\text{GHz}$ the short-pass parameter is small, $\bar{\kappa} \approx 0.01$. Since it, in general, has only a very small effect on the spectral properties it will be kept constant for the further analysis at a value of $\bar{\kappa} = 0.01$.

Chapter 4. The Critical Josephson Current in the Dynamical Coulomb Blockade Regime

To account for the constant current background of the current amplifier, the equation for the Cooper pair tunneling current, Eq. 4.10, is extended by a constant current offset, c_1 . The gap-filling due to quasiparticle excitations (cf. Ch. 2, Sec. 2.2.3) is considered by adding a cubic background c_2 to the current equation. We find the final fitting function for the Cooper pair tunneling current

$$I(V_J) = \frac{\pi e E_J^2}{\hbar} [P(2eV_J) - P(-2eV_J)] + c_1 + c_2 \times V_J^3. \quad (4.21)$$

Incorporating these assumptions, we can fit the experimental $I(V_J)$ curve at $G_N = 0.27 G_0$, as shown in Fig. 4.6. The fit nicely reproduces both the supercurrent peak as well as the spectral resonances and we can extract a Josephson coupling energy of $E_J = 46.60 \pm 0.12 \mu\text{eV}$. The environmental impedance $Z(\nu)$ shows its lowest eigenmode frequency at $\nu_0 = 29.47 \pm 0.20 \text{ GHz}$. This value matches the expected $\lambda/4$ -resonance of the $l = 1.7 \pm 0.1 \text{ mm}$ long tip used in this experiment. The corresponding damping factor, $\alpha = 0.76 \pm 0.01$, has a rather large value, which can be attributed to the intrinsically low quality factors of antennas⁸. For the junction capacitance, we find a value of $C_J = 2.16 \pm 0.04 \text{ fF}$. This value is in good agreement with our estimates in the experimental setup, which only comprises the junction capacitance between tip and sample on the order of femtofarads.

We conclude that the $I(V_J)$ curves from our small capacitance tunnel junction, showing the characteristics of sequential Cooper pair tunneling, can be nicely modeled by $P(E)$ -theory with reasonable parameters. Moreover, we are able to unambiguously determine an experimental value of the Josephson coupling energy E_J in a particular junction. In the following section we will explore the conductance range of applicability for our implementation of $P(E)$ -theory.

4.5 Testing the Range of Validity for $P(E)$ -Theory

Comparing the relevant energy scales of our experiment in Fig. 4.1 at the beginning of this chapter we found that we can tune the ratio of Josephson coupling energy E_J versus capacitive charging energy of the junction when changing the tunneling conductance G_N via the tip-sample distance. In this way, we can tune the Josephson junction from the DCB regime $E_J \ll E_C$ at $G_N \ll G_0$ to a regime in which the Josephson coupling energy is comparable to the charging energy $E_J \approx E_C$ at $G_N \approx G_0$. However, $P(E)$ -theory was derived exclusively for the DCB regime so that it should fail to describe Cooper pair tunneling characteristics in this limit. To address this interesting question, which has remained open so far, we will in this section investigate the tunneling characteristics of the Josephson junction in our STM in the limit $G_N \rightarrow G_0$.

To this end, we measure the $I(V_J)$ curves for a wide range of tunneling conductance val-

⁸The purpose of antennas is to radiate the excitation into free space. Hence, in contrast to resonator cavities, the quality is strongly reduced.

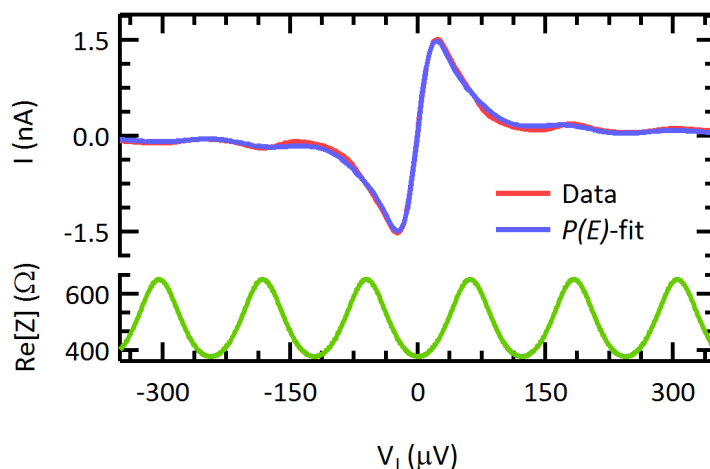


Figure 4.6 – Example of a $P(E)$ -fit to an $I(V_J)$ spectrum measured at $G_N/G_0 = 0.27$ and $T = 15$ mK. On the bottom, the real part of the environmental impedance that results from the fit is shown.

ues $0.05 G_0 \leq G_N \leq 0.27 G_0$ which are shown in Fig. 4.7(b). All curves exhibit a well-defined supercurrent peak, symmetrically centered around zero bias, as well as spectral current resonances. Deviations are found in the background signal that originates from quasiparticle excitations. To smaller values of the tunneling conductance the quasiparticle background current increases and appears more pronounced, as compared to the Cooper pair tunneling current features. Figure 4.7 also shows that by using $P(E)$ -theory in the same fashion as before we are able to nicely model all $I(V_J)$ curves along the entire conductance range that spans almost three orders of magnitude. Concerning the fit parameter shown in Fig. 4.8, we find that neither the junction capacitance C_J nor the impedance properties, ν_0 and α , depend on the tunneling conductance. This result is certainly expected, since the spectral energy exchange probability distribution does not depend on the tunneling conductance. Still, it corroborates the consistency of our $P(E)$ implementation and fitting routine as well as our capability to correctly model $I(V_J)$ tunneling curves with $P(E)$ -theory.

In our case, the regime $G_N \rightarrow G_0$ is also of particular interest, since here the initial requirement of $P(E)$ -theory, $E_J \ll E_C$, is not valid anymore (cf. Fig. 4.1). We should accordingly fail to describe our experimental data with $P(E)$ -theory. Additionally, Ingold *et al.* found that the global condition $E_J \ll E_C$ is superimposed by another condition $E_J \times P(E) \ll 1$ [109]. This condition must hold for any applied bias voltage $V = E/(2e)$ and for this reason, it is much more stringent than $E_J \ll E_C$. In order to test this hypothesis, we measured the $I(V_J)$ curves for tunneling conductance values $G_N \geq 0.59 G_0$ of which three examples are shown in Fig. 4.9. Using $P(E)$ -theory as before, we were unable to properly fit any of these spectra, which is to be expected since, at the measured conductance values, we find $E_J \approx E_C$ (cf. Fig. 4.1). Nevertheless, we can up-scale a fitted current spectrum from experiments at a lower conductance, $G_N = 0.27 G_0$, making use of E_J only being an independent scaling

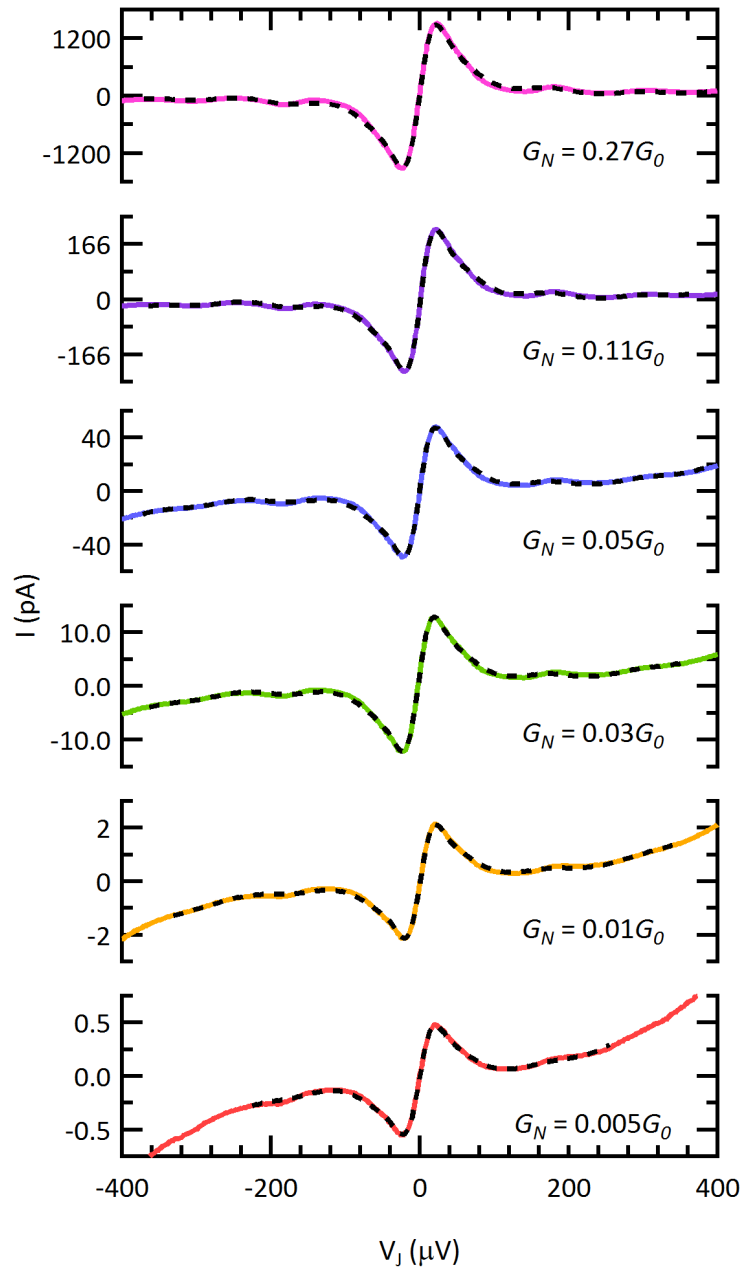


Figure 4.7 – Experimental tunneling spectra $I(V_J)$ (color lines) and fit to data (black dashed lines) for indicated tunneling conductance values measured at $T = 15$ mK.

4.5. Testing the Range of Validity for $P(E)$ -Theory

factor. The up-scaled $I(V_J)$ curve nicely fits the spectral resonances at higher voltages, but largely overestimates the supercurrent peak in all cases with increasing mismatch for higher conductance values, as shown in Fig. 4.9, indicating the breakdown of $P(E)$ -theory.

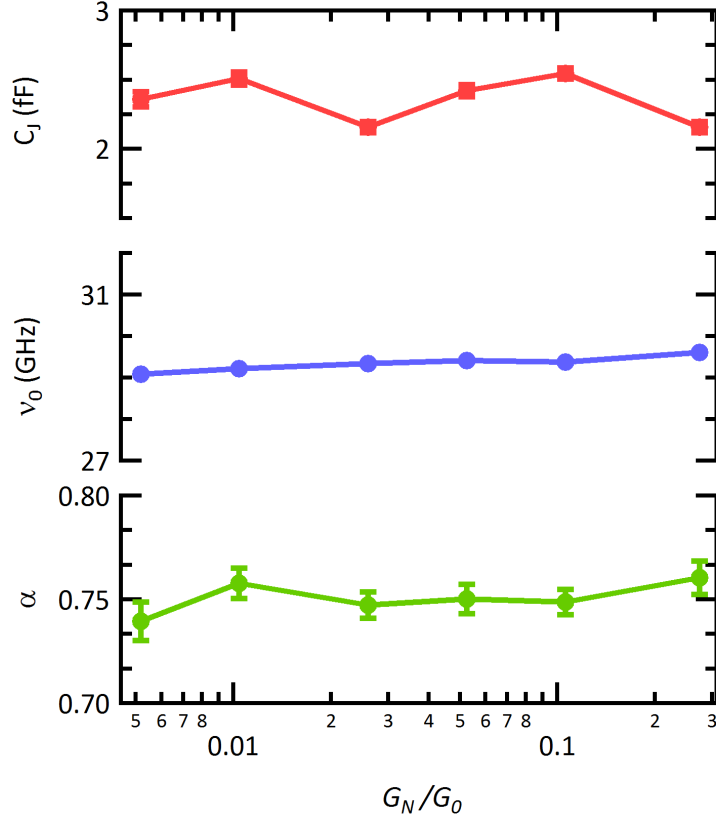


Figure 4.8 – Fitted values for the junction capacitance C_J , the lowest eigenmode frequency ν_0 and the damping α as a function of the normalized tunneling conductance G_N/G_0 .

To better understand this observation, we investigated the product $E_J \times P_{\max}$. For E_J we use the values found from upscaling the $I(V_J)$ curves. P_{\max} is the global maximum of the calculated probability distribution $P(E)$. It is found at zero voltage for the probability distribution of the impedance $P_Z(E)$ as well as for the total convoluted probability distribution $P(E)$ (see Fig. 4.4) [109]. It can be seen that the broadening of the total $P(E)$ due to the thermal voltage noise \bar{u} greatly reduces the maximum value of the $P(E)$ distribution, as compared to $P_Z(E)$. The dependence of $E_J \times P_{\max}$ on the tunneling conductance G_N is shown in Fig. 4.10. For $G \geq 0.59 G_0$, we find $E_J \times P_{\max} \geq 1$ so that the required condition for $P(E)$ -theory is “locally” violated near zero voltage. This result perfectly explains our observation that $P(E)$ -theory still nicely models the spectral resonances at higher bias voltages, where $E_J \times P(E \gg 0) \ll 1$, but fails for the supercurrent peak close to zero bias, where $P(E)$ has its maximum and $E_J \times P(E \approx 0) \approx 1$.

This result indicates that the Cooper pair tunneling current at low voltages is dominated by the *coherent* tunneling of Cooper pairs whereas at higher voltages the *sequential* Cooper pair

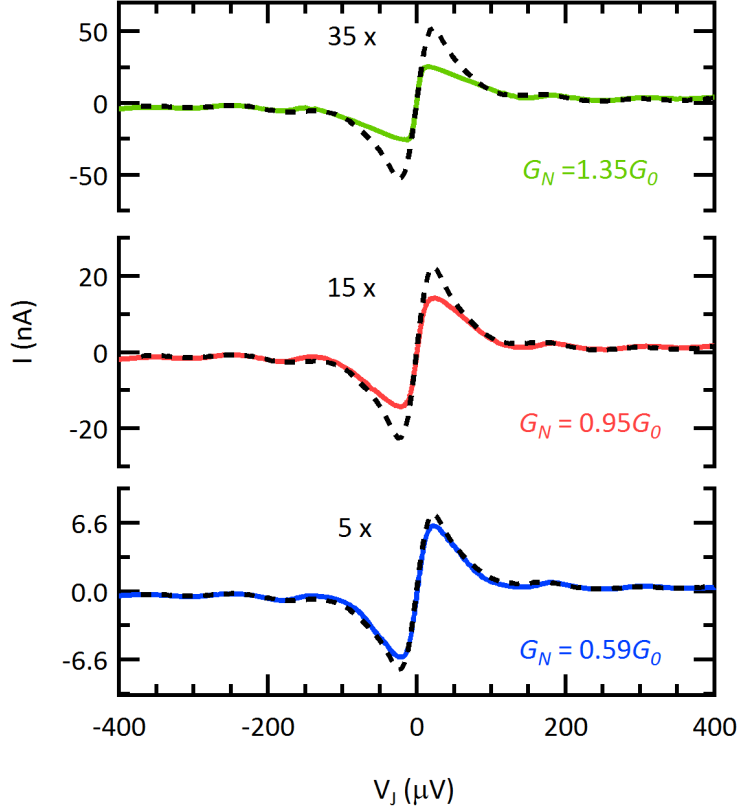


Figure 4.9 – Experimental tunneling spectra $I(V_J)$ (color lines) and up-scaled fits (black dashed lines) for indicated tunneling conductance values measured at $T = 15$ mK.

tunneling dominates the current. For this reason $P(E)$ -theory fails to describe the entire $I(V_J)$ curve. This result is somewhat expected, since in the regime $E_J \gg E_C$ the tunneling current is sustained by the coherent tunneling of Cooper pairs and scales with the Josephson critical current I_0 or the Josephson coupling energy E_J , respectively [31, 62]. Hence, as soon as Ingold's condition for sequential Cooper pair tunneling is violated, the Cooper pair current, which is most likely dominated by coherent Cooper pair tunneling, will not scale as $\propto E_J^2$ anymore but rather scales as $\propto E_J$. For this reason, $P(E)$ -theory will overestimate the Cooper pair current amplitude around zero voltage, as is also reported by another group [116]. Our result also signifies that the turnover from the sequential Cooper pair tunneling regime to the coherent Cooper pair tunneling regime does not occur at a specific ratio E_C/E_J but continuously around the turning point $E_C/E_J = 1$.

In order to discuss this physical interpretation we compare our experimental results with a condition for coherent Cooper pair tunneling, which has been evaluated independently from $P(E)$ -theory by Falci *et al.* [110]. The authors investigated the effective action of a Josephson junction employing the imaginary-time path-integral formalism [117, 118]. For a purely ohmic environment $Z(0)$ they found that coherent tunneling occurs as long as the condition

4.5. Testing the Range of Validity for $P(E)$ -Theory

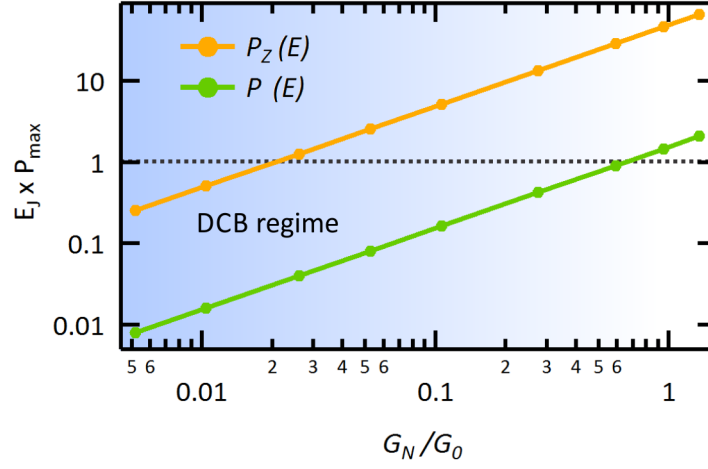


Figure 4.10 – Ingold's condition $E_J \times P_{\max}$ calculated for $P_Z(E)$ and $P(E)$ as a function of the normalized conductance G_N/G_0 .

$\bar{\gamma} = E_J/(E_C \times \bar{\alpha}^{1/2}) > 1$ holds, where $\bar{\alpha}$ is defined as $\bar{\alpha} = R_Q/Z(0)$. Fig. 4.11 displays $\bar{\gamma}$ as a function of the normalized tunneling conductance. For E_C and E_J we used the values found from the fit and as before, we set $Z(0) = R_{DC} = 377\Omega$. In fact, for the entire conductance range we find $\bar{\gamma} < 1$ so that tunneling current is still carried by the sequential tunneling of Cooper pairs, as we found from our analysis using $P(E)$ -theory. For $G_N/G_0 > 1$, $\bar{\gamma}$ approaches unity, which indicates the turnover to the coherent tunneling regime in the framework of this theory, similar to the condition $E_C \gg E_J$. However, both conditions $\bar{\gamma} > 1$ and $E_C \gg E_J$, respectively, are global conditions and it requires the more stringent, local requirement $E_J \times P(E) \ll 1$ in order to properly explain our experimental results.

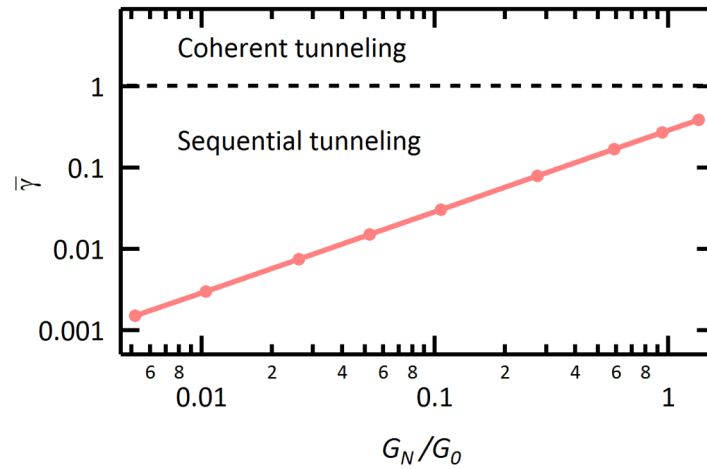


Figure 4.11 – The parameter $\bar{\gamma}$ as a function of the normalized conductance G_N/G_0 [110].

Moreover, the analysis of the $P(E)$ function reveals the significance of the thermal voltage noise as a spectral broadening mechanism (cf. Sec. 3.2.3 and 4.2.2). We cannot fit the experimental data by $P(E)$ -theory without considering the capacitive noise broadening. While the probability distribution in the convoluted $P(E)$ -function is broadened and has some spectral weight at higher voltages, the $P_Z(E)$ distribution – only containing the interaction with the frequency-dependent environment – sharply peaks at $V_J = 0$ (see Fig. 4.4). For this reason, the required condition $E_J \times P_{Z,\max} \ll 1$ is violated for almost the entire conductance range as shown in Fig. 4.10. This is in agreement with theory, which predicts failure of $P(E)$ -theory for a tunnel junction that is operated in a low impedance environment, i. e. $R_{DC} \ll 1/R_Q$. However, including the capacitive noise broadening [109, 107] is necessary to correctly describe the experimentally observed sequential Cooper pair tunneling, because we still work at non-zero temperatures. It reduces the P_{\max} values and results in an overall consistent picture between experiment and theory as well as the range of validity for $P(E)$ -theory.

4.6 The Josephson Critical Current in the Dynamical Coulomb Blockade Regime

In the last section, we demonstrated that we can model Cooper pair tunneling characteristics using $P(E)$ -theory over a large range of tunneling conductance values and that $P(E)$ -theory is valid across this range. We can therefore unambiguously determine the local value of the Josephson coupling energy E_J . However, in order to access the local superconducting order parameter Δ via Josephson STM, it is necessary to determine the local value of the Josephson critical current I_0 , simply related to E_J via natural constants, $I_0 = (2e/\hbar)E_J$. However, the well-known formulation of the Josephson critical current derived by Ambegaokar and Baratoff [8], which relates I_0 to Δ , was derived at exactly zero voltage, where the tunneling current is purely carried by the coherent tunneling of Cooper pairs. Such a case corresponds to a large planar junction of large capacity and small tunneling resistance, in which E_C and both quantum and thermal fluctuations can be disregarded. As we have demonstrated in the previous sections, STM experiments are commonly operated in the dynamical Coulomb blockade regime, in which the Cooper pair tunneling current is dominated by the sequential tunneling of Cooper pairs. For this reason it is *a priori* not clear that the experimentally determined E_J values will result in the Josephson critical current as defined by Ambegaokar and Baratoff. To quantitatively compare the experimentally found values for the critical current with the critical current calculated from the AB formula, we again write this formula for two superconductors with unequal order parameters $\Delta_{1,2}$, where $\Delta_1 > \Delta_2$, and zero temperature⁹ (cf. Eq. 2.21 in Sec. 2.2.5)[8]:

$$I_0 = \Delta_2 G_N K \left(\sqrt{1 - \frac{\Delta_2^2}{\Delta_1^2}} \right). \quad (4.22)$$

⁹In good approximation we can neglect the temperature.

4.6. The Josephson Critical Current in the Dynamical Coulomb Blockade Regime

To gain access to the order parameters Δ_1 and Δ_2 , we measured the quasiparticle excitation spectrum of the tunnel junction in our STM, which is shown in Fig. 4.12. In the lower panel the differential conductance proportional to the LDOS is displayed. The upper panel shows the second derivative, which enhances the positions of the Andreev reflections. The differential conductance shows two peaks at $\Delta_1 + \Delta_2 = 1210 \mu\text{eV}$ as well as in-gap states. We find an Andreev reflection that is associated with the sample gap Δ_1 at $eV \approx 760 \mu\text{eV}$ [50, 53]. Due to lifetime effects of Cooper pairs in the STM tip, the spectral features in the dI/dV spectrum are broadened [54]. Still, the gap values can be extracted from the d^2I/dV^2 -spectrum at $\Delta_1 = 760 \pm 70 \mu\text{eV}$ and $\Delta_2 = 450 \pm 20 \mu\text{eV}$.

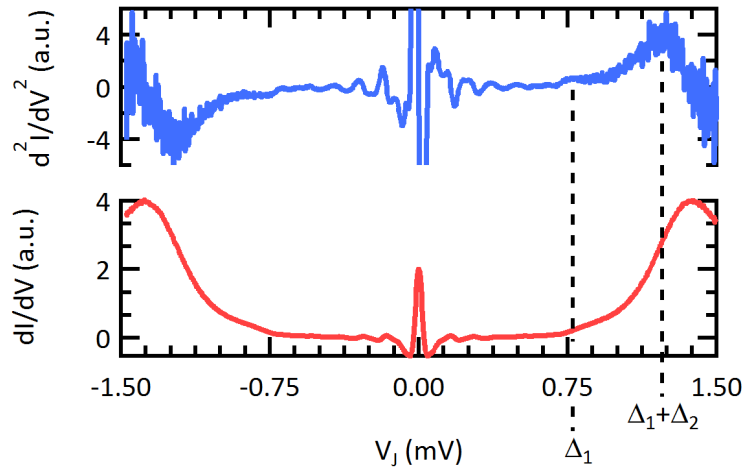


Figure 4.12 – First derivative dI/dV_J of the tunneling current (bottom) and second derivative d^2I/dV_J^2 (top), respectively.

Inserting these values along with the tunneling conductance G_N into the AB formula, we can plot the corresponding critical currents in Figure 4.13 as a function of the normalized tunneling conductance G_N/G_0 . The critical currents from the $P(E)$ -fits and the AB formula match within error bars over the entire range of tunneling conductance where $G_N \leq 0.27 G_0$. On the bottom, Fig. 4.13 also displays the relative deviation δI_0 between calculation and experiment, $\delta I_0 = 100 \times |I_{0,\text{exp}} - I_{0,\text{calc}}|/I_{0,\text{calc}}$. In all cases, δI_0 is smaller than 10% and we determine its standard deviation to $\sigma_{\delta I_0} \leq 5\%$. The agreement between the experimental and the calculated critical current is a remarkable observation, because the experimental values were determined from sequential Cooper pair tunneling characteristics, whereas the AB formula was derived for coherent Cooper pair tunneling. Hence, our findings suggest that the critical current I_0 represents a coupling strength between the overlapping pair wavefunctions and that this coupling strength is independent of the actual tunneling process – a question that remained open in the original work of Ambegaokar and Baratoff [8]. In this sense, the spectral weight of the Cooper pair tunneling current in the DCB regime, $E_J \ll E_C$, is distributed at finite voltages, while it peaks at zero voltage for Josephson junctions of negligible capacitive charging energy, such that $E_J \gg E_C$.

In Fig. 4.13 we also compare the critical current values of the up-scaled fits with the values calculated using the AB formula. Here, the deviation is much larger, $\delta I'_0 \leq 41\%$, which, however, is not too surprising. The large tunneling conductance in these experiments, $G_N/G_0 \geq 0.59$, clearly violates the weak coupling limit, i.e. $G_N \ll G_0$, for the perturbative calculation of the Cooper pair current through the Josephson junction (cf. Sec. 2.2.5) [7, 8]. Instead, it could be experimentally shown, that the Cooper pair current through transparent Josephson contacts, i.e. $G_N \approx G_0$, results from a population imbalance of Andreev bound states on each side of the atomic contact altering the sinusoidal phase relationship of the Josephson effect in the weak coupling limit [119]. As a consequence, the critical Josephson current in this limit deviates from the result obtained by Ambegaokar and Baratoff, as we could also find indications for in our experimental data. Moreover, in this so-called *Andreev bound state model* the Cooper pair current is transmitted through the i number of conductance channels of the Josephson contact, whereby each of them has a specific, yet arbitrary, transmission τ_i [120, 121]. For this reason, this theory can be applied to a variety of Josephson contacts ranging from the tunnel junction, as studied in this work, to ballistic contacts. However, we only recently started to investigate our tunnel contact configuration in more detail by using a Hamiltonian approach as given in Ref. [122]. Until now, we lack knowledge on the precise number of conductance channels as well as their respective transmission and for this reason, the discussion on the critical Josephson current in the limit $G_N \rightarrow G_0$ has to remain on this qualitative level.

It should be noted that the formulation of the Josephson critical current as derived by Ambegaokar and Baratoff [8] corresponds to the limit of many poorly transmitting channels, i.e. $i \rightarrow \infty$ and $\tau_i \ll 1$, of the Andreev bound state model [123]. Hence, it should only be possible to reach the Ambegaokar-Baratoff critical current, if the tunnel contact consists of a sufficiently large number of conductance channels. This requirement is certainly met for planar tunnel junctions of large junction area, as experimentally demonstrated by Steinbach *et al.* [62], but not *a priori* fulfilled for the atomic scale tunnel junction in an STM. In our case this turns out as an interesting observation. We found great agreement between our experimentally determined critical current values and the calculated values using the AB formula, which indicates that the tunnel junction in an STM in fact consists of a large number of conductance channels. This observation is in stark contradiction to the commonly-used hypothesis that in STM experiments only one poorly transmitting conductance channel contributes to the tunneling current [75]. Since the tunnel contact configuration in an STM recently attracted an increasing amount of interest [124, 125], we will address this interesting problem in future work.

4.7 Conclusion

In summary, we have investigated the $I(V_J)$ tunneling characteristics of a voltage-biased Josephson junction in the DCB regime for the purpose of JSTM. We showed that using $P(E)$ -theory, we are able to describe the experimental data with high accuracy and extract the Josephson coupling energy E_J . We also observed indications for the continuous transition

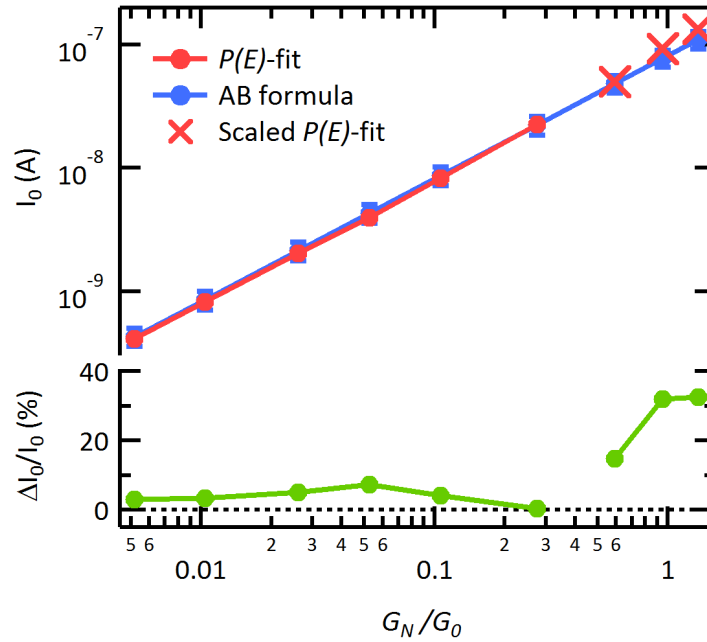


Figure 4.13 – Critical current I_0 as found from the $P(E)$ -fit to the experimental data and calculated using the AB formula (top). Relative deviation between fitted and calculated I_0 values (bottom).

from the regime of pure sequential Cooper pair tunneling to a regime, in which both sequential Cooper pair tunneling *and* coherent tunneling sustain the tunneling current in the same spectrum but at different energies. In this way, we could experimentally determine the range of validity for $P(E)$ -theory and, at the end, define a parameter range for JSTM to work best. Furthermore, we found that the Josephson critical current values $I_0 = 2e/\hbar E_J$, as calculated from the experimental E_J values, are equivalent to the theoretical values calculated by using the Ambegaokar-Baratoff formula [8]. The DCB regime, which is predominantly accessible in STM, can therefore be used to directly determine unambiguous values of the critical Josephson current I_0 . This result represents the fundamental step towards the implementation of JSTM as a versatile spectroscopic tool for studying superconductor physics on the atomic scale [14, 16, 17, 18].

5 The AC Josephson Effect as a GHz Source on the Atomic Scale

The content of this chapter is published as a letter in *Applied Physics Letters* **106**, 013109 (2015) entitled *A nanoscale gigahertz source realized with Josephson scanning tunneling microscopy* by the authors Jäck, B., Eltschka, M., Assig, M., Hardock, A., Etzkorn, M., Ast, C.R. and Klaus Kern.

5.1 Introduction

Within the last chapter we showed that using $P(E)$ -theory it is possible to describe the $I(V)$ -characteristics of a Josephson junction operated in the dynamical Coulomb blockade regime (DCB). Our experimental data reveals the high sensitivity of the Josephson junction in our STM to its immediate, frequency-dependent environment $Z(\nu)$. In particular, this sensitivity enables inelastic Cooper pair tunneling via energy exchange processes with the electromagnetic environment $Z(\nu)$. From a simple geometric analysis we found that the frequency-dependent impedance $Z(\nu)$ of a typical STM geometry, such as that shown in Fig. 5.1, is dominated by the tip holder sample geometry and shares the electric properties of a $\lambda/4$ -monopole antenna.

In this chapter, we study the electromagnetic properties of the $\lambda/4$ -monopole antenna and its interaction with the Josephson junction in more detail. On the one hand, the combination

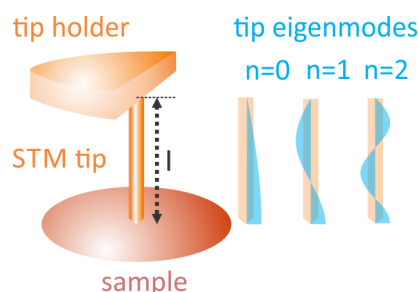


Figure 5.1 – Conceptual sketch of the STM tip holder sample geometry and the three lowest tip eigenmodes.

of a Josephson junction and a resonator in its immediate environment represents a valuable tool for studying the photon emission process from tunneling and has recently attracted an increasing amount of research interest [105, 126, 127]. In particular, possible nonlinear interactions of an excited resonator and a Josephson junction are predicted by theory [106].

On the other hand, combining the junction's sensitivity to GHz signals with a resonator of GHz resonance frequencies could allow us to realize a spectroscopy tool for GHz signals at the nano-scale, a concept that has already been successfully demonstrated on planar junction geometries [22, 23]. It is of great interest to introduce this frequency range into the vivid research field of nano scale science, because it would facilitate a new approach for investigations on individual molecular magnets [24] or the physics of individual nuclear as well as electronic spins, for instance [128, 129]. However, generating and guiding GHz signals from outside the experimental setup into the tunnel junction requires adaptation to the experimental conditions of STM, adding another level of complexity. All recent realizations of an STM employing high frequency radiation (HF) feed externally generated HF-signals into the junction by means of optical guiding or waveguides [130, 131]. As we will show in the following, the fundamental aspect of this study lies in circumventing the external feed and, instead, realizing both GHz signal *generation* as well as *detection* right in the tunnel junction. To this end, we combine the AC Josephson effect, acting as a perfect voltage V_J to frequency ν converter through the relation $h\nu = 2eV_J$, with the tip resonator that provides the necessary electromagnetic eigenmode spectrum. This unique combination, along with the junction's sensitivity to its immediate electromagnetic environment and the local probe capabilities of an STM, could make the *AC Josephson STM* an ideal broadband atomic scale spectroscopy tool operating under UHV conditions.

5.2 Tuning the Tip Eigenmodes

In Section 4.3 we found, from a simple analysis of the geometric impedance distribution, that the tip holder assembly shares the electric properties of a $\lambda/4$ -monopole antenna. Since the eigenmode energy of such a monopole antenna reciprocally depends on the antenna length l (cf. Eq. 4.19), we should be able to tune the position $V_J = h\nu/(2e)$ of the resonance current peaks in the nanoscale Josephson junction by changing the length l of the STM tip (cf. Fig. 5.1). In order to test this hypothesis, we measure $I(V_J)$ curves for different tip lengths ranging from $l = 2.7 \pm 0.1$ mm to $l = 0.7 \pm 0.1$ mm, which are shown in Fig. 5.2. It can be clearly seen from the spectra that the current resonance peaks move to higher energies as the tip length l is reduced. The highest measured current peak that we observe for an $l = 0.7 \pm 0.1$ mm long STM tip corresponds to a resonance frequency of the lowest eigenmode exceeding 200 GHz. For longer tips we cannot, however, resolve a footprint of the $n = 0$ mode in the $I(V_J)$ curves, which in these cases is part of the falling flank of the supercurrent peak close to zero voltage. Still, the characteristics of the visible current resonances unambiguously reflect the typical eigenmode spacing of a monopole antenna (cf. Eq. 4.19).

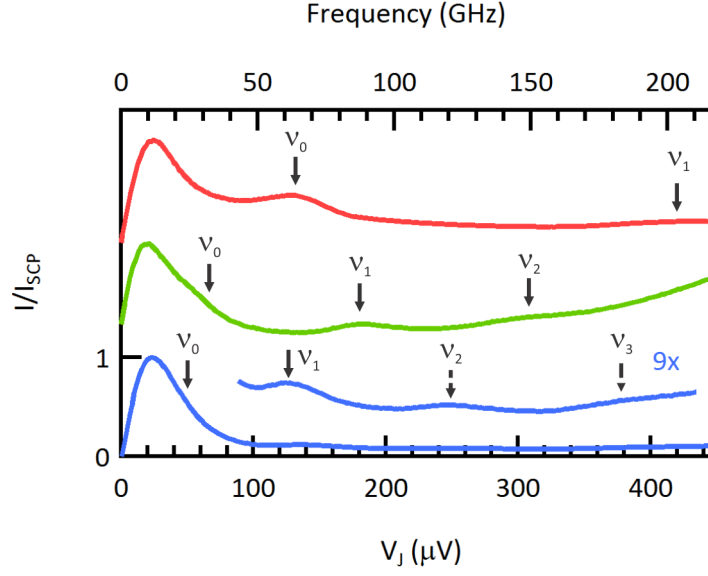


Figure 5.2 – $I(V_J)$ curves, normalized to the supercurrent peak amplitude I_{SCP} , for experiments at a conductance $G_N = 0.1 G_0$ using STM tips of different length $l = 2.7 \pm 0.1$ mm, $l = 1.7 \pm 0.1$ mm and $l = 0.7 \pm 0.1$ mm, from bottom to top. The tip eigenmodes v_n are indicated at the corresponding current resonance.

By comparing the $I(V_J)$ curves in Fig. 5.2, we also find that the amplitude of the current resonances is enhanced when the tip length is reduced. We can explain this observation in a descriptive fashion if we consider the current distribution oscillating along the antenna. Similar to the well-known dipole antenna, where the current oscillates between the two edges of the antenna, the current on the monopole antenna oscillates between the antenna apex and the outer edge of the ground plane. In other words, the ground plane constitutes the monopole antenna's second half and acts as an electric counter weight [113]. As a general rule, the ground plane radius r should not be smaller than the antenna length.

Considering the various tip lengths we used in our experiment, we find that only the $l = 0.7 \pm 0.1$ mm STM tip matches the rule $r/l \approx 1$ and, moreover, that for this particular tip length the current resonances have the largest amplitude. To further investigate the relation between antenna ground plane size and antenna properties, we change the tip holder surface area, which is shown in Fig. 5.3(a). While the antenna length, $l = 0.7 \pm 0.1$ mm, stays the same, we increase the surface area by a factor of three. Figure 5.3(b) displays the measured $I(V_J)$ curves for these two different tip holder geometries. For the larger surface area A_1 , the peak amplitude more than doubles compared to the smaller surface A_2 , where it almost reaches the supercurrent peak amplitude. In contrast, the voltage position of the current resonance at the corresponding voltage $V_J = hv_0/2e$ remains unaffected. Hence, we experimentally observe that changing both the length of the tip and the size of the tip-holder strongly changes the electromagnetic properties of the tip holder assembly, i.e. of the monopole antenna.

To quantitatively analyze the relation between the geometry and the electromagnetic prop-

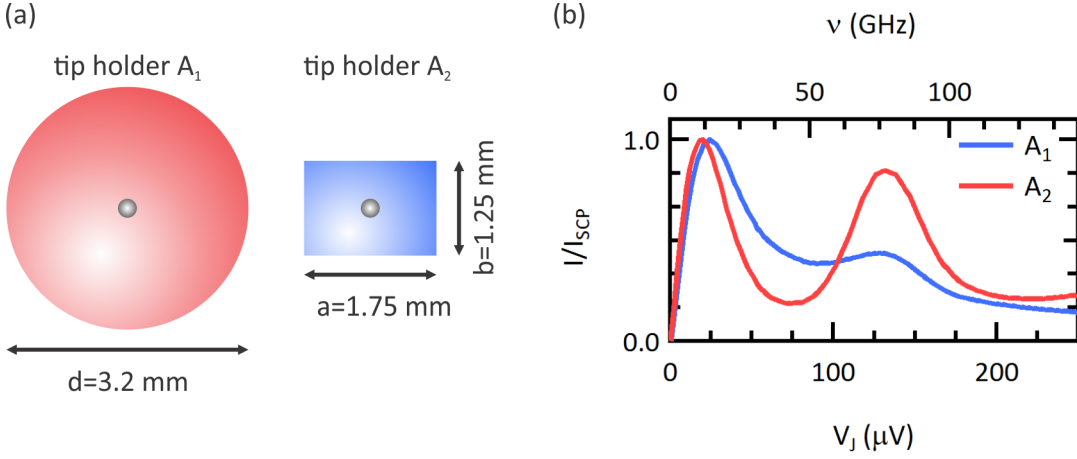


Figure 5.3 – (a) Sketch of the two different tip holder surface geometries used for the experiments (The dimensions are indicated). (b) $I(V_J)$ curves, normalized to the supercurrent peak, for experiments with different tip holder surfaces A_1 and A_2 , both measured at a conductance $G_N = 0.1 G_0$.

erties of the tip holder assembly we employ the particularities of $P(E)$ -theory, namely, that the current features – expressing the spectral energy exchange probability $P(E)$ with the environment – directly relate to the impedance $Z(\nu)$ of the tip holder assembly. In this sense, we perform an impedance spectroscopy by using the sequential Cooper pair tunneling current as a probe [39]. To this end, we fit the experimental $I(V_J)$ curves with $P(E)$ -theory in the same fashion as introduced in the last chapter (cf. Ch. 4, Sec. 4.4). From the fits we can extract the properties of the tip impedance $Z(\nu)$ which are its lowest mode frequency ν_0 and the damping parameter α (cf. Eq. 4.20). In Fig. 5.4(a) we plot the frequency of the lowest eigenmode ν_0 for the different measured tips and tip holder shapes as a function of the tip length l . Their values nicely follow the inverse proportionality to the tip length as found in Ch. 4, Sec. 4.3 from a simple geometric impedance analysis. Using the relation between the tip length and the lowest eigenmode frequency,

$$\nu_0 = c / (4(l + l_0)), \quad (5.1)$$

we can fit the dependence of ν_0 on the tip length l and extract an electrical lengthening of $l_0 = 0.46 \pm 0.04$ mm. This rather large value, even exceeding the shortest tip length, is not surprising, because lengthening effects are predominantly observed for antennas of non-negligible thickness, as is the case with our STM tips [115, 113]: For the shortest tip, $l = 300 \mu\text{m}$, we are in the extreme limit in which the antenna length is even comparable to its thickness $d = 250 \mu\text{m}$.

Quantitatively analyzing the relation between the fitted α values and the geometric parameters remains difficult, because the impact of the ground plane geometry on the electromagnetic properties of the antenna is rather complex [115]. Hence, it is not possible to derive an analytical expression for the antenna impedance $Z(\nu)$ that connects to the geometry, for

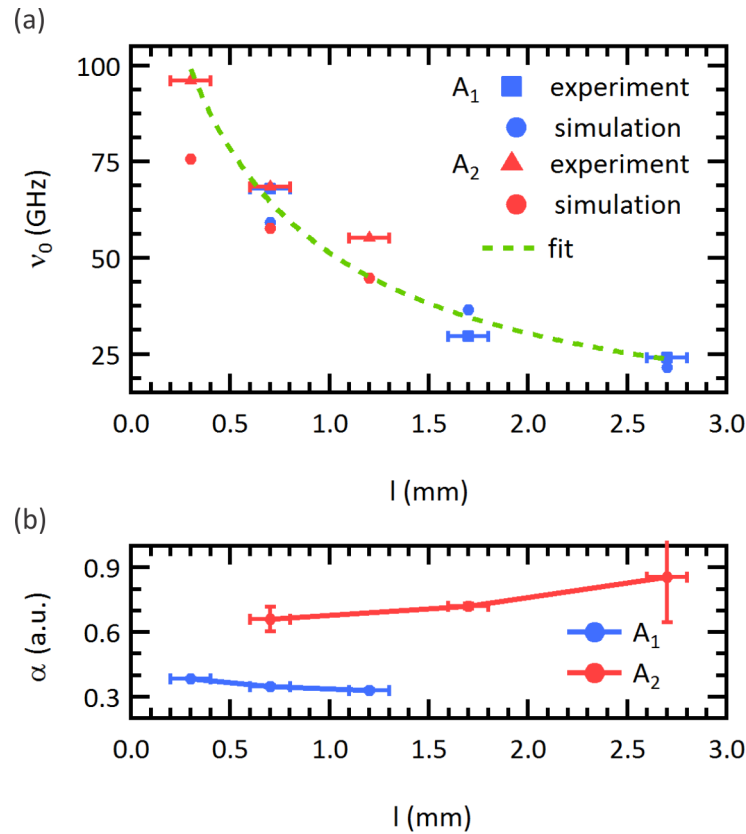


Figure 5.4 – (a) Lowest eigenmode frequency ν_0 as a function of the tip length l for both tip holder geometries A_1 and A_2 , respectively, found from the $P(E)$ -fits to the $I(V_j)$ curves and the FIM simulations. (b) Damping parameter α as a function of the tip length l found from the $P(E)$ -fits to the $I(V_j)$ curves.

which reason the discussion of α has to remain on a qualitative basis at this point. Figure 4.4(b) displays the damping α as a function of the tip length l that we found from the fits. These large values reflect the intrinsically low quality common to antennas that are constructed for dissipating power into free space. Moreover, unlike real antennas that are capacitively coupled to their power feed, the STM tip in our case is in ohmic contact to the measurement circuit. This link favors power dissipation along the wires and results in the observed large damping. Figure 4.4(b) also compares the fitted damping for the two different tip holder geometries. For the large tip holder surface A_1 we find a strongly reduced damping compared to the small surface tip holder A_2 . This result reflects the ground plane's relevance as the antenna's "second half". The slight increase found in α for shorter tip lengths with the tip holder A_1 could originate from the discussed finite thickness of the antenna reducing the resonance quality.

5.3 Numerical Simulations of the Environmental Impedance

In a next step, we aim to corroborate and complement our knowledge on the electromagnetic properties of the STM geometry by means of *Finite Integral Method* (FIM) simulations using the CST Microwave Studio [132]. The simulations were performed in collaboration with Andreas Hardock from the Institute for Theoretical Electrical Engineering at the TU Hamburg-Harburg. To this end we create a simplified 3D model of the STM head geometry, of which cross sections are displayed in Fig. 5.5 (cf. Ch.3, Fig.3.2). In comparison to the real STM head geometry, we reduce the complex structure to the relevant parts in the junction vicinity, which is a necessary step for a successful simulation, as the wide spread of aspect ratios along the real geometry results in diverging simulation times. However, this reduction to the relevant structure could result in deviations between the real and simulated impedance $Z(\nu)$, in particular in the limit of lower frequencies where large geometric aspect ratios are of importance.

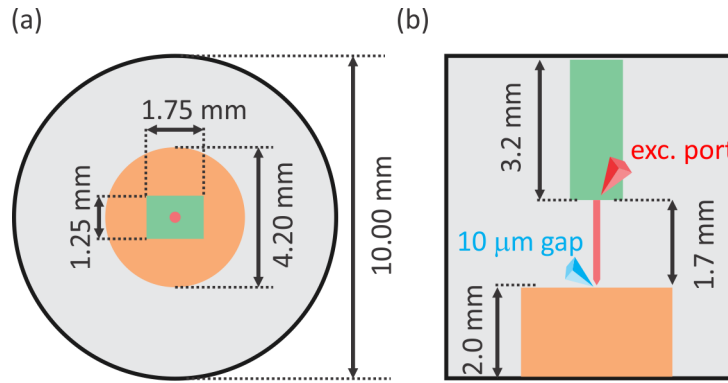


Figure 5.5 – (a) Top view of the geometric structure used for the FIM simulations. (b) Cross section of the same structure. The excitation port and the small gap between tip apex and sample surface are indicated. All relevant dimensions are labeled.

To probe the electromagnetic properties of this reduced structure, we apply an excitation pulse at the tip bottom and record the scattering spectrum of this excitation along the geometric structure as the scattering parameter $S_{11}(\nu)$. As a pulse, we use a Dirac-shape pulse in the time domain, which has an amplitude of $V = 1$ V. In order to simplify the analysis of $S_{11}(\nu)$, we neglected reflections from the enclosing structure. The impedance $Z(\nu)$ of the tip holder assembly can be directly calculated from the scattering parameter using the network microwave conversion technique [133]. For a one port network, this conversion is simply given by

$$Z(\nu) = Z(0) \frac{1 + S_{11}(\nu)}{1 - S_{11}(\nu)}, \quad (5.2)$$

where $Z(0)$ denotes the DC impedance of the structure.

Fig. 5.6(a) and (b) display the scattering parameter $S_{11}(\nu)$ as well as the converted impedance spectrum $Z(\nu)$, which result from the FIM simulation of a $l = 1.7$ mm long STM tip on the small area tip holder A_2 . They feature four resonances on the sampled frequency range, which

5.3. Numerical Simulations of the Environmental Impedance

are indicated by $\nu_{0,1,2}$ and ν_X . The frequency values of the $\nu_{0,1,2}$ modes constitute the typical eigenmode pattern of a $\lambda/4$ -monopole antenna, namely that the lowest eigenmode ν_0 has approximately half the frequency of the spacing of the higher modes $\nu_0 \approx 0.5(n_k - n_{k-1})$ and $k \geq 2$ (cf. Eq. 4.19). We can observe a similar eigenmode pattern in the voltage positions of the current resonances in experimental $I(V_J)$ -curves (cf. e.g. Fig. 5.2). However, there are distinct differences between the simulated impedance spectrum and our experimental results. First, we never observe a footprint of the $\nu_X \approx 25$ GHz mode in the experimental $I(V_J)$ curves (cf. Fig. 5.6(b) and 5.2). Since the corresponding current resonance would occur at voltages of around $50 \mu\text{eV}$ it could be masked by the much larger supercurrent peak occurring at similar voltages. Second, the amplitude of the eigenmodes $\nu_{0,1,2}$ rapidly decays to higher modes $n > 0$. When comparing to experimental $I(V_J)$ curves, e.g. Fig. 5.2, the current resonances also exhibit such a decay to higher modes. However, also the response of the Josephson junction to the environment decays as $1/\nu$ [37, 38]. For this reason it is difficult to unambiguously assign the decay in the current resonances to a decay of the resonance amplitudes in $Z(\nu)$. Our analysis of the experimental data based on $P(E)$ -theory using a transmission line impedance does not include such a decay, cf. Eq. 4.20 and Fig. 4.5(c). Therefore, our analysis could contain an error in the relative distribution of the spectral weight. On the one hand, a more precise treatment of $Z(\nu)$ is certainly desirable to reduce this error and will be part of future work. In particular, using numerically simulated impedance functions as an input parameter for $P(E)$ -theory could be of particular interest here. On the other hand, the known error in $Z(\nu)$ should not hamper a quantitative analysis of the Cooper pair tunneling curves in view of JSTM, which was indeed demonstrated by extracting the correct values of the Josephson critical current in Ch. 4, Sec. 4.6.

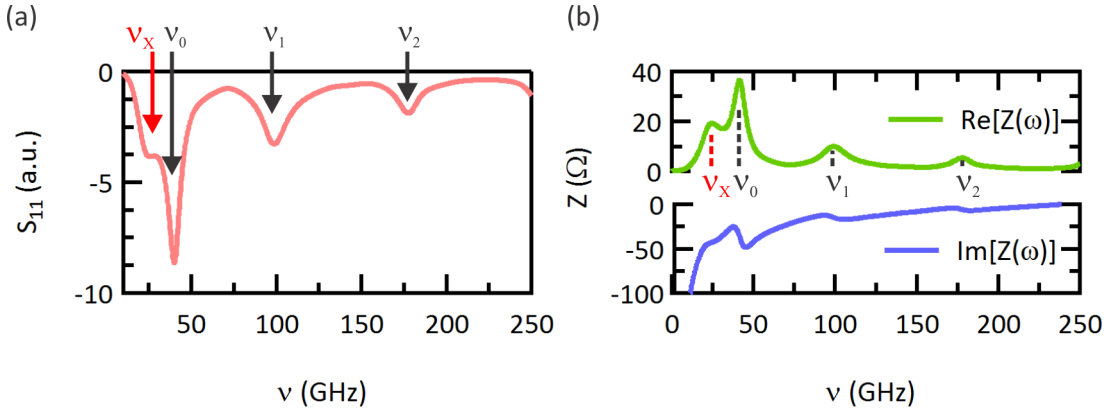


Figure 5.6 – (a) Scattering parameter $S_{11}(\nu)$ of the simulated geometry, as shown in Fig. 5.5 ($l = 1.7$ mm, A_2), with four indicated resonances, $\nu_{0,1,2}$ and ν_X , respectively. (b) Real- and imaginary part of the impedance $Z(\nu)$, as obtained from the simulated scattering parameter spectrum.

Analyzing the experimental Cooper pair tunneling characteristics using $P(E)$ -theory, as described in the previous section, we observed a strong dependence of the environmental impedance $Z(\nu)$ on the STM geometry. To reproduce this observation we simulate the electro-

dynamic properties of the corresponding simplified geometries, i.e. different tip lengths l and tip holder surfaces A , in the same fashion as before and determine the simulated impedance function $Z(\nu, l, A)$. From these impedance functions we extract the respective lowest eigenmode frequency ν_0 and plot them as a function of the tip length in Fig. 5.4(a). We find largely good agreement between these simulated values and the values determined from experimental $I(V_J)$ curves using $P(E)$ -theory, also concerning the effect of electrical lengthening [113, 114].

In the last step, we investigate the electric near field pattern of the resonance modes that can be found from the *FIM* simulations. Figure 5.7 displays the electric field pattern on a cross section of the simplified structure, focusing on the tip holder sample area. Shown are the absolute values of the electric field at the frequencies of all resonances $\nu_{0,1,2}$ and ν_X , that are found in the impedance spectrum (cf. Fig. 5.6(b)). For the eigenmodes $\nu_{0,1,2}$, these patterns are in great agreement with the simplified electric field pattern in Fig. 4.5(b), which we derived from a basic geometric impedance distribution analysis. We further find the field strength to be highest at the tip apex and, due to the confined geometry, we estimate the near field at the tip apex, i.e. in the tunnel junction, to be much larger than the field strength found from simulations¹. By reciprocity, the antenna is most susceptible to absorb radiation at this point, thereby corroborating the observed strong coupling to the Josephson junction (cf. Sec. 4.2)². In contrast to the tip eigenmodes, the field pattern of the mode ν_X appears like a resonance mode that is hosted by the enclosing surfaces between tip-holder and sample. It can also be seen that the antenna ground plane, i.e. the tip holder, shows enhanced field strength for every mode, which illustrates its relevance and the impact observed in our experiments (cf. Fig. 5.4(b)).

In conclusion, the presented simulation results on the electrodynamics properties of the STM head confirm and extend our results on $Z(\nu)$ that we obtained by means of $I(V_J)$ tunneling spectroscopy as well as from a simple geometric impedance analysis shown in Ch. 4. We conclude that the impedance of a typical STM geometry is strongly frequency-dependent and exhibits characteristic properties of a $\lambda/4$ -monopole antenna, such as a defined eigenmode spectrum with the $\lambda/4$ resonance as the lowest eigenmode. First, this result is of great interest for ourselves because it clearly characterizes the environment of the Josephson junction in our STM. Second, our results on the STM head impedance could provide useful information for other recently implemented STM setups that involve HF signals and operate in the time domain [131, 134, 135].

In the following section, we will discuss perspective applications for the combination of a resonator structure and a Josephson junction in an STM.

¹Even for the simplified geometry, the largely varying aspect ratios did not allow a detailed study of the field distribution in the tunnel junction in these first *FIM* simulations. However, with the present knowledge obtained granting a precise refinement of the simulated structure and mesh, the near field properties in the tunnel junction will be investigated in future simulations.

²The current amplitude at a given voltage V_J directly relates to the energy exchange probability at the corresponding energy $P(E = 2eV_J)$, which in our case is dominated by the tip holder assembly impedance.

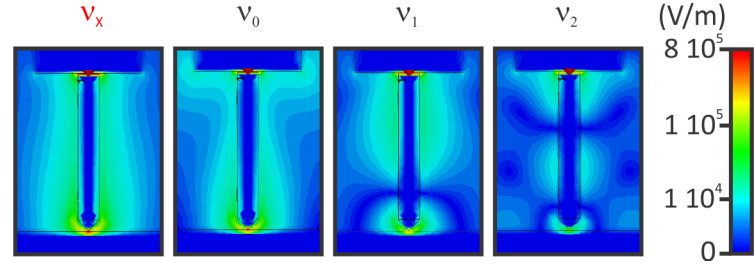


Figure 5.7 – Simulated electric field pattern for the three lowest tip eigenmodes $v_{0,1,2}$ as well as the additional geometrical mode v_x of a $l = 1.7$ mm long tip.

5.4 Features and Perspectives of the AC Josephson STM

In view of the resonator properties of the STM tip and the maximum electric field at the tip apex, we look again at the inelastic tunneling process of Cooper pairs in more detail: The energy $h\nu$ of the emitted photons can be directly tuned by the applied bias voltage V_J ($2eV_J = h\nu$). The tip eigenmode spectrum enhances the tunneling probability of Cooper pairs at specific eigenmode energies $h\nu_n$. This means that the tip eigenmode spectrum facilitates the creation of a photon field in the tunnel junction. Remarkably, while the tunneling process and the photon generation are localized in the nanoscale tunnel contact of the STM, the macroscopic resonator, i.e. the STM tip holder assembly, necessary to enhance the tunneling process, can be manipulated on the millimeter scale. In conjunction with the unity quantum yield of photon generation, these two different length scales should facilitate a high photon flux ϕ localized at the tunnel contact. This flux can be directly calculated from the resonant current peak amplitude, since the quantum efficiency of the photon generation process is unity, i.e. every inelastic Cooper pair tunneling process generates one photon of energy $h\nu = 2eV_J$. For a measurement with an $l = 0.7 \pm 0.1$ mm long tip on the large tip holder surface A_1 shown in Fig. 5.8, we find a peak amplitude for the v_0 mode of $I_M \approx 350$ pA at a tunneling conductance of $G_N = 0.12 G_0$. This value directly translates into a photon number per second of $n_p \approx 0.9 \times 10^9$ s $^{-1}$. If we assume, in a simplified picture, that the photons are emitted in a cube of edge length l , we can estimate the approximate number of photons crossing a surface plane of this cube $\phi = n_p / (6 \times l^2)$. However, it is currently an unresolved question whether the photons are emitted during the tunneling process through the atomic scale tunnel contact, $l \approx 100$, pm, or after tunneling within the coherence length of the superconductor, $l \approx 10^1$ nm [93]. Still, from these values we can estimate upper and lower boundaries of the photon flux to $10^{20} \leq \phi \leq 10^{24}$ cm $^{-2}$ s $^{-1}$. These flux values are well within the range of flux applied in conventional laser spectroscopy methods, hence we can underline the potential of the resonator Josephson junction combination in our STM to be employed as a high-frequency source for spectroscopic applications.

However, it should also be noted that a successful application of the AC Josephson STM for spectrometry does actually not require a resonator for the creation of an additional photon field inside the tunnel junction that could interact with nanoscale samples. In principle, it only

requires the sensitivity of the Josephson junction to its frequency-dependent environment $Z(\nu)$. In detail, following $P(E)$ -theory (cf. Ch.4), any electromagnetic transition that provides a possibility for Cooper pairs to exchange the energy portion $h\nu = 2eV_J$ alters the total environmental impedance spectrum $Z(\nu)$. Accordingly, also a nanoscale sample inside the tunnel contact that exhibits such an electromagnetic transition, e.g. the spin-flip process of a magnetic moment, should alter the measured Cooper pair tunneling current at the corresponding voltage $V_J = h\nu/(2e)$. Hence, the AC Josephson STM should be capable of probing a variety of nano-scale samples, the choice of which is only limited by the spectrometer's spectral range and energy resolution, i.e. spectroscopic line width.

The accessible frequency range is limited by the superconducting order parameter Δ of the electrode material, since the photon generating process involves tunneling Cooper pairs. For our current setup using vanadium as the electrode material, the maximum frequency of approximately 250 GHz is limited by the maximum value of the tip order parameter $\Delta \approx 500 \mu\text{eV}$. Still, this range could be extended into the THz range by choosing materials with larger Δ , such as MgB_2 [136]. However, in that case the junction capacitance and wire resistance have to be adapted to the higher frequency range. The line width of the AC Josephson STM is predominantly limited by the voltage noise \bar{u} due to thermal charge fluctuations on the shunting capacitance, which effectively broadens all spectral features (cf. Ch. 4, Sec. 4.2.2). Hence, the lowest temperatures are necessary to minimize the line width. For our current setup we estimate voltage fluctuations of about $\sqrt{\bar{u}^2} \leq 12 \mu\text{eV}$ [35]. Inserting a larger capacitive shunt will strongly decrease the line width, but in turn also decrease the junction sensitivity to large frequencies, so that the right shunt needs to be chosen in view of the perspective application.

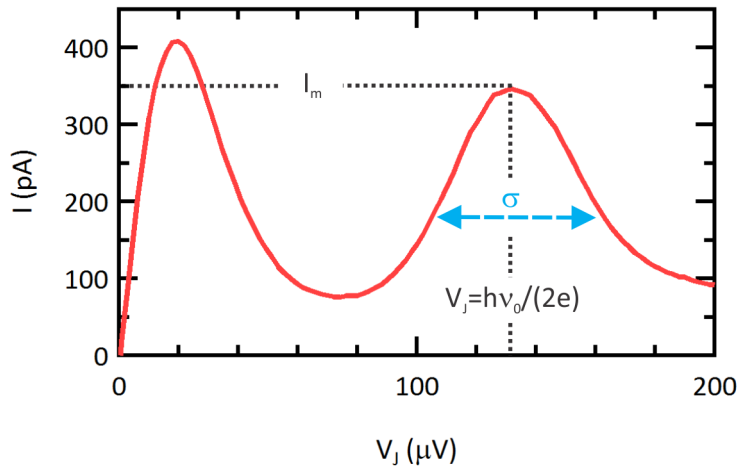


Figure 5.8 – Determination of both the maximum resonance current I_M and the $FWHM$ σ of the lowest eigenmode ν_0 for a measurement with an $l = 0.7$ mm long STM tip on top of the tip holder A_1 .

Another interesting aspect is the lifetime of an excitation in the resonator, i.e. the tip antenna,

after an inelastic Cooper pair tunneling event. For lifetimes larger than the average time between two subsequent inelastic Cooper pair tunneling events, the excited resonator could allow us to study nonlinear Cooper pair photon interactions predicted by theory [106]. From the current resonance in Fig. 5.8 we can make a simple estimate on this lifetime τ_1 , which can be approximated via the oscillation period of an eigenmode along the tip antenna, \bar{t} , and the quality factor of the corresponding eigenmode $\tau_1 = \bar{t} \times Q$. Here, the quality factor denotes the number of oscillation periods for a resonator excitation before the resonator relaxes back into its ground state. We can calculate the oscillation period as the time that an excitation needs to travel from the tip apex to the tip-holder edge and back to the apex $\bar{t} = 2(l + d/2)/c_0$. For the $l = 0.7$ mm long tip on the large tip-holder of diameter $d = 3.2$ mm used for the experiment in Fig. 5.8 we find $\bar{t} \approx 44$ ps. Furthermore, we can simply approximate an upper limit of the resonator quality from the *FWHM* value σ and voltage position V_J of the current peak to $Q = V_J/\sigma \approx 3$. These values result in an average excitation lifetime for the resonator of $\tau_1 \approx 0.13$ ns. From the amplitude of the current resonance in Fig. 5.8 we can also calculate the average time between two subsequent resonator excitations as the average time between two inelastic Cooper pair tunneling events, and we find $\tau_2 = 2e/I_S \approx 0.9$ ns. Remarkably, the average excitation lifetime of the resonator, τ_1 , is smaller but still on the same order of magnitude as the average time between two excitation events. Hence, experiments on nonlinear Cooper pair photon interactions [106] are in reach and, for instance, could be realized by tuning the geometry of the tip antenna in order to increase the eigenmode quality (cf. Ch. 7).

5.5 Conclusion

To conclude, in this chapter we investigated the electrodynamic properties of the Josephson junction environment, $Z(\nu)$. Combining voltage-biased experiments on the Josephson junction in our STM with FIM Simulations on the electrodynamic properties of the STM head, we find that the impedance $Z(\nu)$ of a typical STM geometry is strongly frequency-dependent and that it is similar to the impedance of a $\lambda/4$ monopole antenna. With the sensitivity to HF-signals we demonstrate a first realization of the AC Josephson STM spectrometer and show that spectrometry of HF signals is, in principle, possible with the microscopic Josephson junction in an STM, a concept that has only, to date, been successfully demonstrated in planar junction geometries [22, 23, 137, 138]. The spectral range of this spectrometer is only limited to larger frequencies by the superconducting order parameter Δ , whereas the line width of the spectrometer is dominated by thermal voltage fluctuations on the junction capacitance.

6 Phase Dynamics of an Atomic Scale Josephson Junction

6.1 Introduction

In Chapter 4, experimental results indicated that for larger values of the tunneling conductance $G_N \approx G_0$ the tunneling current through the Josephson junction in our STM is carried by an increasing amount of coherent Cooper pair tunneling, as opposed to the sequential tunneling of Cooper pairs in the DCB regime. The observation of coherent Cooper pair tunneling is associated with a bound state of the junction phase inside a washboard potential minimum, which facilitates the observation of the DC Josephson effect. In fact, we are able to observe the DC Josephson effect when we apply a bias current to the Josephson junction in our STM as, for example, shown in Fig. 6.1(a) and (b). As we will see later, this even works for quite a large range of tunneling conductance values $G_N < G_0$. Figure 6.1(b) also shows that in our experiment the $I(V_J)$ curves are strongly hysteretic and, even more remarkably, that the current-biased and voltage-biased $I(V_J)$ curves perfectly match and only deviate in the regions of negative differential conductance. By being able to access features of both sequential and coherent

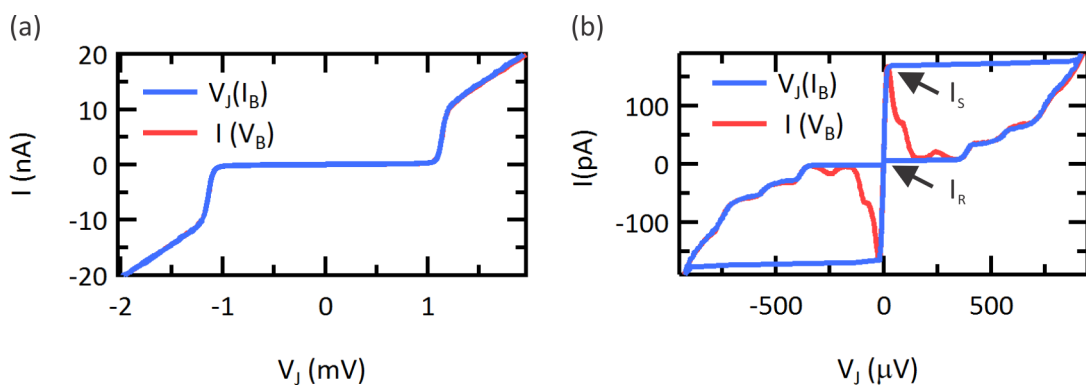


Figure 6.1 – (a) Large scale comparison of the $I(V_J)$ curves for voltage-biased and current-biased experiments. (b) Magnification of the in-gap region that displays the sequential Cooper pair tunneling characteristics discussed in Ch. 4 for the voltage-biased experiment as well as the characteristic hysteretic $I(V_J)$ characteristics for the current-biased experiment.

Chapter 6. Phase Dynamics of an Atomic Scale Josephson Junction

tunneling in one spectrum as well as the existence of the DC Josephson effect in the current-biased $I(V_J)$ curves tells us that our Josephson junction is operated in a *quantum mechanical* regime (cf. Ch. 2, Sec. 2.5). In this regime, $E_J \approx E_C$, neither the junction phase ϕ nor the charge q are perfectly defined quantum numbers as opposed to the *classical limits* $E_J \gg E_C$ or $E_J \ll E_C$; both exhibit a certain uncertainty σ . For this reason, in the regime $E_J \leq E_C$ which is relevant to this chapter, the junction cannot simply be represented by a particle in a washboard potential¹ but rather by a wavefunction $\bar{\Psi}(\phi)$, as illustrated in Fig. 6.2 [139]. This purely quantum-mechanical property of ϕ and q also manifests itself in the experimental $I(V_J)$ characteristics of the Josephson junction, in which it strongly alters the $I(V_J)$ curves in comparison to the classical limits. For instance, the tunneling of the phase between two adjacent minima in the washboard potential – similar to the tunnel effect discussed in Ch. 2, Sec. 2.2.1 – can drastically reduce the maximum observable DC Josephson current [31, 40]. To

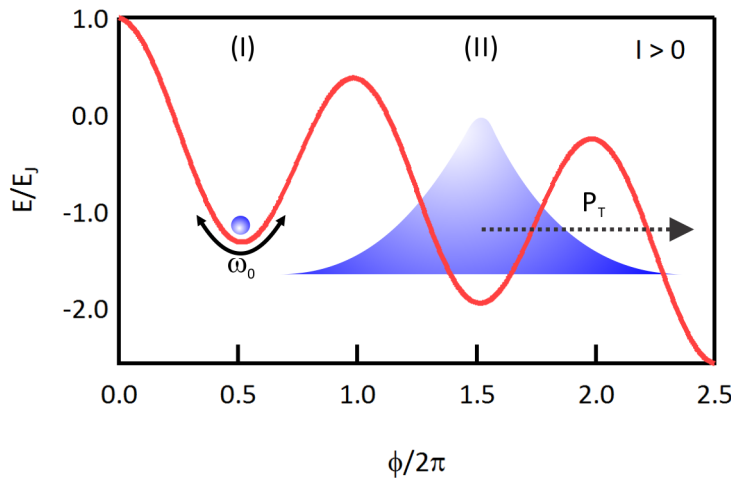


Figure 6.2 – (I) Classical representation of the junction phase as a particle in a washboard potential, valid for $E_J \gg E_C$. (II) Quantum mechanical representation of the junction phase as the wavefunction $\bar{\Psi}(\phi)$ for the regime $E_J \approx E_C$. Possible phase tunneling P_T to the adjacent potential minimum is indicated by the dashed arrow.

fully characterize the Josephson junction in our STM and clarify its properties it is necessary to investigate this quantum-mechanical character of phase and charge. Although these quantum-mechanical Josephson junctions attracted considerable experimental and theoretical efforts in the years around 1990, questions on dissipation mechanisms and the transition from sequential to coherent Cooper pair tunneling remained open, mainly due to the experimental limitation that the Josephson coupling energy can not be easily tuned in experiments on planar junction geometries [41, 140, 141, 142]. Moreover, varying the ratio of E_J versus E_C is also of large interest in today's science, especially in the context of *Hamiltonian by design* for phase qubits [12]. In STM experiments the ratio E_J versus E_C can be readily tuned by varying the tip-sample distance and for this reason, STM can serve as an ideal means for addressing

¹This classical analogue represents the case $E_J \gg E_C$ in which the phase is perfectly localized.

these fundamental problems of superconducting tunneling.

Within this chapter we investigate the quantum-mechanical character of the junction as well as the energy dissipation of the junction phase $\phi(t)$. To this end, we perform experiments on current-biased and voltage-biased Josephson junctions, whereby this combined approach provides total control of the parameter space. The analysis of the experimental data is partly based on the $P(E)$ -theory introduced in Ch. 4. The theoretical framework necessary for analyzing $I(V_J)$ curves from current-biased experiments as well as $\dot{\phi}$ will be presented in this chapter.

6.2 Defining the Quantum-Mechanical Regime

Figure 6.1 shows that both the coherent as well as the sequential Cooper pair tunneling can be observed when the capacitive charging energy E_C is comparable to the Josephson coupling energy E_J (cf. Ch. 2, Sec. 2.5). However, the question still remains open for which range of E_C versus E_J this manifestation of the quantum-mechanical nature of ϕ and q can be expected. In other words, for which values of E_J versus E_C is the junction phase sufficiently localized in a potential well so that the coherent tunneling of Cooper pairs can still be observed. We can determine the boundaries of this regime when we investigate the extent of the wavefunction $\bar{\Psi}(\phi)$ in the washboard potential $U(\phi)$ as a function of E_J versus E_C . To this end we write again the Hamiltonian of the Josephson junction, using $\bar{\lambda} = E_J/(4E_C)$, (cf. Ch. 2, Eq. 2.35)²

$$H' = n^2 - \bar{\lambda} \cos(\phi). \quad (6.1)$$

This Hamiltonian is equivalent to the Hamiltonian of an electron which experiences a periodic potential. In analogy to the Bloch functions for an electron in a crystal lattice (see e.g. Ref. [143]), we can introduce a wavefunction

$$\bar{\Psi}(\phi) = e^{in\phi}. \quad (6.2)$$

From the derivative of $\bar{\Psi}(\phi)$ with respect to the phase,

$$\frac{\partial}{\partial \phi} \bar{\Psi}(\phi) = in \bar{\Psi}(\phi), \quad (6.3)$$

follows $n = -i\partial/\partial\phi$, which allows one to simplify the modified Hamiltonian in Eq. 6.1 to

$$H' = -\frac{\partial^2}{\partial \phi^2} - \bar{\lambda} \cos(\phi). \quad (6.4)$$

In this formulation, the Hamiltonian corresponds to the time-independent Schrödinger equation, which can be evaluated in ϕ space, $H'\bar{\Psi}(\phi) = \epsilon\bar{\Psi}(\phi)$ and $\epsilon = E/(4E_C)$. However, it cannot be solved analytically due to the nonlinear cosine potential and thus it requires further means

²A similar approach for approximating this regime is given in Ref. [139].

Chapter 6. Phase Dynamics of an Atomic Scale Josephson Junction

of simplification. Assuming the phase to be sufficiently localized in the center of the potential minimum we can expand the cosine term up to second order, giving

$$\cos(\phi) = 1 - \frac{1}{2}\phi^2 + O(\phi^3). \quad (6.5)$$

This simplification yields a harmonic potential so that the resulting Schrödinger equation,

$$H'\bar{\Psi}(\phi) = \left(-\frac{\partial^2}{\partial\phi^2} + \frac{\bar{\lambda}}{2}\phi^2\right)\bar{\Psi}(\phi) = \epsilon\bar{\Psi}(\phi), \quad (6.6)$$

corresponds to the Schrödinger equation of a harmonic oscillator [144]. This equation can be solved analytically and its eigenfunctions, which represent the junction phase ϕ of the Josephson junction in the phase space, are the Hermite functions

$$\bar{\Psi}_n(x) = \left(\frac{1}{\pi}\sqrt{\frac{\bar{\lambda}}{2}}\right)^{1/4} \frac{1}{\sqrt{2^n n!}} H_n(x) e^{-\frac{x^2}{2}}, \quad (6.7)$$

where $x = \sqrt[4]{\bar{\lambda}/2}\phi$ and $H_n(x)$ denotes the Hermite polynomial [145]. The first two eigenfunctions of the junction phase are shown in Fig. 6.3(a) for $E_J = E_C$ inside the washboard potential. The eigenenergies correspond to the harmonic oscillator eigenenergies,

$$\epsilon_n = \sqrt{2\bar{\lambda}}(n + 1/2), E_n = \sqrt{8E_J E_C}(n + \frac{1}{2}), \quad (6.8)$$

whereas the eigenenergy spectrum also reveals one of the major differences between the quantum-mechanical and classical description; namely, that the junction phase does not “sit” at the bottom of the potential as the classical particle does, but is elevated to a finite energy of the lowest eigenstate, the zero point energy $E_0 = \sqrt{2E_J E_C}$.

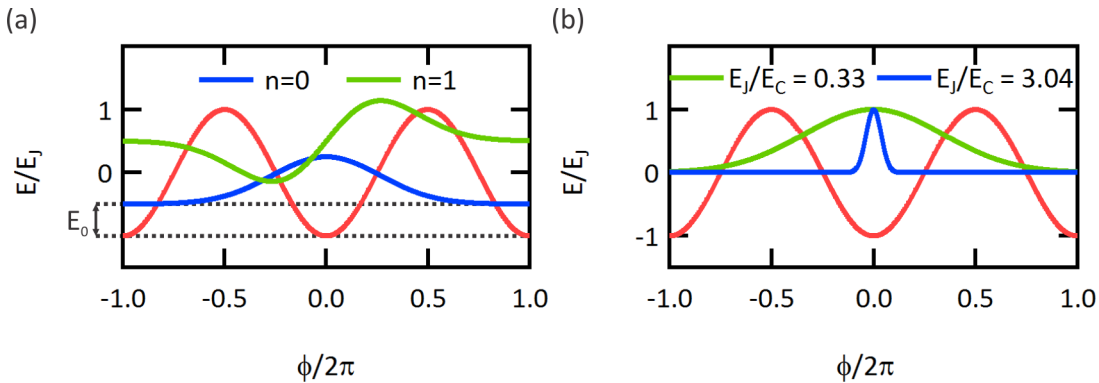


Figure 6.3 – (a) Calculated first two eigenfunctions $n = 0, 1$ of the junction phase for $E_J = E_C$. (b) Calculated $n = 0$ eigenfunction for different values of E_J/E_C , as indicated.

To determine the localization of the junction phase inside the potential, we investigate the width of the eigenfunction in the phase representation. To this end, we calculate the standard

deviation σ_ϕ of the $n = 0$ eigenfunction, assuming that the junction is not in an excited state. For this eigenfunction we find

$$\overline{\Psi}_0(x) = e^{-\frac{x^2}{2}} \rightarrow \overline{\Psi}_0(\phi) = e^{\sqrt{\frac{\lambda}{8}}\phi^2} = e^{\frac{-\phi^2}{\sigma_\phi^2}} \rightarrow \sigma_\phi = \sqrt[4]{\frac{32E_C}{E_J}}. \quad (6.9)$$

A sufficient localization of the phase within one potential minimum requires the condition $\sigma_\phi \leq \pi$. Hence, we are now able to define the lower limit of $\bar{\lambda}$ until which the phase is sufficiently localized, giving

$$\frac{E_J}{E_C} \geq \frac{32}{\pi^4}. \quad (6.10)$$

The standard deviation for the junction charge directly follows from the commutator relation between charge and phase (cf. Ch. 2, Sec. 2.5), giving $\sigma_\phi = \sqrt[4]{E_J/32E_C}$. Figure 6.3(b) displays the calculated $n = 0$ eigenfunction inside the washboard potential for these two values of E_J versus E_C which define the upper and lower boundaries of the range in which quantum-mechanical phenomena should effect the properties of the Josephson junction.

If we put in a typical capacitance of the tunnel junction in our STM, $C_J \approx 2.5$ fF (cf. Ch. 4), we find a limiting value to smaller numbers for the Josephson coupling energy of $E_J \approx 16 \mu\text{eV}$. Comparing this value with the values given in Fig. 4.1 in Ch. 4, we find that the phase should be sufficiently localized inside a potential minimum for tunneling conductance values exceeding $G_N/G_0 > 0.1$. This value is well within the tunneling conductance range accessible to our experiment. From the same figure we also find that the upper limit of the quantum-mechanical regime, $E_J/E_C \approx 3$, is well above the quantum of conductance, $G_N/G_0 = 1$, and exceeds the maximum value found in experiments $E_J/E_C \approx 1.63$.

Nevertheless, the quantum-mechanical regime is clearly accessible for our experiment and we should be able to observe footprints of this regime in the experimental $I(V_J)$ curves for $G_N/G_0 \geq 0.1$. As presented in Ch. 4, Sec. 4.5 we could already observe first indications of this quantum-mechanical regime when analyzing the voltage-biased $I(V_J)$ curves in the limit of $G_N \approx G_0$.

6.3 Theoretical Considerations

Within the last section, we showed, in a simple approximation, that for a particular range of the tunneling conductance accessible to our experiment the Josephson junction will be in a quantum-mechanical state in which neither its phase or charge are perfectly defined. To investigate this state we perform voltage-biased and current-biased experiments on the Josephson junction. The theoretical framework for analyzing the sequential tunneling characteristics of voltage-biased experiments has already been presented in Ch. 4. This section will focus on presenting theory, which describes the bound state of the junction in a washboard potential minimum at a given junction phase $\phi(t)$ as well as the temporal evolution $\dot{\phi}(t)$. In particular,

the theory focuses on two experimental quantities, which are the switching current I_S and the retrapping current I_R , as they were introduced in Ch. 2, Sec. 2.3 [59, 60, 146]. These quantities provide direct access to the quantum behavior of the phase and the dissipative interaction of the junction phase with the environment and, additionally, they are easy to determine experimentally.

6.3.1 Retrapping into the Zero Voltage State

Figure 6.1(b) shows that the $I(V_J)$ curves of the Josephson junction in our STM are strongly hysteretic. Such characteristics are typical for junctions in the limit $E_J \gg E_C$ whose phase dynamics can be treated classically, but it is not *a priori* to be expected from junctions in which E_J is comparable to E_C . Despite this, in the last section, we could approximate a range of E_J versus E_C values, in which the phase is still sufficiently localized in the washboard potential minima and we found that this range of tunneling resistance values is accessible to our experiment. Therefore, we present theory for analyzing the retrapping characteristics of the Josephson junction that treats the phase as a classical variable – an approach that is sufficient to explain our experimental observation as the later analysis will reveal (cf. Sec. 6.7).

Starting from the very first formulation of the Josephson effect, it is possible to derive a differential equation for the temporal evolution of the junction phase, as was introduced in Ch. 2, Sec. 2.3. This equation, which can be solved by numerical means, facilitates the investigation of the temporal evolution of the phase $\phi(t)$ as the movement of the phase, represented by a particle, through the washboard potential. While the external current bias I_B tilts the washboard potential and serves as a driving force, the particle also experiences friction during its movement through the potential landscape. The strength of this friction depends on various parameters, such as the junction capacitance C_J or the tunneling resistance R_N [59, 60] and strongly influences the dynamics of $\phi(t)$. Considering the $I(V_J)$ curve of a current-biased measurement displayed in Fig. 4.1 (b), for instance, we clearly observe a strong hysteresis in the tunneling characteristics and that the retrapping into the zero voltage state occurs close to zero current bias. According to the theoretical introduction (cf. Ch. 2, Sec. 2.3), the existence of a hysteresis loop indicates underdamped junction dynamics, $Q = R_{DC}C_J \times \sqrt{2eI_0/(C_J\hbar)} \gg 1$. Inserting typical values for our experiment in the tunnel regime ($I_0 \approx 5$ nA, $R_N \approx 250$ k Ω and $C_J \approx 2.5$ fF, as given in Ch. 4) we indeed find $Q \approx 30$ and we can conclude that, for standard STM experiments, the junction dynamics are highly underdamped³.

The retrapping into the zero voltage state occurs when the driving energy from the current bias cancels out with the energy dissipated due to friction and we again write the condition

³In principle, underdamped dynamics are common to small area Josephson tunnel junctions, since the capacitance of the contact strongly decreases with the junction area. However, it is possible to create overdamped dynamics by means of advanced circuitry. Here, the junction dynamics are effectively decoupled from the environment and dissipative elements, such as resistors, are introduced to enhance the damping. This approach is in particular interesting in order to reduce phase diffusion in small area Josephson junctions and very descriptive examples of this approach can be found in Refs. [61, 62].

for retrapping [59, 60]:

$$\int_{-\pi}^{\pi} d\phi \frac{I_R}{I_0} = \frac{1}{\omega_0^2 \tau} \int_{-\pi}^{\pi} d\phi \dot{\phi}(t). \quad (6.11)$$

For a junction that is shunted with an ohmic resistor this equation can be readily solved and yields the simplest form of the retrapping current [59],

$$I_R = \frac{4}{\pi} \frac{I_0}{Q}, \quad (6.12)$$

which clearly displays the strong dependence of the retrapping current on the energy dissipation of the junction phase, as expressed by the quality factor Q . However, many experiments on Josephson *tunnel* junctions do not comprise an ohmic shunt but instead a voltage-dependent quasiparticle resistance shunt $R_{QP}(V_J)$. Here, the $I(V_J)$ characteristics deviate from the ohmic behavior for $V_J \leq 2\Delta$ and the current is carried by quasiparticle excitations, as is shown in Fig. 6.4 (cf. Ch. 2, Sec. 2.1). Given an experiment at zero temperature and a perfect superconducting BCS gap, the differential resistance $\Delta V_J / \Delta I_{QP}$ will diverge for voltages smaller than twice the superconducting gap, $V_J \leq 2\Delta$. Accordingly, the quasiparticle resistance R_{QP} will strongly exceed the ohmic resistance R_{DC} . As a consequence, the dissipation into the environment is inhibited and the retrapping of the junction into the bound state occurs at much smaller values of the current bias in comparison to an ohmic shunt [146].

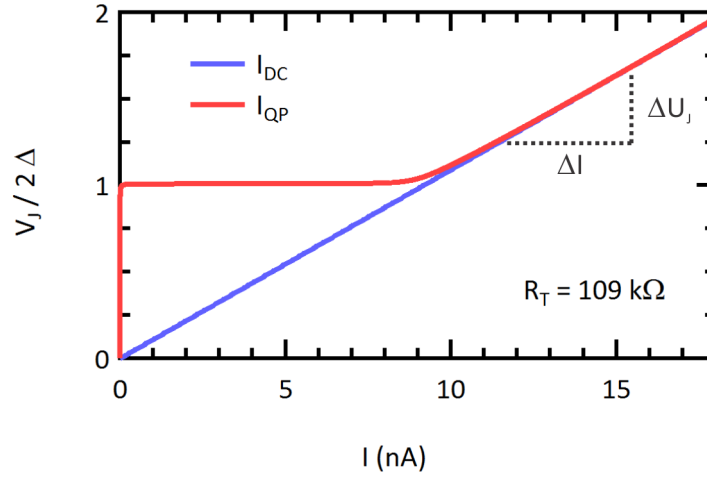


Figure 6.4 – Comparison of a calculated ohmic current $I_{DC}(V_J)$ and a calculated quasiparticle current $I_{QP}(V_J)$ at a tunneling resistance of $R_T = 109 \text{ k}\Omega$.

Calculating the retrapping current for a tunnel junction, therefore, requires one to consider all possible dissipative channels that constitute an effective in-gap resistance R_{eff} . Such a calculation was first performed by Chen, Fisher and Leggett (CFL) [147]. The authors incorporated all possible voltage-dependent quasiparticle and pair transfer processes, as given in Ref. [56], into a quantum-Langevin equation that describes the dissipative time

Chapter 6. Phase Dynamics of an Atomic Scale Josephson Junction

evolution of the phase [148, 147]. Assuming zero temperature, the authors employed Eq. 6.11 to calculate an expression for the retrapping current, giving [147]

$$I_{R,T=0} = \frac{8\Delta^2}{e\hbar\omega_0 R_N} e^{-\frac{2\pi\Delta}{\hbar\omega_0}}. \quad (6.13)$$

This formulation of the retrapping current represents its ultimate limit that can be reached if dissipative in-gap quasiparticle currents do not exist. Hence, the particle moving down the washboard potential can only dissipate energy via breaking up Cooper pairs at $V_J = 2\Delta$ and the junction will therefore retrap into the potential minimum at smallest current bias values. For the same reason, it is experimentally very challenging to reach this minimum retrapping current as we will also see in the later analysis (cf. Sec. 6.7). In most experiments, lifetime effects of Cooper pairs, Andreev reflections or finite temperatures induce in-gap quasiparticle currents at $V_J < 2\Delta$ that increase dissipation and, thereby, increase the current at which the junction retraps.

In an initial experimental work, Kirtley *et al.* addressed the influence of thermally excited quasiparticles on the retrapping current [140]. The starting point of their analysis, which is based on the CFL model, is an effective in-gap resistance for $V_J < 2\Delta$

$$\frac{1}{R_{\text{eff}}} = \frac{1}{R_{\text{QP}}} + \frac{1}{R_{\text{QPP}}} \cos(\phi), \quad (6.14)$$

which includes the quasiparticle resistance R_{QP} as well as the quasiparticle-pair interference resistance R_{QPP} . Employing Eq. 6.11 the authors first simplified the equation for the retrapping current to

$$I_R^{\text{CFL}} = \frac{4I_0}{\pi\omega_0 C_J} \frac{1}{R_{\text{eff}}} = \frac{4I_0}{\pi\omega_0 C_J} \left[\frac{1}{R_{\text{QP}}} + \frac{1}{3R_{\text{QPP}}} \right]. \quad (6.15)$$

Secondly, assuming a Boltzmann-type reduction of the quasiparticle resistance inside the gap, $1/R_{\text{QP}} \propto \exp(-\Delta/k_B T)$ and the temperature such that $\omega_0 \ll k_B T \ll \Delta$ – this energy window corresponds typically to a temperature of a few Kelvin – the authors derived the following expression for the retrapping current

$$I_R^{\text{CFL}} = \frac{8I_0}{3Q} \frac{\Delta}{k_B T} e^{-\Delta/k_B T}. \quad (6.16)$$

The two presented, yet quite different, examples for the relation between the dissipation and the retrapping current already illustrate that the energy dissipation strongly depends on the type and strength of the in-gap quasiparticle currents. To obtain a proper description for our experiment, we compare the thermal energy and the energy of the Josephson plasma mode $\hbar\omega_0$ with values from Ch. 4 in Fig. 6.5(a). It is apparent that, for our experimental conditions, the thermal energy, $k_B T$, is much smaller than the energy of the plasma mode for all values of

the tunneling conductance, for which reason Kirtley's model for calculating I_R is not applicable in our case.

Moreover, a typical experimental quasiparticle excitation spectrum, as shown in Fig. 6.5(b), reveals broadened quasiparticle excitation peaks as well as a finite conductivity inside the superconducting gap, i.e. the presence of dissipative in-gap quasiparticle currents. In our case, both phenomena result from the lifetime effects of Cooper pairs discussed in Ch. 2, Sec. 2.2.4. We also find that both the sample gap, $\Delta_1 \approx 800 \mu\text{eV}$, and the tip gap, $\Delta_2 \approx 300 \mu\text{eV}$, are much larger than $k_B T$ and $\hbar\omega_0$. Although in our experiment the influence of the temperature is negligible, the existence of dissipative in-gap currents will make it impossible to employ the zero temperature limit of the CFL theory (cf. Eq. 6.13) in order to describe the retrapping current in our experiment.

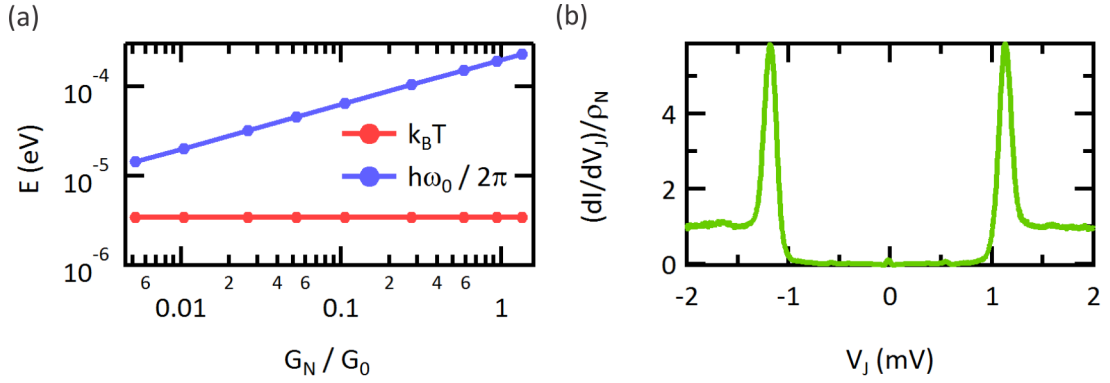


Figure 6.5 – (a) Comparison of Josephson plasma energy (values taken from Ch. 4) and thermal energy as a function of the normalized tunneling conductance. (b) Experimental quasiparticle excitation spectrum measured at $G_N = 0.11 G_0$ and $T = 15 \text{ mK}$.

Hence, we have to derive an appropriate description of the sub-gap dissipation that accounts for the in-gap quasiparticle currents induced by lifetime effects of Cooper pairs. To this end, we start with the Dynes equation in order to model the dissipative quasiparticle current through our tunnel junction according to

$$I_{QP}(V_J) = \frac{1}{eR_N} \int_0^{V_J} \rho_t(E-V) \rho_s(E) dE, \quad (6.17)$$

$$\rho_i(E) = \Re \left[\frac{E - i\Gamma_i}{\sqrt{(E - i\Gamma_i)^2 - \Delta_i^2}} \right] \quad (6.18)$$

(cf. Ch. 2, Sec. 2.2.4). Here, ρ_t and ρ_s denote the superconducting density of states for tip and sample, respectively. We are interested in the in-gap quasiparticle resistance $R_{QP} = V_J / I_{QP}$ for $V_J \ll \Delta_1 + \Delta_2$ which allows us to simplify Eq. 6.17 further on. To this end, we expand Eq. 6.18

around $E = 0$ using the relations $\epsilon = E/\Delta$ and $\gamma = \Gamma/\Delta$:

$$\rho_i(E) = \frac{\gamma_i}{\sqrt{1 + \gamma_i^2}} + \frac{3\epsilon_i^2 \gamma_i}{2(1 + \gamma_i^2)^{5/2}} + 0(\epsilon_i^3). \quad (6.19)$$

If we consider only the zero order term in ϵ we can directly evaluate the integral in Eq. 6.17. This step yields the expression for the quasiparticle tunneling current inside the superconducting gap, $V_J \ll \Delta_1 + \Delta_2$,

$$I_{\text{QP}}(V_J) \approx \frac{V_J}{R_N} \frac{\gamma_1 \gamma_2}{\sqrt{(1 + \gamma_1^2)(1 + \gamma_2^2)}}, \quad (6.20)$$

from which we readily obtain the quasiparticle resistance:

$$\frac{1}{R_{\text{QP}}} = \frac{\gamma_1 \gamma_2}{\sqrt{(1 + \gamma_1^2)(1 + \gamma_2^2)}} \frac{1}{R_N}. \quad (6.21)$$

Using Eq. 6.15 for the retrapping current, as derived by Kirtley *et al.* [140], we can calculate the retrapping current in the zero temperature approximation for a lifetime broadened superconducting density of states using

$$I_R = \frac{4}{\pi} \frac{I_0}{Q} \frac{\gamma_1 \gamma_2}{\sqrt{(1 + \gamma_1^2)(1 + \gamma_2^2)}}. \quad (6.22)$$

For the derivation of this expression we neglected the R_{QPP} term in Eq. 6.15 for the simple reason that we estimate the gap filling due to Cooper pair lifetime effects to be relatively strong in comparison to gap filling effects by Andreev reflections in the tunneling regime $G_N \ll G_0$.

6.3.2 Stability of the Zero Voltage State

The previous section treated the time evolution of the phase $\dot{\phi} \neq 0$ in a classical manner by investigating the dissipative motion of the phase through the washboard potential. The classical treatment was possible since the localization of the phase – represented by the wavefunction $\bar{\Psi}_0(\phi) = \exp(\frac{-\phi^2}{\sigma_\phi^2})$ – inside the potential minimum was assumed to be sufficiently large. However, $\bar{\Psi}_0(\phi)$ is still of finite width σ_ϕ and, therefore, tunneling processes to the adjacent minimum are in principle also possible, as illustrated in Fig. 6.6 (cf. Ch. 2, Sec. 2.2.1). On the one hand, this tunneling strongly reduces the amplitude of the DC Josephson current to values $I_S \ll I_0$. On the other hand, for small bias currents $I \leq I_S$ tunneling to adjacent minima results in a non-average $\dot{\phi}(t)$, such that the DC Josephson effects occurs at $V_J \neq 0$. In this situation, the DC Josephson current exhibits a finite slope $R_0 = V_J/I$ for $I \leq I_S$, as is also apparent in the exemplary $I(V_J)$ curve shown in Fig. 6.1(b) [31, 41, 139]. Hence, in comparison to the dynamics of $\phi(t)$, the stability of the zero voltage state at constant phase is much more effected by the quantum-mechanical nature of $\phi(t)$ and q . For this reason, this section focuses

on a quantum-mechanical description of the zero voltage state as well as the influence of quantum mechanics on the measurement quantities.

The finite slope in the coherent Cooper pair tunneling current can be explained on the basis of Fig. 6.6(a): If the washboard potential is slightly tilted by an applied bias current the barrier height \tilde{U} in the downhill direction is reduced, $\tilde{U}_- = 2E_J - \hbar\pi I_0/2e$, whereas it is increased in the uphill direction, $\tilde{U}_+ = 2E_J + \hbar\pi I_0/2e$ [139]. Hence, the probability for tunneling downwards \overrightarrow{P}_T is larger than for tunneling upwards \overleftarrow{P}_T , which results in a net rate of tunneling with a probability $\Delta P = \overrightarrow{P}_T - \overleftarrow{P}_T > 0$. Provided that damping of the junction is large enough, the junction phase will relax down into the lowest energy level of the adjacent minimum and remain in the bound state. Still, these phase slips correspond to a small, albeit non-zero, $\dot{\phi}(t)$, such that a small voltage drop V_J occurs across the junction. Assuming a sufficient localization of the phase inside the potential and a bias current $I \ll I_0$, the resistance R_0 resulting from these quantum-mechanical phase slips can be evaluated [40, 108, 139]

$$R_0 = \frac{V_J}{I} = \frac{\hbar}{2e} \frac{1}{I_0} \frac{d\phi}{dt} \approx \frac{\hbar}{2e} \frac{1}{I_0} (\overleftarrow{P}_T - \overrightarrow{P}_T), \quad (6.23)$$

$$\overrightarrow{P}_T = \frac{\omega_0}{2\pi} \chi^4 \sqrt{\frac{\tilde{U}}{\hbar\omega_0}} e^{-\sqrt{\frac{\tilde{U}}{\hbar\omega_0}} s}. \quad (6.24)$$

Here, $\chi = 52.1$ and $s = 7.2$ are numerical constants, as given in Ref. [139]. The state of finite phase slips is only stable as long as the junction phase experiences sufficient dissipation. At some critical current I_S the dissipation is too small and the phase will start moving down the potential wall at a velocity $\dot{\phi}(t)$. That situation corresponds to the switching out of the zero voltage state, which can be observed experimentally in the tunneling characteristics. Although it is difficult to introduce continuous energy dissipation into a quantum-mechanical framework, Iansiti *et al.* succeeded in, at least, making an estimate for the current at which the junction leaves its bound state. To this end, they assumed that the work performed by the current to induce a phase shift of π – corresponding to a translation to the adjacent minimum – must be smaller than the binding energy of the lowest eigenmode inside the potential. In this way, the authors derived the switching current as [139]⁴

$$I_S = \frac{e}{4\hbar} \frac{E_J^2}{E_C}. \quad (6.25)$$

Interestingly, this estimate predicts a quadratic dependence of the switching current on the Josephson coupling energy for the regime $E_J \approx E_C$. In fact, Fig. 6.1(b) shows us that the switching current is of the same value as the maximum Cooper pair current peak found in voltage-biased measurements. For these experiments, we could show in Ch. 4 that the amplitude of the Cooper pair current scales with $I \propto E_J^2$.

It should be noted that the effects of phase tunneling on the junction properties were presented

⁴In a similar approach Ferrell *et al.* obtained the same result [149].

Chapter 6. Phase Dynamics of an Atomic Scale Josephson Junction

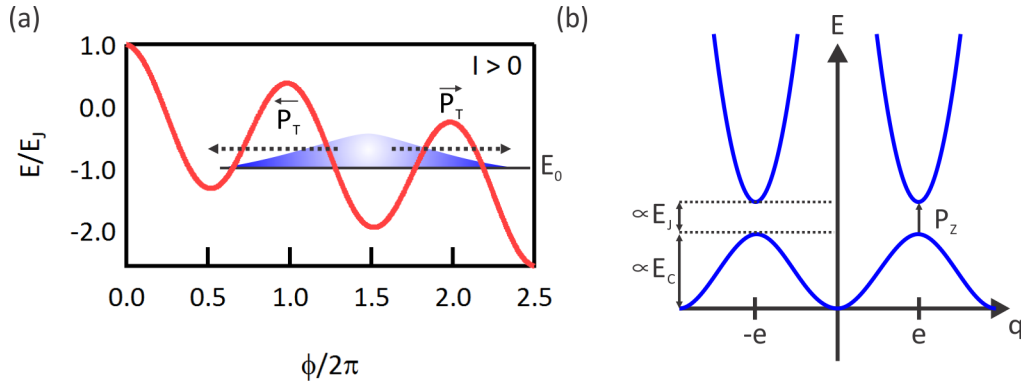


Figure 6.6 – (a) Illustration of the possible tunneling processes for the wavefunction $\bar{\Psi}(\phi)$. (a) Energy bands spectrum of the junction in the charge space for $\bar{\lambda} = 0.4$, adopted from Ref. [150]. The interband transition P_Z causing phase slips and premature switching out of the zero voltage state is indicated.

in phase space. On the one hand, this approach facilitates a very descriptive explanation of the physical phenomena, also referring to the particle in a washboard picture. On the other hand, for our experiment we find that, for most of the tunneling resistance range, the Josephson coupling energy is a bit smaller than the charging energy, $\bar{\lambda} = E_J/E_C \leq 1$. For this reason, the phase will experience a certain amount of delocalization which makes a precise treatment of the discussed phenomena challenging. Although the presented derivations on R_0 and I_S are at least qualitatively correct, for quantitative conclusions it appears favorable to move to a description in the charge space [139, 150, 151, 152, 153].

Here, the energy level diagram for the phase in the washboard potential is replaced by a “band structure“ $E(q)$ for the charge on the junction, which is similar to the band structure of an electron in a crystal. For example, Fig. 6.6(b), displays such a band structure for $\bar{\lambda} = 0.4$. The bandwidth scales with the charging energy E_C , whereas the band gap at the edge of the Brillouin zone, at $q = e$, is on the order of the Josephson coupling energy. In this picture, an intraband transition in the lowest band to the next Brillouin zone corresponds to the transfer of one Cooper pair across the tunnel junction. The discussed phase slips for $I \ll I_S$ in phase space here correspond to interband transitions into a higher band, as indicated in Fig. 6.6(b). This process is in analogy to Zener tunneling as observed in pn-diodes, for instance (see e.g. Ref. [143]). If the bias current increases, the probability for Zener tunneling also increases. At a critical current I_S the junction is not able to discharge the Cooper pairs from the capacitor anymore and the Zener breakdown occurs, i.e. the junction switches out of the zero-voltage state [150, 40, 139], as in analogous to the Zener breakdown in diodes.

This explanation might appear less descriptive than the presented explanation in phase space, yet the charge space representation facilitates a quantitative determination of the switching current in the limit $E_J \leq E_C$. Based on the theoretical framework for Zener tunneling, Iansiti *et*

al. could derive an expression for the switching current, giving [40]

$$I_{S,Z} = \frac{\pi e}{8\hbar} \frac{E_J^2}{E_C}. \quad (6.26)$$

In comparison to the expression for I_S derived in phase space we find that $I_{S,Z}$ is only larger by a factor of $\pi/2$ but shares the same quadratic dependence on E_J .

Finally, it should be noted that all the presented theoretical considerations have neglected the influence of thermal fluctuations described in Ch. 2, Sec. 2.4. The main reason is that for all values of the tunneling conductance, we find that, in our case, the thermal energy is always (much) smaller than the Josephson coupling energy (cf. compare Fig. 4.1). Hence, thermal activation of the phase over the washboard potential barrier is unlikely to occur and thus tunneling through the barrier will be the predominant source of premature switching out of the zero voltage state.

6.4 Numerical Simulation of the Phase Dynamics

Investigation of the phase dynamics ϕ by means of tunnel experiments can be complemented by performing numerical simulations on the temporal evolution of $\phi(t)$ as initially demonstrated in Ref. [146]. To this end, we start out with the classical differential equation for $\phi(t)$ with respect to time, as introduced in Ch. 2, Sec. 2.3, which we write again here [55, 59, 60, 146]:

$$I = I_0 \sin(\phi(t)) + I_{\text{QP}} \left(\frac{\hbar}{2e} \dot{\phi}(t) \right) + C \frac{\hbar}{2e} \ddot{\phi}(t). \quad (6.27)$$

This equation can be solved by numerical means using a differential equation solver such as the *ode45-solver* in Matlab. For the later analysis, we limit ourselves to the simulation of the retrapping characteristics of the Josephson junction, since the switching characteristics demand a quantum-mechanical treatment. For this reason, the boundary condition $\dot{\phi}(t=0) \neq 0$ has to be chosen. In order to calculate a full $I(V_J)$ tunneling spectrum for a range of current bias values $I = \{I_0, I_2, \dots, I_n\}$ it is necessary to solve this equation for each individual value of the current bias I_n , which itself serves as an input parameter. From the solution $\phi(t)$ we directly obtain its derivative $\dot{\phi}(t)$, which evolves in time as shown, for example, in Fig. 6.7. As soon as $\dot{\phi}(t)$ converges to a constant value, the voltage drop across the tunnel junction can be calculated using $V_J = (\hbar/2e)\dot{\phi}$.

We model the dissipative quasiparticle current $I_{\text{QP}}(\frac{\hbar}{2e}\dot{\phi}(t))$ via a lifetime broadened BCS density of states as given in Eq. 6.17 and 6.18 (cf. Ch. 2, Sec. 2.2.4).

Fig. 6.8 displays simulated $I(V_J)$ tunneling curves focused on the in-gap region $V_J \ll \Delta_1 + \Delta_2$ for all individual values of the tunneling resistance R_N as given in Sec. 6.5. For the simulation we used $C_J = 2.53$ fF, $\Delta_1 = 800 \pm 20 \mu\text{eV}$ and $\Delta_2 = 309 \pm 20 \mu\text{eV}$ (cf. Sec. 6.6) as well as lifetime broadening parameters $\Gamma_1 = 20 \mu\text{eV}$ and $\Gamma_2 = 63 \mu\text{eV}$ (cf. Sec. 6.7). By visual inspection of the

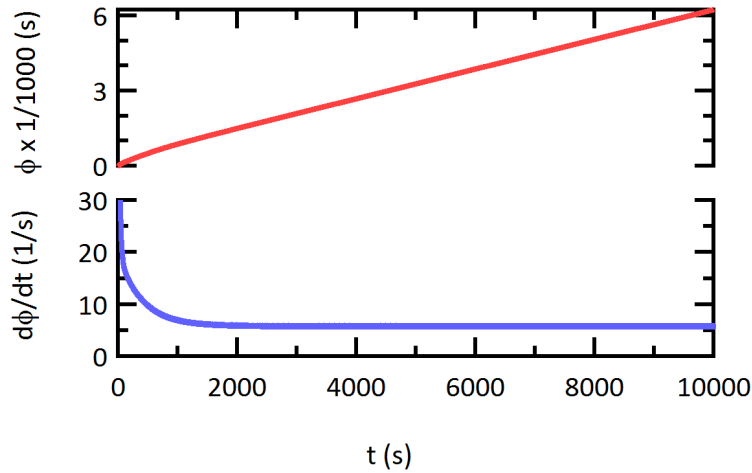


Figure 6.7 – $\phi(t)$ and $\dot{\phi}(t)$, as obtained by numerically solving Eq. 6.27 for a chosen bias current of $I = 100$ pA.

$I(V_J)$ curves, the increase in the retrapping current for decreasing tunneling resistance values is apparent. Moreover, the in-gap quasiparticle current is enhanced for reduced values of R_N which descriptively illustrates its significance as a dissipation channel effecting I_R .

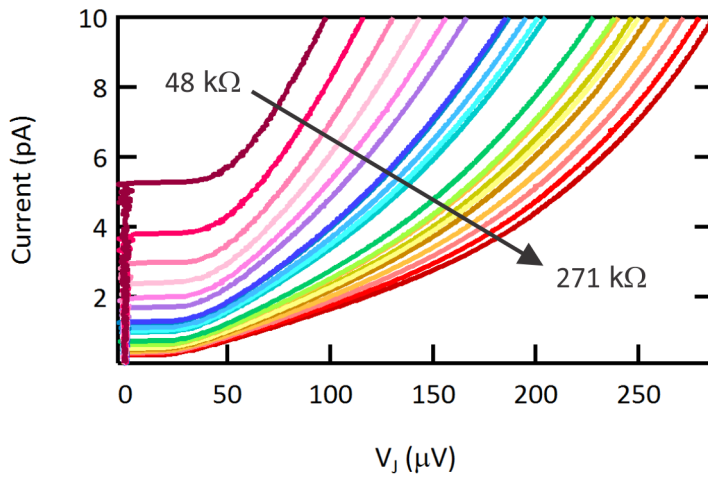


Figure 6.8 – $I(V_J)$ tunneling curves as calculated from the simulated $\dot{\phi}$ values plotted for different values of R_N , as indicated.

6.5 Comparison of Current-biased and Voltage-biased Experiments

To investigate the quantum-mechanical properties of the Josephson junction in our STM we performed experiments in which we applied both a bias voltage and bias current to the

6.5. Comparison of Current-biased and Voltage-biased Experiments

Josephson junction⁵. In this way, we can fully control the parameter space of the Josephson junction: By analyzing the $I(V_J)$ experiments we can precisely extract the Josephson critical current I_0 as well as the capacitance of the tunnel junction C_J . In conjunction with the tunneling resistance R_N these parameters serve as valuable input parameters for analyzing the $V_J(I)$ curves⁶. These measurements were performed as described in Ch. 3, Sec. 3.4 and 3.5,

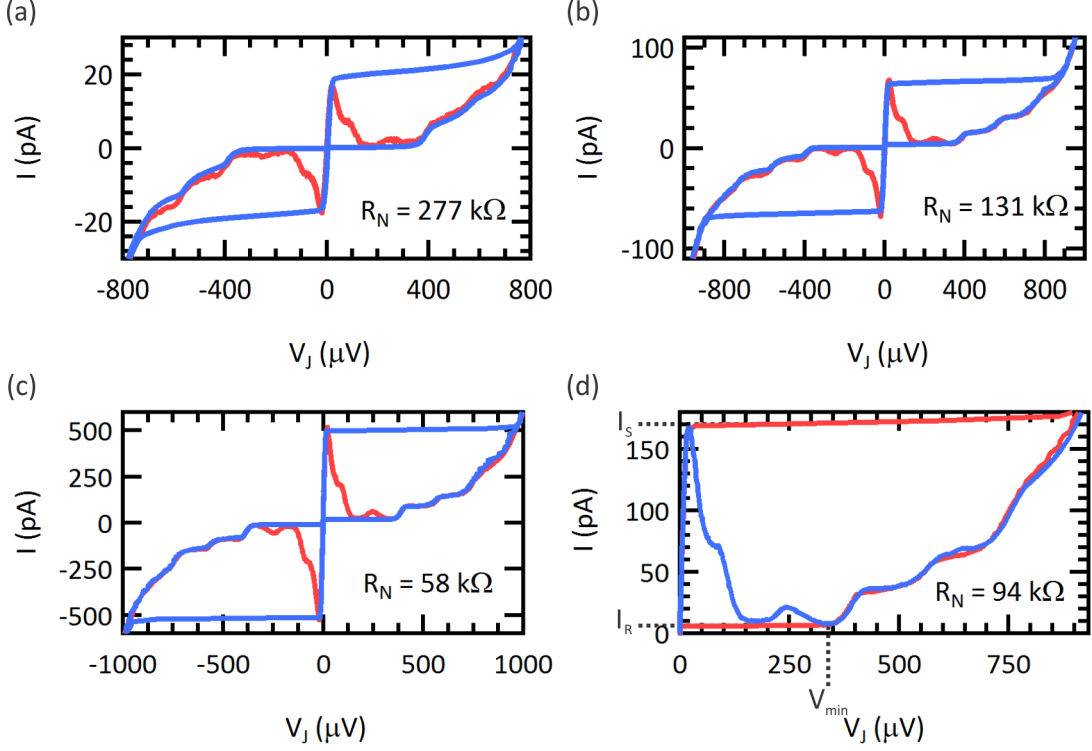


Figure 6.9 – (a-c) Comparison of voltage- and current-biased experiments for different values of R_N as indicated. (d) Exemplary $I(V_J)$ curve in which the relevant points for extracting I_S and I_R are indicated. Moreover, the point of minimum quasiparticle current, V_{\min} , is indicated.

using a large range of tunneling resistance values from $R_N \approx 50 \text{ k}\Omega$ to $R_N \approx 300 \text{ k}\Omega$. Figure 6.9(a-c) displays the experimental $I(V_J)$ curves for three different values of R_N and also compares the results obtained by voltage- and current-biased experiments. As it was already shown in Fig. 6.1, the $I(V_J)$ curves of both bias techniques perfectly match and only deviate for regions of negative differential conductance, i.e. $dI/dV_J < 0$. In particular, the agreement of both curves in the in-gap quasiparticle current for $V_J < 1 \text{ mV}$ and for the range of coherent Cooper pair tunneling around $V_J = 0$ will be of importance for the later analysis.

We assign the tiny deviations found between the two $I(V_J)$ curves to small deviations in the tunneling resistance of both experiments. Fig. 6.10 compares the fitted R_N values and their

⁵It should be noted that the inconsistency in terminology by using both the terms *tunneling conductance* and *tunneling resistance* is on purpose and reflects the common practice in the respective contexts.

⁶For the sake of simplicity the tunneling characteristics of both current- and voltage-biased experiments will be labeled $I(V_J)$ in the following, whereas the bias source will be mentioned where necessary.

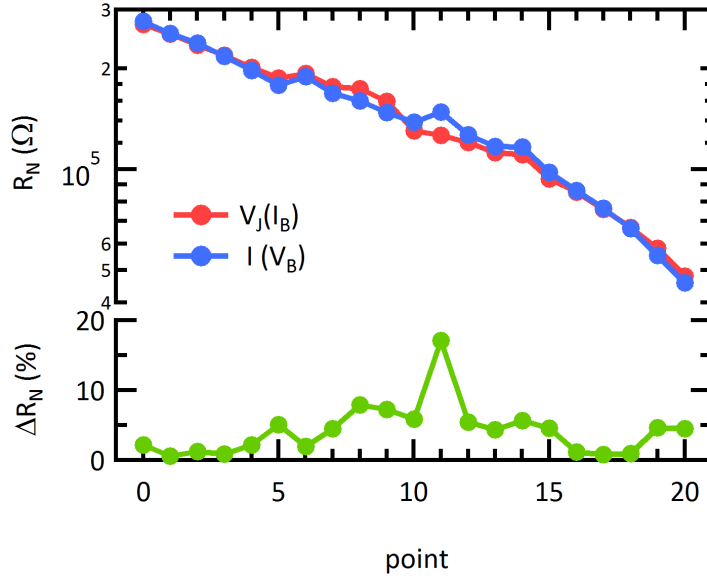


Figure 6.10 – Comparison of fitted tunneling resistance values R_N of voltage-biased and current-biased experiments as well as their relative deviation ΔR_N .

relative deviation ΔR_N (cf. Ch. 3, Sec. 3.4). We find that, for most measurements, the deviations are small $\Delta R_N \leq 5\%$ and might originate from a systematic error in adjusting the tunneling resistance by manually adjusting the tip-sample distance with the z -piezo. We find a larger deviation only for one value at $R_N = 148\text{ k}\Omega$. This could be induced, for instance, by a surface adsorbate in the tunnel contact leaving the contact instable. Nevertheless, the good agreement between the R_N values of voltage- and current-biased experiments allows us to combine results from both measurement techniques for investigating the quantum-mechanical properties of the Josephson junction in our STM.

From the $I(V_J)$ curve, as for example shown in Fig. 6.9(d), we extract the retrapping current I_R as the value of the bias current at which the voltage across the tunnel junction V_J rapidly drops to zero voltage, when the bias current is continuously decreased starting from $I_B > I_0$. We extract the switching current I_S as the value of the bias current at which the voltage across the tunnel junction V_J rapidly increases from zero to voltages on the order of Δ when starting from $I_B = 0\text{ A}$.

6.6 Analysis of the Voltage-biased Experiments

In this section we analyze the $I(V_J)$ curves obtained from voltage-biased experiments on the Josephson junction in our STM for all values of the tunneling resistance shown in Fig. 6.10. We employ $P(E)$ -theory and fit the $I(V_J)$ curves in the same fashion demonstrated in Ch. 4, Sec. 4.4. Figure 6.11 displays the experimental $I(V_J)$ characteristics and the corresponding fit, which is split up into the Cooper pair tunneling current, modeled by $P(E)$ -theory, and

the quasiparticle background. This separation will be of particular importance in the later analysis of the retrapping current. From Fig. 6.11 we see that the fit nicely models each single contribution to the total Cooper pair current. From such a fit we readily extract the Josephson coupling energy E_J , the junction capacitance C_J and the cubic background for each single value of the tunneling resistance ⁷.

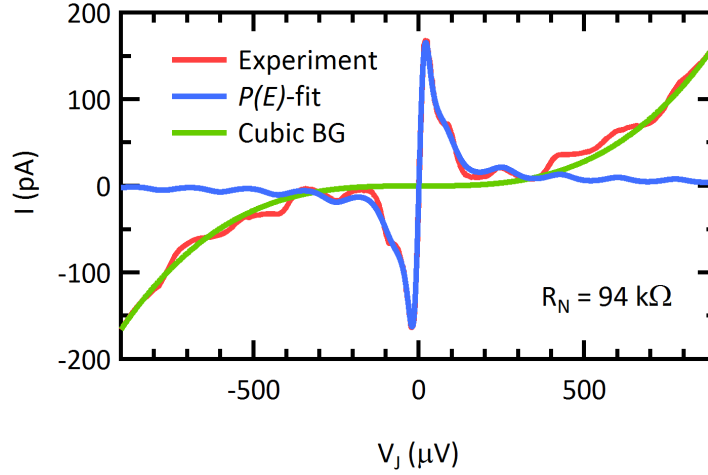


Figure 6.11 – $I(V_J)$ tunneling curves and the $P(E)$ -fit to data as well as the in-gap quasiparticle current, as modeled by the parameter c_2 .

In Figure 6.12(a) we plot the experimental Josephson critical current I_0 , that we calculated from the fitted E_J values as a function of the normalized tunneling conductance G_N/G_0 . Furthermore, we compare these values with theoretical values that we calculated using the Ambegaokar-Baratoff formula (Ch. 2, Eq. 2.21) [8]. As already demonstrated in Ch. 4, we can extract the gap values for the two superconducting electrodes from the dI/dV_J -spectrum and its derivative shown in Fig. 6.12(b). In this case, the superconducting properties of the tip were such that both spectra only feature the quasiparticle excitation peak at $\Delta_1 + \Delta_2 = 1109 \pm 10 \mu\text{eV}$. We therefore estimate the sample gap value to $\Delta_1 = 800 \pm 20 \mu\text{eV}$ – a value that represents the average value of the sample gaps found in our experiments – and yield a tip gap $\Delta_2 = 309 \pm 10 \mu\text{eV}$.

The fitted and calculated critical current values, shown in Fig. 6.12(a), are in good agreement along the entire range of tunneling conductance values, as we also found it for the experiment discussed in Ch. 4, Sec. 4.6. For this set of data, the deviations are slightly larger, especially for $G_N \geq 0.1G_0$. However, on average, we find an acceptable standard deviation between theory and experiment of $\sigma_{\Delta I_0} = 9\%$. Moreover, we find an unexpected behavior for I_0 at a conductance of about $0.09G_0$, which corresponds to a tunneling resistance of $R_N = 1/(0.09G_0) = 143 \text{ k}\Omega$. We already observed this abnormality when comparing R_N values

⁷To minimize uncertainties in the fit, we initially determined the lowest eigenmode of the tip ν_0 and its quality α to $\nu_0 = 42.1 \text{ GHz}$ and $\alpha = 0.71$, respectively, and afterwards kept these fixed when fitting the dependence of the $I(V_J)$ curves on R_N (cf. Ch. 4, Sec. 4.5.)

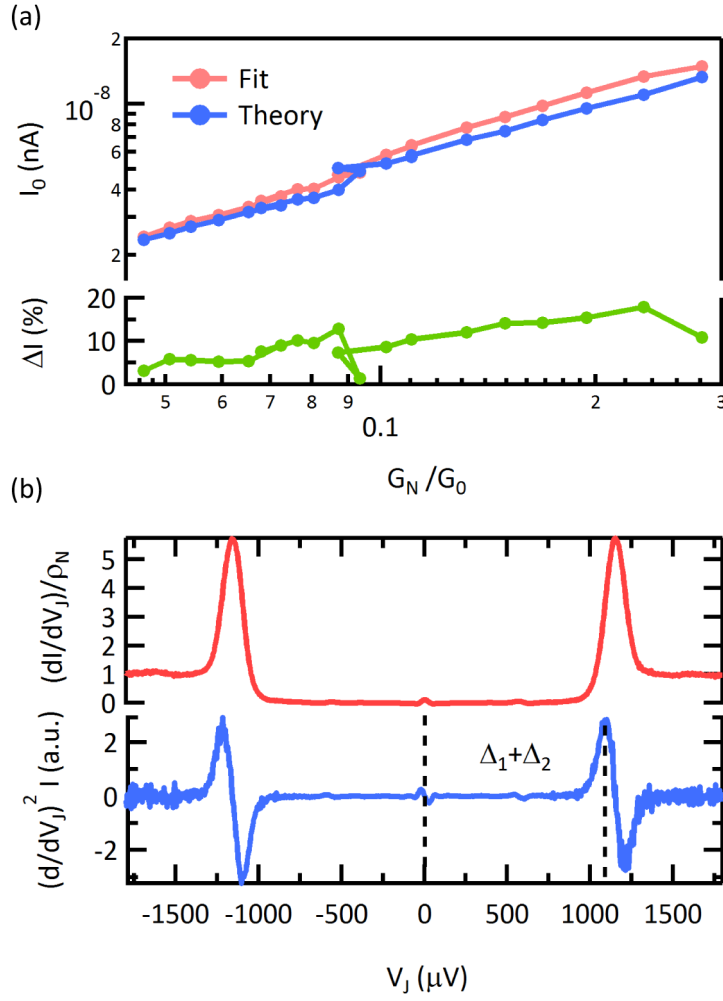


Figure 6.12 – (a) Comparison of experimental and theoretical I_0 values and their relative deviation ΔI_0 plotted as a function of R_N . (b) First dI/dV_J and second d^2I/dV_J^2 derivative of the quasiparticle tunneling current, which facilitate determination of the gap values Δ_1 and Δ_2 .

from voltage- and current-biased experiments in the last section.

In Fig. 6.13(a), we plot the fitted junction capacitance C_J as a function of R_N . Just as we found from the analysis of voltage-biased experiments in Ch. 4, C_J does not depend on R_N . Hence, we can calculate an average value of $C_J = 2.53 \pm 0.11$ fF, which we will use for the following analysis. In contrast, the fit parameter c_2 , which models the in-gap quasiparticle current, exhibits a strong dependence on R_N . Whereas c_2 remains almost constant for larger values of R_N , it drastically increases when R_N is reduced below 100 k Ω . The constant contribution originates from the lifetime-broadened superconducting density of states (cf. Ch. 2, Sec. 2.2.4). We can fit the strong increase in c_2 with a power law function $c_2 = \tilde{A}/R_N^\xi$ as shown in Fig. 6.13(b). From the fit we find $\xi = -1.94 \pm 0.07$, $\tilde{A} = (1.02 \pm 0.82) \times 10^9$ 1/(AV). The square dependence of the in-gap current on the tunneling resistance is a strong indication that the dominant source

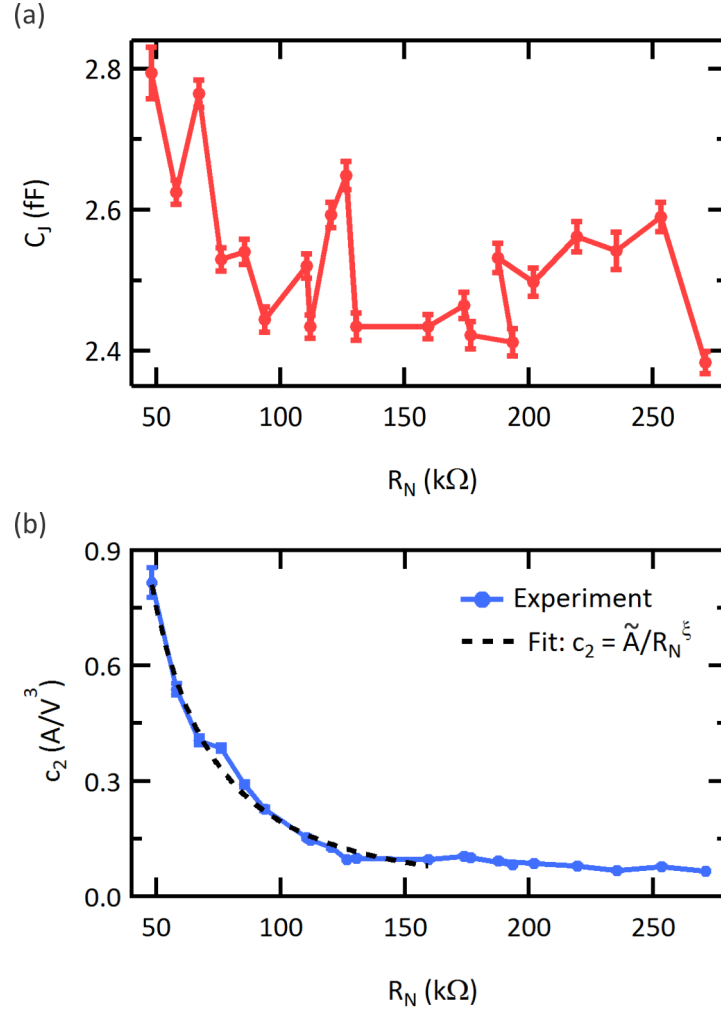


Figure 6.13 – (a) Junction capacitance C_J as extracted from the $P(E)$ -fits plotted as a function of R_N . (b) Cubic background parameter c_2 as extracted from the $P(E)$ -fits as well as the fit to the c_2 parameter plotted as a function of R_N .

of the gap filling is Andreev reflections, a typical feature in transparent tunnel contacts, as introduced in Ch. 2, Sec. 2.2.3. At this point we keep the analysis of the in-gap quasiparticle current on the presented phenomenological level, which should be sufficient for the later investigation of the phase dynamics $\dot{\phi}(t)$. A more detailed analysis of this quasiparticle current is certainly desirable, also in view of the multiple Andreev reflection processes, but will be part of future work.

In Sec. 6.3.1 we could derive a relation between the phenomenological lifetime parameter Γ and the retrapping current of the Josephson junction. To determine the Γ values of the superconducting gaps, it is necessary to investigate the quasiparticle excitation spectrum (cf. Ch. 2, Sec. 2.2.4). To this end, we calculate the first derivative dI/dV_J of the quasiparticle tunneling current from the experimental $I(V_J)$ curves, as shown in Fig. 6.14(a). We perform

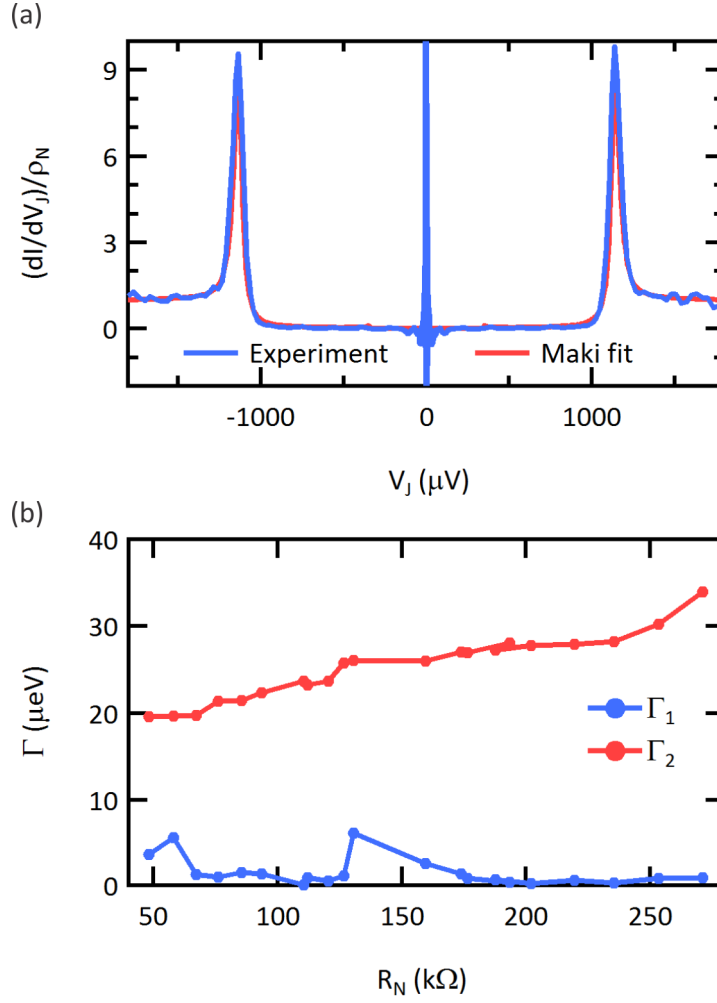


Figure 6.14 – (a) dI/dV_J spectrum normalized to the normal metal density of states ρ_N measured at $R_N = 86\text{k}\Omega$ and the fit to data using the extended Maki model. (b) Lifetime broadening parameter of the sample Γ_1 and the tip Γ_2 , as extracted from the Maki fits, plotted as a function of R_N .

this calculation for all values of the tunneling resistance R_N given in Sec. 6.5. It should be noted that the large feature around zero voltage in the $dI(V_J)/dV_J$ curves of Fig. 6.14(a) is an artifact that results from differentiating the current signal. We can fit the resulting dI/dV_J spectra using an extended Maki model [154, 155, 156]. In comparison to the BCS model introduced in Ch. 2, the Maki model used for this study contains an additional *depairing parameter* ζ that effectively reduces the amplitude of the coherence peaks at $V_J = \Delta_1 + \Delta_2$. The modified superconducting density of states reads as

$$\rho_{S,Maki}(E) = \frac{\rho_N}{2} \text{sgn}(E) \text{Re} \left(\frac{u_{\pm}}{\sqrt{u_{\pm}^2 - 1}} \right). \quad (6.28)$$

Here, u_+ and u_- are implicitly defined functions:

$$u_{\pm} = \frac{E - i\Gamma}{\Delta} + \frac{\zeta u_{\pm}}{\sqrt{1 - u_{\pm}^2}}. \quad (6.29)$$

Fig. 6.14 shows a fit to an experimental dI/dV_J spectrum using this model. From the fits, we extract the lifetime parameter Γ_1 and Γ_2 , which we plot as a function of the tunneling resistance R_N in Fig. 6.14(b). Whereas Γ_1 of the sample does not show any dependence on R_N , Γ_2 of the tip slightly decreases for smaller R_N values. However, this behavior is counter intuitive since we actually expect the gap to fill up when R_N is reduced, which should result in a strong increase of Γ_2 . A possible explanation is that the dependence of the coherence peaks on the Γ -value is much stronger in comparison to the gap-filling introduced by this parameter. In comparison, the c_2 parameter, which includes contributions from both Γ and Andreev reflections and also models the gap-filling, does strongly depend on R_N . Nevertheless, for the later analysis of the in-gap quasiparticle resistance we can assume Γ to be independent of R_N and employ average values for the lifetime parameter of $\Gamma_1 = (1.40 \pm 1.28) \mu\text{eV}$ and $\Gamma_2 = (25.3 \pm 3.8) \mu\text{eV}$, respectively.

6.7 Analysis of the Retrapping Current

In Section 6.3.1 we introduced the concept that the retrapping current I_R serves as a probe for the dissipative interaction of the Josephson junction with its environment and that for tunnel junctions this dissipation originates from breaking up Cooper pairs. To analyze this dissipative interaction we extract the retrapping current I_R as defined in Sec. 6.5 and plot it as a function of the tunneling resistance R_N in Fig. 6.15. We find that I_R is strongly dependent on R_N and increases by two orders of magnitude when R_N is reduced by only half an order of magnitude. In view of Eq. 6.15 this observation signifies that the effective in-gap resistance R_{eff} drastically changes on this tunneling resistance interval.

To investigate the dependence $I_R(R_N)$, we employ Eq. 6.22 to fit the retrapping current, which is displayed in Fig. 6.15. We find that the fit nicely models the retrapping current for larger values of the tunneling resistance, $R_N \geq 150 \text{ k}\Omega$ but underestimates its value when the junction becomes more transparent, $R_N \leq 150 \text{ k}\Omega$. For fitting, we used the average values for C_J , Δ_1 and Δ_2 as given in Sec. 6.6. For the fit, we keep one lifetime parameter constant at a reasonable value, $\Gamma_1 = 20 \mu\text{eV}$ and for the second lifetime parameter we find $\Gamma_2 = (63 \pm 4) \mu\text{eV}$. Despite the fact Γ_1 was deliberately kept constant, we find that both Γ values obtained from fitting the retrapping current are (much) larger than the Γ values found from the Maki fits in the last section. On the one hand and as discussed before, the Γ parameter in the extended Maki model might be relatively insensitive to the very small in-gap density of states (cf. Fig. 6.14(a)) in comparison to its drastic influence on the coherence peak width and amplitude [54]. For this reason, the in-gap density of states, which strongly affects the retrapping current via the effective in-gap resistance, might not be perfectly modeled by the Maki fits. On the other hand,

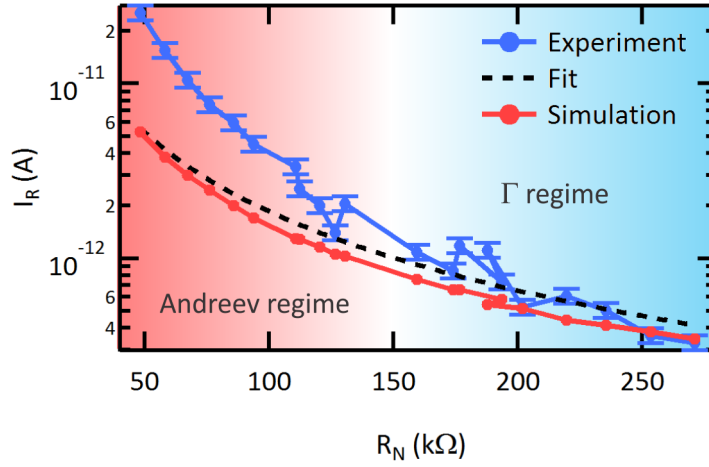


Figure 6.15 – Experimental and simulated retrapping current and the fit to experimental data plotted as a function of R_N . For the simulated retrapping current the error bars are included in the symbols.

the quantitative modeling of I_R on an analytical basis is difficult to achieve [148, 147] and, so far, published studies on this topic only obtained a qualitative agreement between experiment and theory [140].

The deviation between fit and experimental data for $R_N \leq 150 \text{ k}\Omega$ can be better understood if we also consider the in-gap quasiparticle currents observed in voltage-biased experiments in Sec. 6.6. Here, the in-gap current was nicely modeled by the c_2 parameter. We found that this parameter, shown in Fig. 6.13, strongly increases for $R_N \leq 150 \text{ k}\Omega$ and we could assign this increase to the likely onset of Andreev reflections causing the observed in-gap quasiparticle currents. In contrast, for larger values of the tunneling resistance, c_2 is nearly constant and displays the finite in-gap current that results from lifetime effects, as expressed by Γ . Hence, for $R_N \geq 150 \text{ k}\Omega$ the effective in-gap resistance R_{eff} is significantly reduced by the lifetime effects of Cooper pairs, whereas for smaller values of the tunneling resistance the in-gap resistance is dominated by Andreev reflections. In comparison, both Γ -parameters that model the effective in-gap resistance in Eq. 6.22 do not comprise an implicit R_N dependence. For this reason, Γ cannot account for a reduction in R_{eff} due to Andreev reflections and the analytic expression given in Eq. 6.22, which relates lifetime effects of Cooper pairs to the retrapping current, is not applicable in this regime.

We obtain very similar results for the retrapping currents that we extract from the simulated $I(V_J)$ curves introduced in Sec. 6.4⁸. For the simulation we used the Γ values that we obtained from the fit to the experimental retrapping currents using Eq. 6.22. In Fig. 6.15 we plot the simulated retrapping currents as a function of the tunneling resistance. Remarkably, the I_R values found from the simulations almost perfectly reproduce the fitted I_R curve. As a

⁸The I_R values are determined in the same fashion as demonstrated in Sec. 6.5.

consequence, the simulated I_R values match their experimental counterparts for $R_N \geq 150 \text{ k}\Omega$ but also underestimate their values for $R_N \leq 150 \text{ k}\Omega$. On the one hand, this is certainly expected, since the dissipative quasiparticle current in the simulation is of the same form as the current used for the derivation of Eq. 6.22. On the other hand, this result corroborates the validity of our assumptions made for deriving Eq. 6.22. Hence, Eq. 6.22 can be regarded as a proper description for modeling the retrapping currents in the regime $R_N \geq 150 \text{ k}\Omega$.

Nevertheless, we can address the enhanced in-gap quasiparticle current arising from Andreev reflections on a phenomenological level in order to correctly model the experimentally observed retrapping currents. To this end, we again look at the c_2 parameter from the $P(E)$ -fits in Sec. 6.6. Comparing voltage- and current-biased experiments in Fig. 6.9(a-d) we could show that the in-gap quasiparticle currents from both measurements are identical. Therefore, the effective in-gap resistance at which the junction retraps can be calculated on the basis of the c_2 parameter. In detail, we calculate the differential conductance dI/dV_J of the quasiparticle current according to $dI/dV_{QP} = 3c_2 \times V^2$. Figure 6.9(a-d) shows that the retrapping occurs at the same voltage of $V_{\min} \approx 330 \mu\text{eV}$ independent of the tunneling resistance. Hence, the effective in-gap resistance at which the junction retraps calculates as

$$R_{\text{eff}} = \left. \frac{1}{dI/dV_J} \right|_{V=V_{\min}} = \frac{1}{3c_2} V_{\min}^{-2}. \quad (6.30)$$

From these values for the effective in-gap resistance, we can easily calculate the retrapping current from Eq. 6.15. In Fig. 6.16 we plot these I_R values together with the experimentally determined I_R values as a function of R_N . We find quantitative *and* qualitative agreement between calculation and experiment over the entire range of tunneling resistance values. In particular, in the regime of $R_N \leq 150 \text{ k}\Omega$, where Andreev reflections strongly reduce R_{eff} , the calculation now correctly models the resulting strong increase in I_R .

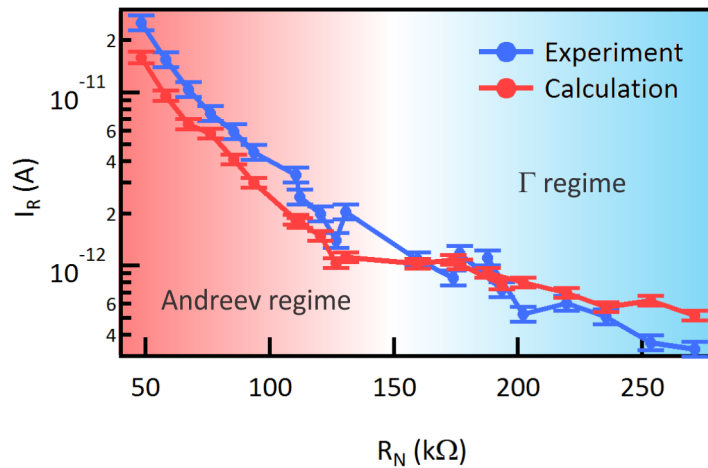


Figure 6.16 – Comparison between experimental retrapping values and calculated values using the c_2 parameter plotted as a function of R_N .

Together, our experimental results demonstrate that the dependence of the retrapping current on the tunneling resistance can be separated into two regimes. These regimes are determined by two different dissipative interactions of the junction phase with the environment. We find that for opaque tunnel junctions – in our case $R_N \geq 150\text{k}\Omega$ – dissipation is dominated by lifetime effects of Cooper pairs. In this regime, the dissipative interaction is properly described by the analytic expression given in Eq. 6.22. In contrast, for transparent tunnel junctions – in our case for $R_N \leq 150\text{k}\Omega$ – the onset of Andreev reflections strongly enhances dissipation, which we can phenomenologically address with a simple model based on the in-gap quasiparticle current. However, it should be noted that another experimental study found an influence of the circuit impedance $Z(2\pi\nu)$ on the energy dissipation of the junction phase [142]. Analyzing temperature-dependent measurements on the retrapping current, the authors argue that at low temperatures quasiparticle dissipation due to thermally excited quasiparticles freezes out, and that in this situation the dissipation is temperature-independent and dominated by the circuit impedance. This effect could certainly also be of relevance in our experiment, not least because our model for the retrapping current based on Cooper pair lifetime effects overestimates this dissipation channel in comparison to independently determined lifetime values that we obtained from fitting dI/dV_J spectra using the Maki model. However, from the current point of view a detailed comparison of our study with Ref. [142] is difficult. Whereas we directly tune the in-gap quasiparticle current via the tunneling resistance, the authors of Ref. [142] tune the quasiparticle dissipation via the temperature and neglect any in-gap dissipation due to Cooper pair lifetime effects or Andreev reflections. Nevertheless, for a better comparability we will address the dissipative potential of our environmental impedance $Z(\nu)$ in future work.

Last but not least, we want to address the question of why the temporal evolution of the quantum-mechanical operator ϕ satisfies a classical equation of motion. Let us again assume that the junction phase can be represented by a wavefunction $\bar{\Psi}(\phi)$ and that this wavefunction is sufficiently localized inside a potential minimum, i.e. $\sigma_\phi \leq \pi$. In the running state the wave package moves down the potential well to a finite position where it is retrapped inside a minimum at a particular bias current value I_B . Certainly, if we repeat this measurement over and over, the probability of presence of the junction in phase space, as expressed by its wavefunction, will induce a statistical spread on the measurement result. However, a sufficient localization of $\bar{\Psi}(\phi)$ also signifies that the probability of presence is centered around a particular point in phase space, its expectation value $\langle \phi \rangle$. In a *classical picture* the junction phase therefore has a certain center of mass ϕ_c . It is now easy to imagine that the bias current value at which this moving center of mass retraps into a potential minimum will approximately be of the same value for a large number of measurement repetitions and, additionally, that the statistical spread, which results from the quantum-mechanical nature of ϕ , will be negligible.

This attempted descriptive explanation is a close analogy to the *Ehrenfest theorem* that, together with the correspondence principle, describes the transition from quantum mechanics to classical mechanics [157, 158, 144]. In 1927 Paul Ehrenfest showed for a *linear potential* that the time-evolution of the expectation value of a quantum-mechanical operator obeys

a classical equation of motion. The correspondence principle by Niels Bohr postulates that in the limit of infinite repetitions an experiment will always converge to a result that can be described by classical mechanics and that the statistical spread of the results will be unmeasurable small. However, it should be emphasized at this point that the Ehrenfest theorem only applies to systems with a *linear* potential and that it can actually not be applied to our system in which the washboard potential is periodic, i.e. it is *highly non-linear*. Yet, it might be an interesting question to address whether such a classical limit can also be theoretically derived for non-linear potentials.

6.8 Analysis of the Zero Voltage State

In contrast to the phase dynamics that satisfy a classical equation of motion for our experimental conditions, the analysis of the zero voltage state requires a quantum-mechanical description, which we introduced in Sec. 6.3.2. In particular, the tunneling out of the potential well, which is favored by a certain delocalization of the junction phase, strongly effects the amplitude of the DC Josephson current [31, 40, 141]. For this reason the so-called switching current I_S , at which the Josephson junction leaves its zero voltage state, can serve as a valuable probe for investigating how *quantum-mechanical* the junction behaves.

To this end, we determine the switching current from the current-biased experiments in the way explained in Sec. 6.5 and plot it as a function of the tunneling resistance in Fig. 6.17(a). For comparison, we also plot the Josephson critical current I_0 , as calculated in Sec. 6.6, as a function of R_N . We find that the I_S values are at least one order of magnitude smaller than the corresponding I_0 values along the entire range of R_N . The double logarithmic plot of Fig. 6.17(a) also highlights that the slope of the I_S curve is twice as large as that of the I_0 curve. Since the critical current relates to the tunneling resistance as $1/R_N$ (cf. Ch. 2, Sec. 2.2.5), the relation between switching current and tunneling resistance should be on the order of $1/R_N^2$. Considering theory on the zero voltage state of a quantum-mechanical junction presented in Sec. 6.3.2, the Zener-model indeed predicts a $1/R_N^2$ dependence for the switching current that results from tunneling phenomena of the delocalized phase.

For a more detailed comparison of theory and experiment we employ Eq. 6.26 in order to calculate the theoretical switching current, which we plot together with the experimental values in Fig. 6.17 as a function of G_N/G_0 . For the calculation of I_S we used the fitted C_J and I_0 values as determined in the voltage-biased experiments of Sec. 6.6. We find excellent agreement between calculated and experimental values of the switching current for $R_N \leq 100 \text{ k}\Omega$, which is in accordance to reported results on planar junction geometries [141]. Only for larger values of R_N do the deviations increase. A possible explanation for this increasing deviation is illustrated in Fig. 6.17(b), in which we plot the relative deviation $\Delta I_S = |(I_{S,\text{exp}} - I_{S,\text{calc}})/I_{S,\text{calc}}|$ as a function of E_J/E_C . We find that ΔI_S continuously increases when the ratio E_J/E_C is reduced to values much smaller than unity. In comparison, the lower limit of the quantum-mechanical regime that we derived in Sec. 6.2 $E_J/E_C \geq 0.3$ is much larger than the maximum ratio for

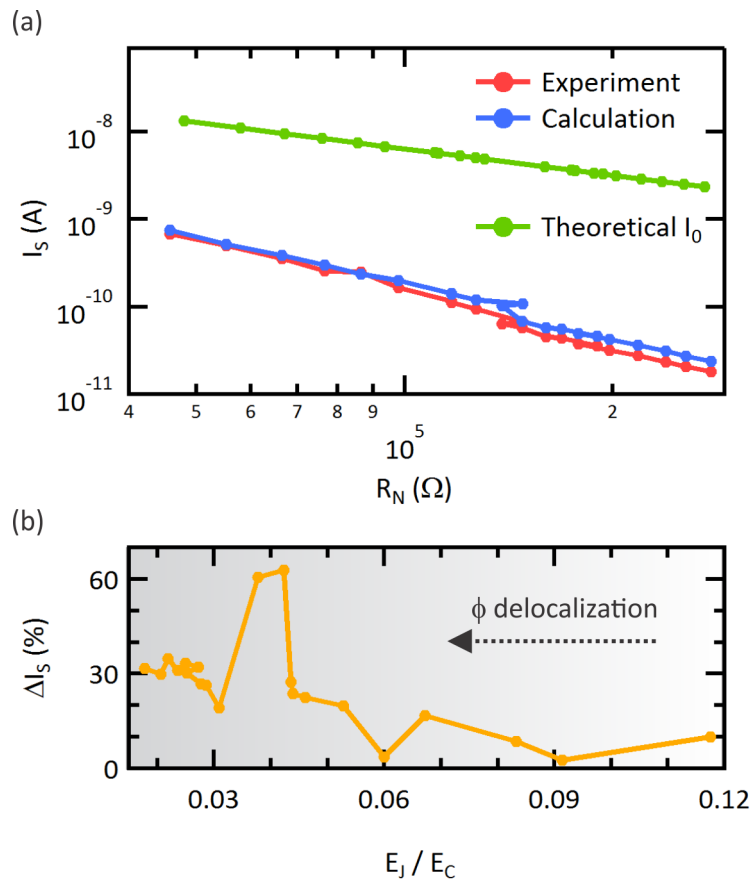


Figure 6.17 – (a) Comparison of Josephson critical current I_0 , experimental and calculated switching current I_S plotted as a function of R_N . (b) Relative deviation ΔI_S between experimental and calculated I_S values plotted as a function of E_J / E_C .

the experimental data presented in this chapter, $E_J/E_C \leq 0.12$. Hence, for $E_J/E_C \ll 1$ the phase will be highly delocalized and is not a good quantum number to describe the system. Accordingly, theoretical models, such as the Zener-model in Eq. 6.26, which are evaluated for the regime $E_J \approx E_C$, will fail for $E_J \ll E_C$. In contrast, in this limit the charge is a good quantum number and in this regime $P(E)$ -theory should be the appropriate theory for describing our experimental data (cf. Ch. 4) [37, 38].

In fact, in Sec. 6.6 we were able to fit the $I(V_J)$ curves from the corresponding voltage-biased experiments for all values of the tunneling conductance using $P(E)$ -theory. Moreover, for the experiment presented in Ch. 4, Sec. 4.5 we found that $P(E)$ -theory nicely describes our experimental data for $E_J/E_C \leq 0.33$ but fails for $E_J/E_C > 0.7$. Together these experimental results indicate that in the quantum-mechanical regime for $E_J/E_C > 0.3$ the quantum-mechanical nature of the junction phase significantly alters the experimental $I(V_J)$ curves. For smaller values $E_J/E_C < 0.3$, however, the relevance of quantum effects is reduced, the charge evolves as a good quantum number and $P(E)$ -theory represents the appropriate theory for describing our experimental data in this limit.

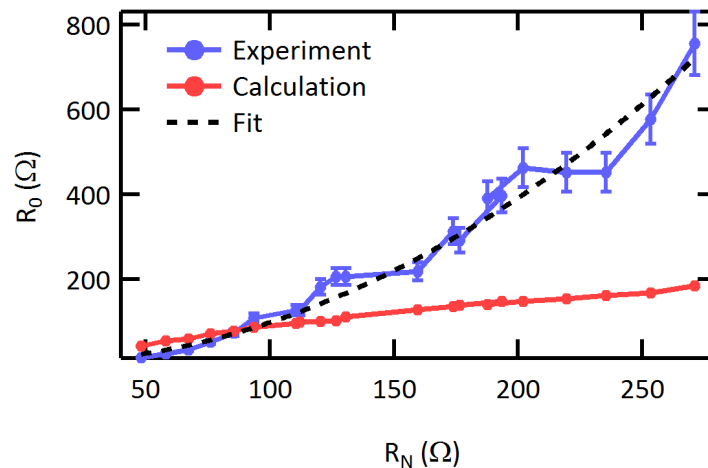


Figure 6.18 – Experimental and calculated values of the zero voltage resistance R_0 as a function of R_N . The dashed line represents a simple square fit to the experimental data.

Before the junction switches out of the zero voltage state into the running state, eventual phase tunneling events between adjacent potential minima are possible as well. These *phase slip* events constitute a measurable effect that manifests as a finite slope in the DC Josephson current (cf. Sec. 6.3.2) [31, 41, 139]. As a result, the Josephson effect can be observed at small finite voltages, in our system typically on the order of $\leq 20 \mu\text{eV}$. To better understand this phenomenon we investigate the *zero voltage resistance*, $R_0 = \Delta I / V_J$ for $I < I_S$.

In Figure 6.18 we plot the experimental R_0 values as a function of the tunneling resistance R_N . In addition, we plot the theoretical R_0 values that we calculated using Eq. 6.23 [41, 139]. For the calculation we used the values for the junction capacitance C_J and the Josephson

coupling energy E_J as they were determined by analyzing the voltage-biased experiments in Sec. 6.6. The Experimental and the calculated values of R_0 match for $R_N \leq 100\text{k}\Omega$, but exhibit significant deviations for larger values of the tunneling resistance. Interestingly, we observe similar deviation characteristics in the analysis of the switching current, where we find that the Josephson junction is not in the quantum-mechanical regime, i.e. $E_J/E_C < 0.3$. Moreover, also in literature good agreement between experimental and theoretical R_0 values is only reported for $E_J \approx E_C$ [41, 139].

The origin of these deviations in the limit $E_J \ll E_C$ comes to light when we again employ $P(E)$ -theory, which provides an expression to model the zero voltage resistance. In detail, Ingold *et al.* could show that the zero voltage resistance of the DC Josephson effect scales as $R_0 \propto R_N^2$ [107]. In Figure 6.18 we apply a simple square fit to the experimental R_0 values, $R_0 = B \times R_N^2$, and observe that R_0 indeed follows such a square dependence. Moreover, in Ch. 4 we show that in the DCB regime, i.e. $E_J \ll E_C$, thermal voltage fluctuations strongly effect the $P(E)$ distribution around zero voltage. Hence, possible phase slip events due to the quantum-mechanical nature of ϕ , i.e. quantum fluctuations, might be masked by thermal fluctuations. A more detailed analysis of this zero voltage resistance was theoretically performed by Ingold *et al.* in a later publication [159]. However, its application to experiment is quite involved and will be part of future work.

6.9 Conclusion

To conclude, in this chapter we investigated the properties of a Josephson junction in a regime in which the Josephson coupling energy is comparable to the capacitive charging energy by means of current-biased *and* voltage-biased experiments. By comparing the $I(V_J)$ curves of both experiments, we found that the quasiparticle tunneling currents at finite voltage perfectly match. We also observed excellent agreement for the current around zero voltage that originates from the coherent tunneling of Cooper pairs associated with the DC Josephson effect. From investigations on the retrapping current I_R , we found that the temporal evolution of the junction phase satisfies a classical equation of motion. Moreover, we could determine two different channels for energy dissipation of the junction phase. For smaller values of the tunneling resistance, $R_N \leq 150\text{k}\Omega$, the junction dissipates via Andreev reflections, whereas for larger values, $R_N \geq 150\text{k}\Omega$, the energy dissipation is dominated by lifetime effects of Cooper pairs.

In contrast to the above picture, when investigating the switching current I_S we found that an appropriate description of the zero voltage state stability requires a fully quantum-mechanical picture. For $E_J < E_C$ find that the premature switching out of the zero voltage state can be explained by phase tunneling through the potential walls, although the junction is not directly operated in the quantum-mechanical regime, as defined in Sec. 2.5. In contrast, in the limit $E_J \ll E_C$ we find that the relevance of phase tunneling phenomena is reduced and that $P(E)$ -theory represents the appropriate theory to describe our experimental data.

7 Conclusion & Outlook

7.1 Conclusion

The aim of this thesis was to characterize the properties of a Josephson junction in an STM at millikelvin temperatures and to implement JSTM as a versatile probe on the atomic scale. Such a process first demands an understanding of the regime in which the junction is operated. Second, on this basis the inelastic interaction of the Josephson junction with its immediate environment as well as the dynamics of the Josephson junction have to be understood. Moreover, an appropriate theory has to be implemented that allows us to extract the critical Josephson current from experimental data in view of the application of JSTM as a probe for superconductivity.

To this end we investigated the $I(V_J)$ tunneling characteristics of the Josephson junction in our STM at a base temperature of 15 mK by means of current-biased and voltage-biased experiments. In Ch. 4 we observed that in the tunnel regime, $G_N \ll G_0$, the Josephson junction is operated in the dynamical Coulomb blockade (DCB) regime in which the sequential tunneling of Cooper pairs dominates the tunneling current. Employing $P(E)$ -theory [37, 38, 112, 107] allowed us to model experimental $I(V_J)$ characteristics from voltage-biased experiments and determine experimental values of the Josephson critical current in agreement to theory [8]. Moreover, we observed a breakdown of $P(E)$ -theory for experiments at large tunneling conductance $G_N \approx G_0$, which could indicate that the coherent tunneling of Cooper pairs strongly contributes to the tunneling current in this limit.

Analyzing the $I(V_J)$ curves from voltage-biased experiments we observed in Ch. 5 that the Josephson junction in an STM at millikelvin temperatures is highly sensitive to its electromagnetic environment [39]. The combination of the experiment with finite integral simulations revealed that the immediate environment of a Josephson junction in an STM is frequency-dependent and additionally, that the STM geometry shares the electric properties of a monopole antenna with the STM tip acting as the antenna.

Comparing the $I(V_J)$ curves of voltage-biased and current-biased experiments in Ch. 6 we ob-

served that the dynamics of the junction phase exhibit underdamped characteristics. We could show that at these low temperatures the dynamics of the junction phase are dominated by the in-gap quasiparticle tunneling current. For opaque junctions $G_N < 0.1G_0$ this quasiparticle current originates from Cooper pair lifetime effects and that in more transparent junctions, $G_N > 0.1G_0$, it is strongly enhanced by Andreev reflections. Moreover, from comparing current- and voltage-biased experiments we also observed that the quantum-mechanical nature of the junction phase strongly effects the junction properties for $G_N \leq G_0$.

To conclude, we fully characterized the properties of the Josephson junction in an STM that is operated at millikelvin temperatures. Hence, this work represents necessary and fundamental steps that allow us to employ the Josephson effect as a versatile probe on the atomic scale. In the following outlook, we will give examples for JSTM applications that can be realized using our experiment. Moreover, we will give an outlook on general questions of Josephson tunneling which can be ideally addressed using our STM experiment. Partly, the given examples directly follow from the thesis' results.

7.2 Outlook

7.2.1 JSTM: Probing the Superconducting Ground State

A very promising application for Josephson STM is to study spatial variations of the superconducting order parameter Δ in non-conventional superconductors. In BSCCO, for example, the superconducting gap, as measured via quasiparticle excitations, reveals a strong response to local doping by both magnetic and non-magnetic impurities [74, 160, 101, 161]. Here, the sensitivity of JSTM to the superconducting ground state itself could provide more insight into the underlying interaction. Moreover, for the same class of superconductors JSTM could help to shed light onto the pairing symmetry and pairing mechanism of the superconducting ground state as proposed by the group of Alex Balatsky [14].

Another interesting question to explore is the perturbation of the superconducting ground state of a BCS superconductor by a single magnetic impurity. While theory predicts a strong response of the superconducting ground state [18], in experiments no change of quasiparticle excitation energy was observed [16, 19]. Even in experiments where the interaction between the magnetic impurity and the substrate was evidently strong, the gap remained unaffected [20]. Again, JSTM could represent the appropriate experimental technique to study the local interaction of a superconductor with a magnetic impurity, as it was proposed by theory [17]. If the interaction between magnetic impurity and superconductor is sufficiently strong, even a π -junction where the order parameter of the sample changes sign, $\Delta \rightarrow -\Delta$, could be realized [17].

We recently started with first experiments on the interaction of a single magnetic moment with a superconducting ground state. To this end, we deposited copper phtalocyanine (CuPc)

molecules – a spin-1/2 system – on top of the vanadium surface¹. Fig. 7.1(a) displays a single CuPc molecule on top of a V(001) surface. We already performed first test measurements on this sample system and we could observe the Josephson effect *through* a single molecule as shown in Fig. 7.1(b). Moreover, we were also able to fit these initial $I(V_J)$ curves by using $P(E)$ -theory.

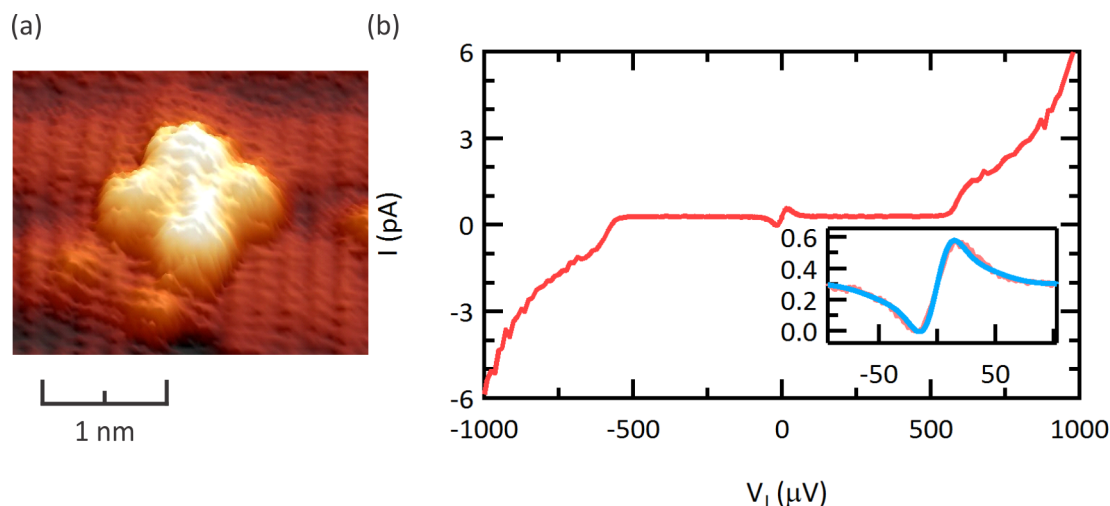


Figure 7.1 – (a) Single CuPc molecule on top of a V(001) surface. (b) Large scale: Initial measurement of the Josephson effect through a single CuPc molecule. The inset shows a $P(E)$ -fit to the experimental $I(V_J)$ curve.

These first results indicate that it is indeed possible to measure and analyze the Cooper pair current through a single adsorbate on a superconducting surface, an observation that provides the basis for a more detailed study.

7.2.2 Cooper Pairs and Photons I: The AC Josephson Spectrometer

Large research efforts concentrate on studying single electronic and nuclear spins using a variety of experimental techniques such as STM, break junctions or NV magnetometry [24, 129, 162, 163, 164]. The sensitivity of the Josephson junction in our STM to its electromagnetic environment could also be exploited in the *AC Josephson spectrometer* for probing electromagnetic transitions in nanoscale systems, a concept that has already been realized in planar junction geometries [22, 23]. A possible sample system that can be prepared in our experiment are single magnetic molecules, such as CuPc molecules shown in the last section. However, in the case of CuPc on V(001) we could not observe inelastic spin-flip transitions in magnetic fields up to 7 T, which indicates that the spin moment of the copper atom could have been compensated by the substrate due to hybridization effects. However, it was shown by the group of Katharina Franke that ligands other than phthalocyanine can decouple the metal

¹The CuPc molecules were deposited by means of thermal evaporation at a temperature of $T = 385^\circ\text{C}$ under UHV conditions. During evaporation the sample was thermalized to $T = 20^\circ\text{C}$.

center from a superconducting substrate such, that the magnetic moment is preserved and magnetic transitions are observable [164].

In addition, the relatively high spectral resolution of the AC Josephson spectrometer of about $12 \mu\text{eV}$ in our current setup should allow us to study hyperfine transitions of a single nuclear spin. The hyperfine transition of an individual Bismuth atom, for instance, has been calculated to be $\Delta E \approx 25 \mu\text{eV}$ [25]. This transition clearly matches our spectral resolution. Moreover, the high sensitivity of the AC Josephson spectrometer [22], in conjunction with the superconducting gap, favors detection of tiny signals as expected for this experiment [25].

7.2.3 Cooper Pairs and Photons II: Nonlinear Cooper Pair Tunnel Effects

In recent years the combination of a Josephson junction and a resonator in its immediate environment served as a valuable tool for theoretical and experimental studies of the Cooper-pair photon interaction [105], circuit quantum electrodynamics [126] and non-classical photon generation [127]. Of particular interest for us is a theoretical work by the group of Joachim Ankerhold, in which they investigate the non-linear interaction between a photon-field in a resonator and a Josephson junction [106]. By tuning both the resonator properties, i.e. the resonance frequency ν_0 and the quality factor Q , and the junction properties, i.e. the Josephson coupling energy E_J and the capacitive charging energy E_C , it should be possible to observe the transition from linear to nonlinear interactions between a resonator and a Josephson junction. Linear interactions correspond to a regime in which inelastic Cooper pair tunneling events excite the resonator modes but where the tunneling rate is so small, that for subsequent tunneling events the resonator will be always in the ground state again. However, if the Cooper pair tunneling rate or the quality of the resonator are increased, the resonator is excited faster than it can relax back into the ground state. In this situation, the occupied resonator can interact with the Josephson junction, which results in non-linear coupling effects such as charge-photon correlations [106].

Our setup also hosts the combination of a Josephson junction with a resonator, which is formed by the $\lambda/4$ -resonator in the tip. Moreover, we can tune both the resonator frequency ν_0 and its quality factor Q by changing the tip holder geometry as well as the Josephson coupling energy for more than two orders of magnitude by changing the tip-sample distance. To investigate whether our system allows us to observe this transition between linear and nonlinear coupling, we investigate the coupling parameter $\beta = \ln(2E_J E_C Q / (\hbar\nu_0)^2)$, as given in Ref. [106]. For a particular ratio of E_C versus ν_0 this parameter defines whether linear or nonlinear coupling occurs. In Fig. 7.2 we plot calculated values of β as a function of the normalized tunneling conductance G_N/G_0 . For the calculation we used a parameter set that is typical for our experiment and a ratio $\ln(E_C/(\hbar\nu_0)) \approx -0.2$ ($\Delta_1 = 800 \mu\text{eV}$, $\Delta_2 = 400 \mu\text{eV}$, $\hbar\nu_0 = 156 \mu\text{eV}$ that corresponds to an $l = 2 \text{ mm}$ long STM tip, $Q = 4$ and $C_J = 2.5 \text{ fF}$) [106]. We also plot the transition point from linear to nonlinear junction resonator interactions that we calculated for the ratio $\ln(E_C/(\hbar\nu_0)) \approx -0.2$ according to Ref. [106]. We find that the transition

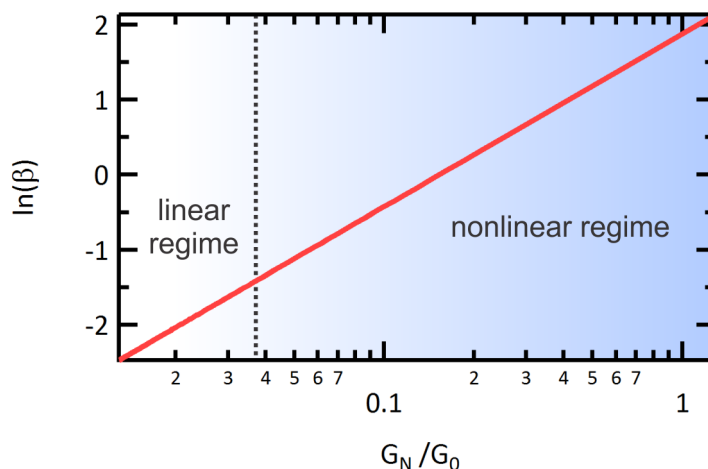


Figure 7.2 – Coupling parameter β as a function of the normalized tunneling conductance G_N/G_0 .

from linear to nonlinear interactions between Josephson junction and resonator occurs well within the tunnel regime $G_N \ll G_0$. For this reason, we should be able to observe a change in the experimental $I(V_J)$ characteristics if we cross this transition point by tuning E_J via the tip-sample distance. In detail, for the nonlinear interaction regime we expect deviations from the E_J^2 -dependence of the resonant current peak, which originates from the inelastic interaction with the resonator at $2eV_J = \hbar\nu_0$, as it is observed for linear interactions in the DCB regime [37, 38, 107].

It should be noted that, before the theoretical work on this problem [106] was published, we already performed experiments in which the shown parameter ratio, $\ln(E_C/(\hbar\nu_0)) \approx -0.2$, was given (cf. Ch. 5). Hence, it should be straightforward for us to repeat this experiment and address this exciting problem in more detail.

7.2.4 Tuning the Energy Scales: Coherent vs. Sequential Cooper pair Tunneling

For a Josephson junction in which the Josephson coupling energy is much smaller than the capacitive charging energy of the junction, $E_J \ll E_C$, the tunneling current is carried by the sequential tunneling of Cooper pairs and can be described by $P(E)$ -theory [37, 38], whereas in the opposite limit, where $E_J \gg E_C$, coherent tunneling of Cooper pairs sustain the tunneling current [7, 9]. By analyzing experimental $I(V_J)$ curves, we indeed find that in the limit $E_J \approx E_C$ $P(E)$ -theory fails to describe our experimental data around zero voltage, indicating an increasing contribution of coherent Cooper pair tunneling to the tunneling current. This transition between sequential and coherent tunneling had already been addressed experimentally at the end of the 1980s [141, 165]. However, this transition had never been clearly resolved, most likely due to the experimental constraint that in experiments using planar junction geometries it is difficult to change the ratio E_J versus E_C . Until now, we were also not able to observe the

full transition to the coherent tunneling regime because for $E_J \approx E_C$ we already reached point contact $G_N/G_0 \geq 1$ (cf. Ch. 4).

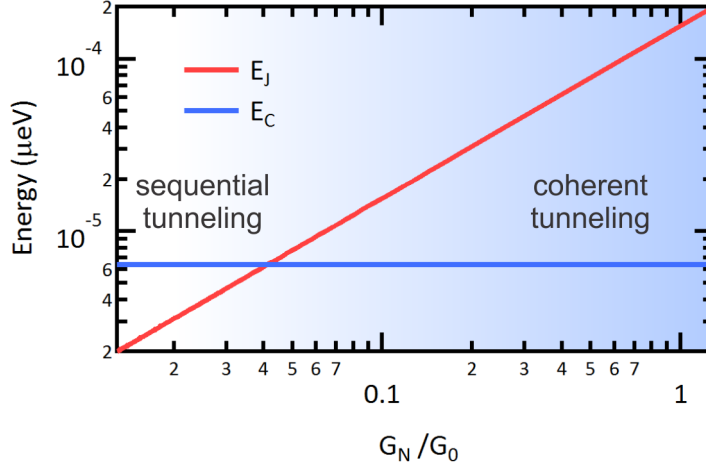


Figure 7.3 – Comparison of E_J and E_C as a function of the normalized tunneling conductance G_N/G_0 .

In order to address this transition in another experiment we therefore have to either increase E_J by changing the electrode material to superconductors of larger order parameter Δ , or decrease E_C by a larger junction capacitance C_J . For our STM setup the latter approach appears more favorable, since a larger junction capacitance can be obtained by varying the tip diameter and shape. Figure 7.3 compares calculated values of E_J and E_C as a function of the normalized tunneling conductance G_N/G_0 for typical experimental parameter ($\Delta_1 = 800 \mu\text{eV}$, $\Delta_2 = 400 \mu\text{eV}$) and assuming a junction capacitance of 50 fF. We find that the transition point $E_J = E_C$ has moved deeply into the tunnel regime. Simple calculations show that such an increased junction capacitance is readily obtained by tuning the thickness of the tip and shaping the sub-millimeter geometry of the tip apex. For this reason, we should be able to observe the full transition from sequential to coherent Cooper pair tunneling in our JSTM setup.

7.2.5 Studying the Quasiparticle Dissipation of Josephson Junctions

The decoherence of prepared qubit states via dissipative interaction with the environment is a fundamental problem in quantum computing. In Josephson phase qubits, the decoherence of the junction phase can result, for instance, from dissipative quasiparticle excitations, for which reason this phenomenon has attracted significant research interest [166, 167, 168, 169, 170]. As we show in Ch. 6 of this thesis, JSTM at millikelvin temperatures enables detailed studies of dissipation processes in Josephson junctions. First, at these low temperatures thermal quasiparticle excitations, a possible yet difficult-to-control source of dissipation, are frozen out and secondly, changing the tip sample distance allows us to precisely tune the amplitude of

dissipative quasiparticle excitations. For a Josephson junction that consists of two vanadium electrodes we find that the minimum dissipation is given by lifetime effects of Cooper pairs, which result from impurity scattering effects or surface scattering effects in the confined tip geometry [156], for instance. In order to minimize these lifetime effects, it is desirable to employ a different junction material. For this reason we recently started working on junctions that consist of an aluminum (001) crystal as the sample and an amorphous aluminum wire as the STM tip. In former experiments we already found that lifetime effects in such aluminum STM tips are negligibly small [81, 35].

Such a Josephson junction should allow us to investigate quasiparticle dissipation phenomena in more detail and we might approach the minimum dissipation limit as given by Chen, Fisher and Leggett in Ref. [147]. Moreover, it should help us to study the in-gap quasiparticle dissipation due to Andreev reflections in more detail, which we could already observe in vanadium junctions (cf. Ch. 6). Hence, JSTM helps us to shed more light on the quasiparticle dissipation phenomena in Josephson junctions and in this way, we can potentially contribute to the highly discussed topic of decoherence phenomena in Josephson phase qubits.

Bibliography

- [1] J. Bardeen, L. N. Cooper, and J. R. Schrieffer. Theory of superconductivity. *Phys. Rev.*, 108(5):1175, 1957.
- [2] J. Bardeen. Tunneling from a many-particle point of view. *Phys. Rev. Lett.*, 6:57–59, Jan 1961.
- [3] J. R. Schrieffer and J. W. Wilkins. Two-particle tunneling processes between superconductors. *Phys. Rev. Lett.*, 10:17–20, Jan 1963.
- [4] I. Giaever. Energy gap in superconductors measured by electron tunneling. *Phys. Rev. Lett.*, 5:147–148, Aug 1960.
- [5] I. Giaever. Electron tunneling between two superconductors. *Phys. Rev. Lett.*, 5(10):464–466, 1960.
- [6] A. Barone and G. Paterno. *Physics and Applications of the Josephson Effect*, volume 1. Wiley New York, 1982.
- [7] B. D. Josephson. Possible new effects in superconductive tunneling. *Phys. Lett.*, 1(7):251–253, 1962.
- [8] V. Ambegaokar and A. Baratoff. Tunneling between superconductors. *Phys. Rev. Lett.*, 10(11):486, 1963.
- [9] P. W. Anderson and J. M. Rowell. Probable observation of the Josephson superconducting tunneling effect. *Phys. Rev. Lett.*, 10(6):230–232, 1963.
- [10] S. Shapiro. Josephson currents in superconducting tunneling: The effect of microwaves and other observations. *Phys. Rev. Lett.*, 11(2):80, 1963.
- [11] J. Clarke. Principles and applications of SQUIDS. *Proc. IEEE*, 77(8):1208–1223, 1989.
- [12] M. H. Devoret and R. J. Schoelkopf. Superconducting circuits for quantum information: An outlook. *Science*, 339(6124):1169–1174, 2013.
- [13] C. A. Hamilton, C. J. Burroughs, and S. P. Benz. Josephson voltage standard - a review. *IEEE Transactions on Appl. Superconductivity*, 7(2):3756–3761, 1997.

Bibliography

- [14] J. Šmakov, I. Martin, and A. V. Balatsky. Josephson scanning tunneling microscopy. *Phys. Rev. B*, 64(21):212506, 2001.
- [15] J. G. Bednorz and K. A. Müller. Possible high- T_c superconductivity in the Ba-La-Cu-O system. *Z. Phys. B: Condens. Matter*, 64(2):189–193, 1986.
- [16] A. Yazdani, B. A. Jones, C. P. Lutz, M. F. Crommie, and D. M. Eigler. Probing the local effects of magnetic impurities on superconductivity. *Science*, 275(5307):1767–1770, 1997.
- [17] M. E. Flatté and J. M. Byers. Local electronic structure of a single magnetic impurity in a superconductor. *Phys. Rev. Lett.*, 78(19):3761, 1997.
- [18] M. I. Salkola, A. V. Balatsky, and J. R. Schrieffer. Spectral properties of quasiparticle excitations induced by magnetic moments in superconductors. *Phys. Rev. B*, 55(18):12648, 1997.
- [19] S. H. Ji, T. Zhang, Y. S. Fu, X. Chen, X. C. Ma, J. Li, W.-H. Duan, J.-F. Jia, and Q.-K. Xue. High-resolution scanning tunneling spectroscopy of magnetic impurity induced bound states in the superconducting gap of Pb thin films. *Phys. Rev. Lett.*, 100:226801, Jun 2008.
- [20] K. J. Franke, G. Schulze, and J. I. Pascual. Competition of superconducting phenomena and Kondo screening at the nanoscale. *Science*, 332(6032):940–944, 2011.
- [21] A. J. Drew, C. Niedermayer, P. J. Baker, F. L. Pratt, S. J. Blundell, T. Lancaster, R. H. Liu, G. Wu, X. H. Chen, I. Watanabe, et al. Coexistence of static magnetism and superconductivity in $\text{SmFeAsO}_{1-x}\text{F}_x$ as revealed by muon spin rotation. *Nature Mat.*, 8(4):310–314, 2009.
- [22] K. Baberschke, K. D. Bures, and S. E. Barnes. ESR in situ with a Josephson tunnel junction. *Phys. Rev. Lett.*, 53(1):98, 1984.
- [23] L. Bretheau, Ç. Ö. Girit, H. Pothier, D. Esteve, and C. Urbina. Exciting Andreev pairs in a superconducting atomic contact. *Nature*, 499(7458):312–315, 2013.
- [24] L. Bogani and W. Wernsdorfer. Molecular spintronics using single-molecule magnets. *Nature Mat.*, 7(3):179–186, 2008.
- [25] F. Delgado and J. Fernández-Rossier. Inelastic electron tunneling spectroscopy of a single nuclear spin. *Phys. Rev. Lett.*, 107:076804, Aug 2011.
- [26] O. Naaman, W. Teizer, and R. C. Dynes. Fluctuation dominated Josephson tunneling with a scanning tunneling microscope. *Phys. Rev. Lett.*, 87(9):097004, 2001.
- [27] J. G. Rodrigo, H. Suderow, and S. Vieira. On the use of STM superconducting tips at very low temperatures. *The European Physical Journal B - Condensed Matter and Complex Systems*, 40(4):483–488, 2004.

- [28] J. G. Rodrigo, V. Crespo, and S. Vieira. Josephson current at atomic scale: Tunneling and nanocontacts using a STM. *Physica C: Superconductivity*, 437:270–273, 2006.
- [29] N. Bergeal, Y. Noat, T. Cren, T. Proslie, V. Dubost, F. Debontridder, A. Zimmers, D. Roditchev, W. Sacks, and J. Marcus. Mapping the superconducting condensate surrounding a vortex in superconducting V_3Si using a superconducting MgB_2 tip in a scanning tunneling microscope. *Physical Review B*, 78(14):140507, 2008.
- [30] H. Kimura, R. P. Barber Jr, Sh. Ono, Y. Ando, and R. C. Dynes. Scanning Josephson tunneling microscopy of single-crystal $Bi_2Sr_2CaCu_2O_{8+\delta}$ with a conventional superconducting tip. *Phys. Rev. Lett.*, 101(3):037002, 2008.
- [31] Yu. M. Ivanchenko and L. A. Zil'berman. The Josephson effect in small tunnel contacts. *Sov. Phys. JETP*, 28(6), 1969.
- [32] H. Kambara, T. Matsui, Y. Niimi, and H. Fukuyama. Construction of a versatile ultralow temperature scanning tunneling microscope. *Rev. Sci. Instr.*, 78(7):-, 2007.
- [33] Y. J. Song, A. F. Otte, V. Shvarts, Z. Zhao, Y. Kuk, S. R. Blankenship, A. Band, F. M. Hess, and J. A. Stroscio. Invited review article: A 10 mK scanning probe microscopy facility. *Rev. Sci. Instr.*, 81(12):-, 2010.
- [34] H. Suderow, I. Guillamon, and S. Vieira. Compact very low temperature scanning tunneling microscope with mechanically driven horizontal linear positioning stage. *Review of Scientific Instruments*, 82(3), 2011.
- [35] M. Assig, M. Etzkorn, A. Enders, W. Stiepany, C. R. Ast, and K. Kern. A 10 mK scanning tunneling microscope operating in ultra high vacuum and high magnetic fields. *Rev. Sci. Instrum.*, 84(3):033903, 2013.
- [36] S. Misra, B. B. Zhou, I. K. Drozdov, J. Seo, L. Urban, A. Gyenis, S. C. J. Kingsley, H. Jones, and A. Yazdani. Design and performance of an ultra-high vacuum scanning tunneling microscope operating at dilution refrigerator temperatures and high magnetic fields. *Rev. Sci. Instr.*, 84(10):-, 2013.
- [37] D. V. Averin, Yu. V. Nazarov, and A. A. Odintsov. Incoherent tunneling of the Cooper pairs and magnetic flux quanta in ultrasmall Josephson junctions. *Physica B: Cond. Mat.*, 165:945–946, 1990.
- [38] M. H. Devoret, D. Esteve, H. Grabert, G.-L. Ingold, H. Pothier, and C. Urbina. Effect of the electromagnetic environment on the Coulomb blockade in ultrasmall tunnel junctions. *Phys. Rev. Lett.*, 64(15):1824, 1990.
- [39] T. Holst, D. Esteve, C. Urbina, and M. H. Devoret. Effect of a transmission line resonator on a small capacitance tunnel junction. *Phys. Rev. Lett.*, 73(25):3455, 1994.

Bibliography

- [40] M. Iansiti, A. T. Johnson, W. F. Smith, H. Rogalla, C. J. Lobb, and M. Tinkham. Charging energy and phase delocalization in single very small Josephson tunnel junctions. *Phys. Rev. Lett.*, 59(4):489, 1987.
- [41] M. Iansiti, A. T. Johnson, C. J. Lobb, and M. Tinkham. Quantum tunneling and low-voltage resistance in small superconducting tunnel junctions. *Phys. Rev. B*, 40(16):11370, 1989.
- [42] H. Fröhlich. Theory of the superconducting state. I. the ground state at the absolute zero of temperature. *Phys. Rev.*, 79(5):845–856, 1950.
- [43] J. Bardeen and D. Pines. Electron-phonon interaction in metals. *Phys. Rev.*, 99(4):1140, 1955.
- [44] L. P. Gorkov. Microscopic derivation of the Ginzburg-Landau equations in the theory of superconductivity. *Sov. Phys. JETP*, 9(6):1364–1367, 1959.
- [45] V. L. Ginsburg and L. D. Landau. On the theory of superconductivity. *Zh. Eksp. Teor. Fiz*, 20:1064, 1950.
- [46] G. Gamow. Zur Quantentheorie des Atomkernes. *Zeitschrift für Physik*, 51(3-4):204–212, 1928.
- [47] J. Nicol, S. Shapiro, and P. H. Smith. Direct measurement of the superconducting energy gap. *Phys. Rev. Lett.*, 5:461–464, Nov 1960.
- [48] M. H. Cohen, L. M. Falicov, and J. C. Phillips. Superconductive tunneling. *Phys. Rev. Lett.*, 8(8):316–318, 1962.
- [49] A. F. Andreev. The thermal conductivity of the intermediate state in superconductors. *Sov. Phys. JETP*, 19:1228, 1964.
- [50] G. E. Blonder, M. Tinkham, and T. M. Klapwijk. Transition from metallic to tunneling regimes in superconducting microconstrictions: Excess current, charge imbalance, and supercurrent conversion. *Phys. Rev. B*, 25(7):4515, 1982.
- [51] T. M. Klapwijk, G. E. Blonder, and M. Tinkham. Explanation of subharmonic energy gap structure in superconducting contacts. *Physica B+C*, 109:1657–1664, 1982.
- [52] M. Octavio, M. Tinkham, G. E. Blonder, and T. M. Klapwijk. Subharmonic energy-gap structure in superconducting constrictions. *Phys. Rev. B*, 27(11):6739, 1983.
- [53] M. Ternes, W. W. Schneider, J. C. Cuevas, C. P. Lutz, C. F. Hirjibehedin, and A. J. Heinrich. Subgap structure in asymmetric superconducting tunnel junctions. *Phys. Rev. B*, 74(13):132501, 2006.
- [54] R. C. Dynes, V. Narayanamurti, and J. P. Garno. Direct measurement of quasiparticle-lifetime broadening in a strong-coupled superconductor. *Phys. Rev. Lett.*, 41(21):1509, 1978.

-
- [55] B.D. Josephson. Supercurrents through barriers. *Advances in Physics*, 14(56):419–451, 1965.
- [56] N. R. Werthamer. Nonlinear self-coupling of Josephson radiation in superconducting tunnel junctions. *Phys. Rev.*, 147(1):255, 1966.
- [57] E. E. H. Shin and B. B. Schwartz. LC-time behavior of weak superconducting loops. *Phys. Rev.*, 152(1):207, 1966.
- [58] D. N. Langenberg, D. J. Scalapino, B. N. Taylor, and R. E. Eck. Microwave-induced DC voltages across Josephson junctions. *Phys. Lett.*, 20(6):563–565, 1966.
- [59] W. C. Stewart. Current voltage characteristics of Josephson junctions. *Appl. Phys. Lett.*, 12(8):277–280, 1968.
- [60] D. E. McCumber. Effect of AC impedance on DC voltage current characteristics of superconductor weak link junctions. *J. Appl. Phys.*, 39(7):3113–3118, 1968.
- [61] P. Joyez, D. Vion, M. Götz, M. H. Devoret, and D. Esteve. The Josephson effect in nanoscale tunnel junctions. *JOSC*, 12(6):757–766, 1999.
- [62] A. Steinbach, P. Joyez, A. Cottet, D. Esteve, M. H. Devoret, M. E. Huber, and J. M. Martinis. Direct measurement of the Josephson supercurrent in an ultrasmall Josephson junction. *Physical review letters*, 87(13):137003, 2001.
- [63] Michael Tinkham. *Introduction to Superconductivity*, volume 2. McGraw-Hill, Inc., 2012.
- [64] G. Binnig, H. Rohrer, C. Gerber, and E. Weibel. Tunneling through a controllable vacuum gap. *Appl. Phys. Lett.*, 40(2):178–180, 1982.
- [65] G. Binnig, H. Rohrer, C. Gerber, and E. Weibel. 7×7 reconstruction on Si(111) resolved in real space. *Phys. Rev. Lett.*, 50(2):120, 1983.
- [66] M. F. Crommie, C. P. Lutz, and D. M. Eigler. Confinement of electrons to quantum corrals on a metal surface. *Science*, 262(5131):218–220, 1993.
- [67] H. Roder, E. Hahn, H. Brune, J. P. Bucher, and K. Kern. Building one-dimensional and 2-dimensional nanostructures by diffusion-controlled aggregation at surfaces. *Nature*, 366:141–143, 1993.
- [68] B. C. Stipe, M. A. Rezaei, and W. Ho. Single-molecule vibrational spectroscopy and microscopy. *Science*, 280(5370):1732–1735, 1998.
- [69] P. Gambardella, A. Dallmeyer, K. Maiti, M. C. Malagoli, W. Eberhardt, K. Kern, and C. Carbone. Ferromagnetism in one-dimensional monatomic metal chains. *Nature*, 416(6878):301–304, 2002.

Bibliography

- [70] J. A Theobald, N. S. Oxtoby, M. A. Phillips, N. R. Champness, and P. H. Beton. Controlling molecular deposition and layer structure with supramolecular surface assemblies. *Nature*, 424(6952):1029–1031, 2003.
- [71] A. J. Heinrich, J. A. Gupta, C. P. Lutz, and D. M. Eigler. Single-atom spin-flip spectroscopy. *Science*, 306(5695):466–469, 2004.
- [72] J. V. Barth, G. Costantini, and K. Kern. Engineering atomic and molecular nanostructures at surfaces. *Nature*, 437(7059):671–679, 2005.
- [73] S. Loth, M. Etzkorn, C. P. Lutz, D. M. Eigler, and A. J. Heinrich. Measurement of fast electron spin relaxation times with atomic resolution. *Science*, 329(5999):1628–1630, 2010.
- [74] E. W. Hudson, S. H. Pan, A. K. Gupta, K. W. Ng, and J. C. Davis. Atomic-scale quasiparticle scattering resonances in $\text{Bi}_2\text{Sr}_2\text{CaCu}_2\text{O}_{8+\delta}$. *Science*, 285(5424):88–91, 1999.
- [75] J. Tersoff and D. R. Hamann. Theory and application for the scanning tunneling microscope. *Phys. Rev. Lett.*, 50(25):1998, 1983.
- [76] H. Haken and H. C. Wolf. *Atom-und Quantenphysik*. Springer, 1987.
- [77] H. Ibach and H. Lüth. *Festkörperphysik*. Springer Verlag, 1995.
- [78] C. J. Chen. *Introduction to Scanning Tunneling Microscopy*. Oxford University Press, 1993.
- [79] R. Wiesendanger. *Scanning Probe Microscopy and Spectroscopy: Methods and Applications*. Cambridge University Press, 1994.
- [80] C. R. Ast, M. Assig, A. Ast, and K. Kern. Design criteria for scanning tunneling microscopes to reduce the response to external mechanical disturbances. *Rev. Sci. Instrum.*, 79(9):093704, 2008.
- [81] Maximilian Assig. *Development of a Millikelvin Scanning Tunneling Microscope for Applications in Ultra High Vacuum and High Magnetic Fields*. PhD thesis, Ecole Fédérale Polytechnique de Lausanne, 2011.
- [82] ANPz50/LT/UHV z positioner. Attocube Systems.
- [83] Stacis 2100/3000. TMC.
- [84] I-2000 Laminar Flow Isolator. Newport.
- [85] H Kamerlingh Onnes. The resistance of pure mercury at helium temperatures. *Commun. Phys. Lab. Univ. Leiden*, 12(120):1, 1911.
- [86] H. London, G. R. Clarke, and E. Mendoza. Osmotic pressure of ^3He in liquid ^4He , with proposals for a refrigerator to work below 1°K . *Phys. Rev.*, 128(5):1992, 1962.

- [87] T. P. Das, R. de Bruyn Ouboter, and K. W. Taconis. *Proc. 9th Int. Conf. Low Temperature Physics*, page 1253, 1965.
- [88] F. Pobell. *Matter and Methods at Low Temperatures*. Springer Science & Business Media, 2007.
- [89] V. Shvarts, Z. Zhao, L. Bobb, and M. Jirmanus. UHV compatible ^3He - ^4He dilution refrigerators for STM in high magnetic field. *J. Phys.: Conference Series*, 150(1):012046, 2009.
- [90] N12-50F-257-0. Janis research inc.
- [91] J. B. Johnson. Thermal agitation of electricity in conductors. *Phys. Rev.*, 32:97, 1928.
- [92] H. Nyquist. Thermal agitation of electric charge in conductors. *Phys. Rev.*, 32:110, 1928.
- [93] S. T. Sekula and R. H. Kernohan. Magnetic properties of superconducting vanadium. *Physical Review B*, 5(3):904, 1972.
- [94] www.spl.eu. Surface preparation laboratory (SPL).
- [95] H. Ibach. *Physics of Surfaces and Interfaces*, volume 10. Springer, 2006.
- [96] R. Koller, W. Bergermayer, G. Kresse, E. L. D. Hebenstreit, C. Konvicka, M. Schmid, R. Podloucky, and P. Varga. The structure of the oxygen induced (1×5) reconstruction of $v(100)$. *Surf. Sci.*, 480(1):11–24, 2001.
- [97] M. Kralj, P. Pervan, M. Milun, K. Wandelt, D. Mandrino, and M. Jenko. HRAES, STM and ARUPS study of (5×1) reconstructed $V(100)$. *Surf. Sci.*, 526(1):166–176, 2003.
- [98] DLPCA-200 Transimpedance Amplifier. Femto Messtechnik GmbH.
- [99] Source Measure Unit B2911A. Keysight Technologies.
- [100] D. J. Van Harlingen. Phase-sensitive tests of the symmetry of the pairing state in the high-temperature superconductors—evidence for $d_{x^2-y^2}$ symmetry. *Rev. of Mod. Phys.*, 67(2):515, 1995.
- [101] S. H. Pan, E. W. Hudson, K. M. Lang, H. Eisaki, S. Uchida, and J. C. Davis. Imaging the effects of individual zinc impurity atoms on superconductivity in $\text{Bi}_2\text{Sr}_2\text{CaCu}_2\text{O}_{8+\delta}$. *Nature*, 403(6771):746–750, 2000.
- [102] P. Schlottmann. Some exact results for dilute mixed-valent and heavy-fermion systems. *Phys. Rep.*, 181(1):1–119, 1989.
- [103] E. W. Hudson, K. M. Lang, V. Madhavan, S. H. Pan, H. Eisaki, S. Uchida, and J. C. Davis. Interplay of magnetism and high-Tc superconductivity at individual Ni impurity atoms in $\text{Bi}_2\text{Sr}_2\text{CaCu}_2\text{O}_{8+\delta}$. *Nature*, 411(6840):920–924, 2001.

Bibliography

- [104] R. L. Kautz and J. M. Martinis. Noise-affected I-V curves in small hysteretic Josephson junctions. *Phys. Rev. B*, 42(16):9903, 1990.
- [105] M. Hofheinz, F. Portier, Q. Baudouin, P. Joyez, D. Vion, P. Bertet, P. Roche, and D. Estève. Bright side of the Coulomb blockade. *Phys. Rev. Lett.*, 106(21):217005, 2011.
- [106] V. Gramich, B. Kubala, S. Rohrer, and J. Ankerhold. From Coulomb-blockade to nonlinear quantum dynamics in a superconducting circuit with a resonator. *Phys. Rev. Lett.*, 111(24):247002, 2013.
- [107] G.-L. Ingold, H. Grabert, and U. Eberhardt. Cooper-pair current through ultrasmall Josephson junctions. *Phys. Rev. B*, 50(1):395, 1994.
- [108] A. O. Caldeira and A. J. Leggett. Quantum tunnelling in a dissipative system. *Ann. Phys.*, 149(2):374–456, 1983.
- [109] G.-L. Ingold and Yu. V. Nazarov. Charge tunneling rates in ultrasmall junctions. In H. Grabert and M. H. Devoret, editors, *Single Charge Tunneling*, volume 294 of *NATO ASI Series*, pages 21–107. Springer US, 1992.
- [110] G. Falci, V. Bujanja, and G. Schön. Quantum tunnelling in small-capacitance Josephson junctions in a general electromagnetic environment. *EPL (Europhys. Lett.)*, 16(1):109, 1991.
- [111] G. Falci, V. Bujanja, and G. Schön. Quasiparticle and Cooper pair tunneling in small capacitance Josephson junctions. *Z. Phys. B: Condens. Matter*, 85(3):451–458, 1991.
- [112] G.-L. Ingold and H. Grabert. Finite-temperature current-voltage characteristics of ultrasmall tunnel junctions. *EPL (Europhys. Lett.)*, 14(4):371, 1991.
- [113] H. Zinke, O. and Brunswig. Lehrbuch der Hochfrequenztechnik. Bd. 1: Koppelfilter, Leitungen, Antennen. *Berlin: Springer, 1973, 2. neubearb. Aufl.*, 1, 1973.
- [114] J. S. Belrose. The handbook of antenna design. *London: Peter Peregrinus Ltd.*, Ch. 15, 1983.
- [115] G. H. Brown and O. M. Jr. Woodward. Experimentally determined impedance characteristics of cylindrical antennas. *Proc. IRE*, 33(4):257–262, 1949.
- [116] Private communication with F. Portier from CEA Saclay, 2015.
- [117] U. Eckern, G. Schön, and V. Ambegaokar. Quantum dynamics of a superconducting tunnel junction. *Phys. Rev. B*, 30(11):6419, 1984.
- [118] G. Schön and A. D. Zaikin. Quantum coherent effects, phase transitions, and the dissipative dynamics of ultra small tunnel junctions. *Phys. Rep.*, 198(5):237–412, 1990.

-
- [119] M. F. Goffman, R. Cron, A. Levy Yeyati, P. Joyez, M. H. Devoret, D. Esteve, and C. Urbina. Supercurrent in atomic point contacts and Andreev states. *Phys. Rev. Lett.*, 85:170–173, Jul 2000.
- [120] P.F. Bagwell, R. Riedel, and L. Chang. Mesoscopic Giaever and Josephson junctions. *Physica B: Condensed Matter*, 203(3–4):475 – 480, 1994.
- [121] V. S. Shumeiko, E. N. Bratus, and G. Wendin. Scattering theory of superconductive tunneling in quantum junctions. *Low Temperature Physics*, 23(3):181–198, 1997.
- [122] J. C. Cuevas, A. Martin-Rodero, and A. L. Yeyati. Hamiltonian approach to the transport properties of superconducting quantum point contacts. *Physical Review B*, 54(10):7366, 1996.
- [123] Ronald Cron. *Les contacts atomiques: un banc d'essai pour la physique mésoscopique*. PhD thesis, Université Paris 6, 2002.
- [124] A. Burtzloff, A. Weismann, M. Brandbyge, and R. Berndt. Shot noise as a probe of spin-polarized transport through single atoms. *Physical Review Letters*, 114(1):016602, 2015.
- [125] M. Ruby, F. Pientka, Y. Peng, F. von Oppen, B. W. Heinrich, and K. J. Franke. Tunneling processes into localized subgap states in superconductors. *arXiv:1502.05048*, Feb 2015.
- [126] J.-M. Pirkkalainen, S. U. Cho, J. Li, G. S. Paraoanu, P. J. Hakonen, and M. A. Sillanpää. Hybrid circuit cavity quantum electrodynamics with a micromechanical resonator. *Nature*, 494(7436):211–215, 2013.
- [127] J. Leppäkangas, G. Johansson, M. Marthaler, and M. Fogelström. Nonclassical photon pair production in a voltage-biased Josephson junction. *Phys. Rev. Lett.*, 110:267004, Jun 2013.
- [128] J. M. Elzerman, R. Hanson, L. H. W. Van Beveren, B. Witkamp, L. M. K. Vandersypen, and L. P. Kouwenhoven. Single-shot read-out of an individual electron spin in a quantum dot. *Nature*, 430(6998):431–435, 2004.
- [129] P. Neumann, J. Beck, M. Steiner, F. Rempp, H. Fedder, P. R. Hemmer, J. Wrachtrup, and F. Jelezko. Single-shot readout of a single nuclear spin. *Science*, 329(5991):542–544, 2010.
- [130] T. L. Cocker, V. Jelic, M. Gupta, S. J. Molesky, J. A. J. Burgess, G. De Los Reyes, L. V. Titova, Y. Y. Tsui, M. R. Freeman, and F. A. Hegmann. An ultrafast terahertz scanning tunnelling microscope. *Nature Photon.*, 7(8):620–625, 2013.
- [131] U. Kemiktarak, T. Ndukum, K. C. Schwab, and K. L. Ekinci. Radio-frequency scanning tunnelling microscopy. *Nature*, 450(7166):85–88, 2007.
- [132] Germany CST Corporation, Darmstadt. CST microwave studio (MWS) 2013.

Bibliography

- [133] D. M. Pozar. *Microwave Engineering*, volume 3rd Ed., Ch.4. John Wiley & Sons, New York City (NY), 2005.
- [134] S. Yoshida, Y. Terada, M. Yokota, O. Takeuchi, H. Oigawa, and H. Shigekawa. Optical pump-probe scanning tunneling microscopy for probing ultrafast dynamics on the nanoscale. *The European Physical Journal Special Topics*, 222(5):1161–1175, 2013.
- [135] C. Grosse, M. Etzkorn, K. Kuhnke, S. Loth, and K. Kern. Quantitative mapping of fast voltage pulses in tunnel junctions by plasmonic luminescence. *Appl. Phys. Lett.*, 103(18):183108, 2013.
- [136] J. Nagamatsu, N. Nakagawa, T. Muranaka, Y. Zenitani, and J. Akimitsu. Superconductivity at 39 K in magnesium diboride. *Nature*, 410(6824):63–64, 2001.
- [137] L. Bretheau, Ç. Ö. Girit, C. Urbina, D. Esteve, and H. Pothier. Supercurrent spectroscopy of Andreev states. *Phys. Rev. X*, 3(4):041034, 2013.
- [138] L. Bretheau, Ç. Ö. Girit, M. Houzet, H. Pothier, D. Esteve, and C. Urbina. Theory of microwave spectroscopy of Andreev bound states with a Josephson junction. *Phys. Rev. B*, 90(13):134506, 2014.
- [139] M. Iansiti, M. Tinkham, A. T. Johnson, W. F. Smith, and C. J. Lobb. Charging effects and quantum properties of small superconducting tunnel junctions. *Phys. Rev. B*, 39(10):6465, 1989.
- [140] J. R. Kirtley, C. D. Tesche, W. J. Gallagher, A. W. Kleinsasser, R. L. Sandstrom, S. I. Raider, and M. P. A. Fisher. Measurement of the intrinsic sub-gap dissipation in Josephson junctions. *Phys. Rev. Lett.*, 61(20):2372, 1988.
- [141] M. Iansiti, A. T. Johnson, C. J. Lobb, and M. Tinkham. Crossover from Josephson tunneling to the Coulomb blockade in small tunnel junctions. *Phys. Rev. Lett.*, 60(23):2414, 1988.
- [142] A. T. Johnson, C. J. Lobb, and M. Tinkham. Effect of leads and energy gap upon the retrapping current of Josephson junctions. *Phys. Rev. Lett.*, 65(10):1263, 1990.
- [143] N. W. Ashcroft and N. D. Mermin. *Solid State Physics*. Holt, Rinehart and Winston, New York, 2005.
- [144] J. J. Sakurai and J. Napolitano. *Modern Quantum Mechanics*. Addison-Wesley, 2011.
- [145] I. N. Bronstein, J. Hromkovic, B. Luderer, H. R. Schwarz, J. Blath, A. Schied, S. Dempe, G. Wanka, S. Gottwald, E. Zeidler, and Others. *Taschenbuch der Mathematik*, volume 1. Springer-Verlag, 2012.
- [146] W. C. Scott. Hysteresis in the DC switching characteristics of Josephson junctions. *Appl. Phys. Lett.*, 17(4):166–169, 1970.

- [147] Y. C. Chen, M. P. A. Fisher, and A. J. Leggett. The return of a hysteretic Josephson junction to the zero-voltage state: I-V characteristic and quantum retrapping. *J. Appl. Phys.*, 64(6):3119–3142, 1988.
- [148] V. Ambegaokar, U. Eckern, and G. Schön. Quantum dynamics of tunneling between superconductors. *Phys. Rev. Lett.*, 48(25):1745, 1982.
- [149] B. Mirhashem and R. A. Ferrell. Comment on "crossover from Josephson tunneling to the Coulomb blockade in small tunnel junctions". *Phys. Rev. Lett.*, 62:483–483, Jan 1989.
- [150] K. K. Likharev and A. B. Zorin. Theory of the Bloch-wave oscillations in small Josephson junctions. *J. Low Temp. Phys.*, 59(3-4):347–382, 1985.
- [151] S. Chakravarty. Quantum fluctuations in the tunneling between superconductors. *Phys. Rev. Lett.*, 49(9):681, 1982.
- [152] F. Guinea, V. Hakim, and A. Muramatsu. Diffusion and localization of a particle in a periodic potential coupled to a dissipative environment. *Phys. Rev. Lett.*, 54(4):263, 1985.
- [153] M. P. A. Fisher and W. Zwerger. Quantum brownian motion in a periodic potential. *Phys. Rev. B*, 32(10):6190, 1985.
- [154] Kazumi Maki. Pauli paramagnetism and superconducting state. II. *Prog. Theo. Phys.*, 32(1):29–36, 1964.
- [155] D. C. Worledge and T. H. Geballe. Maki analysis of spin-polarized tunneling in an oxide ferromagnet. *Phys. Rev. B*, 62(1):447, 2000.
- [156] M. Eltschka, B. Jäck, M. Assig, O. V. Kondrashov, M. A. Skvortsov, M. Etzkorn, C. R. Ast, and K. Kern. Probing absolute spin polarization at the nanoscale. *Nano Letters*, 14(12):7171–7174, 2014.
- [157] N. Bohr. Über die Serienspektren der Elemente. *Z. Phys.*, 2:423, 1920.
- [158] P. Ehrenfest. Bemerkung über die Angenäherte Gültigkeit der klassischen Mechanik innerhalb der Quantenmechanik. *Z. Phys. A: Hadrons Nucl.*, 45:455–457, 1928.
- [159] G.-L. Ingold and H. Grabert. Effect of zero point phase fluctuations on Josephson tunneling. *Phys. Rev. Lett.*, 83:3721–3724, Nov 1999.
- [160] E. W. Hudson, K. M. Lang, V. Madhavan, S. H. Pan, H. Eisaki, S. Uchida, and J. C. Davis. Interplay of magnetism and high-T_c superconductivity at individual Ni impurity atoms in Bi₂Sr₂CaCu₂O_{8+δ}. *Nature*, 411(6840):920–924, 2001.
- [161] I. Zeljkovic, Z. Xu, J. Wen, G. Gu, R. S. Markiewicz, and J. E. Hoffman. Imaging the impact of single oxygen atoms on superconducting Bi_{2+y}Sr_{2-y}CaCu₂O_{8+x}. *Science*, 337(6092):320–323, 2012.

Bibliography

- [162] G. Balasubramanian, I. Y. Chan, R. Kolesov, M. Al-Hmoud, J. Tisler, C. Shin, C. Kim, A. Wojcik, P. R. Hemmer, A. Krueger, et al. Nanoscale imaging magnetometry with diamond spins under ambient conditions. *Nature*, 455(7213):648–651, 2008.
- [163] R. Vincent, S. Klyatskaya, M. Ruben, W. Wernsdorfer, and F. Balestro. Electronic read-out of a single nuclear spin using a molecular spin transistor. *Nature*, 488(7411):357–360, 2012.
- [164] B. W. Heinrich, L. Braun, J. I. Pascual, and K. J. Franke. Protection of excited spin states by a superconducting energy gap. *Nature Phys.*, 9(12):765–768, 2013.
- [165] T. A. Fulton, P. L. Gammel, D. J. Bishop, L. N. Dunkleberger, and G. J. Dolan. Observation of combined Josephson and charging effects in small tunnel junction circuits. *Phys. Rev. Lett.*, 63(12):1307, 1989.
- [166] M. H. S. Amin and A. Yu Smirnov. Quasiparticle decoherence in d-wave superconducting qubits. *Phys. Rev. Lett.*, 92(1):017001, 2004.
- [167] G. Catelani, J. Koch, L. Frunzio, R. J. Schoelkopf, M. H. Devoret, and L. I. Glazman. Quasiparticle relaxation of superconducting qubits in the presence of flux. *Phys. Rev. Lett.*, 106:077002, Feb 2011.
- [168] G. Catelani, S. E. Nigg, S. M. Girvin, R. J. Schoelkopf, and L. I. Glazman. Decoherence of superconducting qubits caused by quasiparticle tunneling. *Phys. Rev. B*, 86(18):184514, 2012.
- [169] J. M. Martinis, M. Ansmann, and J. Aumentado. Energy decay in superconducting Josephson-junction qubits from nonequilibrium quasiparticle excitations. *Phys. Rev. Lett.*, 103:097002, Aug 2009.
- [170] I. M. Pop, K. Geerlings, G. Catelani, R. J. Schoelkopf, L. I. Glazman, and M. H. Devoret. Coherent suppression of electromagnetic dissipation due to superconducting quasiparticles. *Nature*, 508(7496):369–372, 2014.

Curriculum Vitae

Personal Details

Name	Berthold Jäck
Date of Birth	February 21, 1985
Place of Birth	Karlsruhe, Germany
Nationality	German

Education

Since May 2012	PhD student <i>Ecole Polytechnique Fédérale de Lausanne</i> Doctoral School of Physics Thesis: <i>Josephson Tunneling at the Atomic Scale: The Josephson Effect as a Local Probe</i>
Aug. 2008 - May 2009	Student Exchange Year <i>University of California at Berkeley</i> Fellow of the German Academic Exchange Association (DAAD)
Oct. 2005 - May 2011	Diploma Studies of Nanotechnology <i>University of Würzburg, Würzburg</i> Diploma degree with distinction Thesis: <i>Exciton Dynamics in Ordered and Disordered Organic Systems</i>
Sep. 1995 - Jul. 2004	High School <i>Gymnasium Karlsbad, Karlsbad</i>

Bibliography

Scientific & Working Experience

- Since Oct. 2011 **Research Associate**
Max-Planck-Institute for Solid State Research, Stuttgart
- Oct. 2009 - Feb. 2011 **Teaching Assistant**
University of Würzburg, Würzburg
Tutoring of lectures and lab classes
- Aug. 2008 - May 2009 **Research Internship**
Lawrence Berkeley National Laboratory, USA
Preparation & characterization of Graphene samples
- Feb. 2008 - Apr- 2008 **Research Internship**
Qimonda Dresden GmbH, Dresden
Technology development in semiconductor industry
- May 2005 - Sep. 2005 **Advisor**
School for Disabled Children, Karlsbad
Nursing of disabled children
- Sep. 2004 - May 2005 **Civil Service**
School for Disabled Children, Karlsbad
Nursing of disabled children

Publications

- **B. Jäck**, J. Senkpiel, M. Eltschka, M. Etzkorn, C. R. Ast, and K. Kern, “Quasiparticle dissipation phenomena in Josephson junctions“, *in preparation* (2015)
- M. Eltschka, **B. Jäck**, M. Assig, O. V. Kondrashov, M. A. Skvortsov, M. Etzkorn, C. R. Ast, and K. Kern, “Superconducting STM tips in a magnetic field: geometry-controlled order of the phase transition“, *submitted* (2015)
- **B. Jäck**, M. Eltschka, M. Assig, M. Etzkorn, C. R. Ast, and K. Kern, “Critical Josephson current in the dynamical Coulomb blockade regime“, *submitted* (2015)
- **B. Jäck**, M. Eltschka, M. Assig, A. Hardock, M. Etzkorn, C. R. Ast, and K. Kern, “A nanoscale gigahertz source realized with Josephson scanning tunneling microscopy“, *Appl. Phys. Lett.* **106**, 013109 (2015)
- M. Eltschka, **B. Jäck**, M. Assig, O. V. Kondrashov, M. A. Skvortsov, M. Etzkorn, C. R. Ast, and K. Kern, “Probing Absolute Spin Polarization at the Nanoscale“, *Nano Lett.* **14**, 7171 (2014)
- B. Giesecking, **B. Jäck**, E. Preis, S. Jung, M. Forster, U. Scherf, C. Deibel, and V. Dyakonov, “Excitation Dynamics in Low Band Gap Donor–Acceptor Copolymers and Blends“, *Adv. Energy. Mater.* **2** (12), 1477 – 1482 (2012)